QUANTUM CHARGE TRANSPORT IN 10-NANOMETER SCALE SUSPENDED GRAPHENE TRANSISTORS

Vahid Tayari

A thesis
in
The Department
of
Physics

Presented in Partial Fulfillment of the Requirements
For the Degree of Doctor of Philosophy
Concordia University
Montréal, Québec, Canada

April 2014

Concordia University
School of Graduate Studies

This is to certify that the thesis prepared

By: **Mr. Vahid Tayari**

Entitled: **Quantum charge transport in 10-nanometer scale suspended graphene transistors**

and submitted in partial fulfillment of the requirements for the degree of

Doctor of Philosophy (PhD in Physics)

complies with the regulations of this University and meets the accepted standards with respect to originality and quality.

Signed by the final examining commitee:

Dr. Guillaume Lamoureux _____ Chair

Dr. Oussama Moutanabbir _____ External Examiner

Dr. Pat Forgione _____ Examiner

Dr. Laszlo Kalman _____ Examiner

Dr. Pablo Bianucci _____ Examiner

Dr. Alexandre Champagne _____ Supervisor

Approved _____

Chair of Department or Graduate Program Director

_____ 20 _____ _____

Dean of Faculty

Abstract

Quantum charge transport in 10-nanometer scale suspended graphene transistors

Vahid Tayari, Ph.D.
Concordia University, 2014

Since the discovery of graphene there has been a growing interest in fabricating and studying nanometer scale graphene devices for future nanoelectronic applications. We developed a nanoetching technique called electromigration to fabricate ≈ 10 nm scale suspended and clean graphene quantum dots (QD) and ballistic transistors. Because these devices are so small, we were able to explore the fundamental quantum properties of their relativistic-like charge carriers.

Using our electromigration technique, we tailored the shape and size of suspended graphene channels, forming ultra-short devices which behave as graphene QDs if they are narrow (≈ 30 nm) or ballistic transistors if they are wider (≈ 100 nm). Our $\approx 30 \times 30$ nm suspended graphene QDs are, to our knowledge, the smallest suspended graphene QDs made to date. We measured electron transport across these devices and observed a variable charging energy as a function of the charge occupation of the dot, as expected due to the chaotic billiard transport of Dirac fermions. We observed signatures of electron-vibron (e-v) coupling in our suspended QDs and measured their self-actuated out-of-plane vibron resonances (bending mode), whose frequencies range up to ≈ 100 GHz.

We used a gold film to locally gate graphene and create ultra-short p-n junctions. We fabricated $\approx 20 - 100$ nm long suspended graphene ballistic transistors and measured n-p-n junctions (down to ≈ 10 nm p-n junctions). We observed coherent ballistic transport in agreement with the theory of Dirac fermions, and measured Fabry-Pérot interferences in our devices. We measured coherence lengths up to ≈ 700 nm in our graphene transistors, which is much longer than the length of the channels of the transistors. This showed that the graphene contacts (gold covered) are also ballistic.

The fabrication method we developed to make ultra-short suspended graphene

devices, combined with the observation of clear signatures of quantum coherent transport, opens the way to explore graphene physics and applications at the 10 nm scale.

Acknowledgments

Firstly, I would like to acknowledge all who made my stay at department of physics at Concordia University both enjoyable and progressive.

Thank you to my supervisor Alex Champagne. Your passion in science, support, advice, patience and hard work, have helped me to learn many things. I could not ask for a better supervisor. I am extremely grateful.

My gratitude goes to my fellows from the Champagne group. Serap, Joshua, Andrew, Jimi, Colleen, Patrick and Dhan, this would not be possible without your help, energy, kindness and sense of humor. It was a great pleasure to work with you and I have been so lucky to have friends such you guys.

I would like to thank the microfabrication facilities and staff at Mcgill, École Polytechnique and Sherbrooke Universities for their cooperation and advice which made this work possible.

To my family, I thank you mom, dad and Farid my dear brother, you have been always there for me. Your endless support and encouragement gave me determination to face the challenges and accomplish my PhD. I am grateful to have such great family.

Finally, I would like to express my gratitude to all of my friends in Canada, back home, and all over the world. You have contributed significantly to my life and my achievements.

Contents

List of Figures

List of Tables

Chapter 1

Introduction

Experimental electron transport in $10 - 100$ nm scale graphene nanostructures is still largely unexplored. At this scale the quantum properties of the relativistic-like charge carriers (Dirac fermions) in graphene offer a platform for fundamental studies and the fabrication of advanced nanoelectronic devices. To fabricate devices down to the 10 nm-scale, we have developed a nanoetching technique based on electromigration [1, 2, 3]. Fig. 1.1 shows one of our ultra-short graphene transistors. Fabrication at this scale is currently beyond the limit of standard nanofabrication methods.

In contamination-free 10 nm-scale suspended graphene devices, charge carriers (electrons or holes) do not scatter while traversing the device. Thus, they preserve their quantum phase which can be used to store quantum information. Depending on the graphene-contact interface resistance, ultra-short graphene devices can be either ballistic channel (quantum wires) or quantum dots (quantum puddles). We observe quantum dot (QD) behavior in devices whose width is ≈ 30 nm when $T = 4.2$ K, whereas we observe ballistic transport in wider devices.

We explore charge transport in 10 nm scale suspended graphene devices with widths ranging from 30 nm up to 1.5 μm. We suspend the devices to remove substrate disorder, and the associated charge scattering, to preserve the quantum nature of the charge transport. We also remove contamination and residues, such as H_2O and organic residues from nanofabrication with Joule effect annealing of the samples. We can reduce the effect of edge disorder by increasing the width of the devices. We observe clear QD behavior in ≈ 30 nm wide devices [1]. These $\approx 30 \times 30$ nm graphene QDs are among the smallest made to date, and the first such devices to be suspended

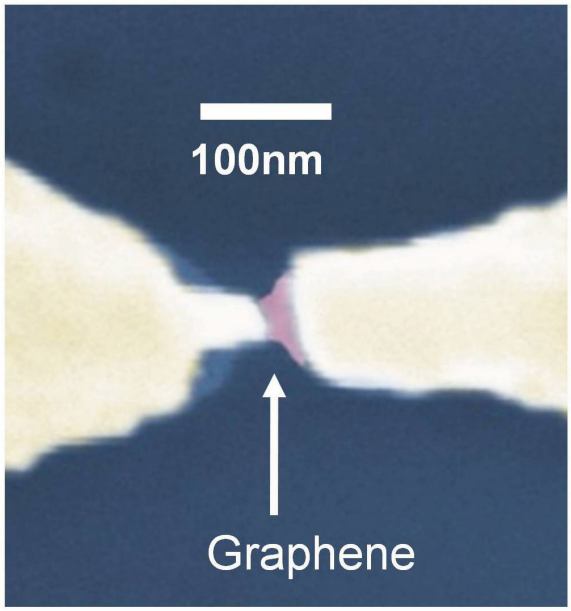

Figure 1.1: Scanning electron microscope image of one of our ultra-short graphene transistor (length $\approx$ 23 nm).

(to the best of our knowledge). We observe signatures of electron-vibron (e-v) coupling in suspended quantum dots. In these nano-electromechanical systems (NEMS), we demonstrate vibrational frequencies on the order of 100 GHz, which is orders of magnitude higher than previously reported for graphene resonators [4, 5, 6, 7, 8, 9]. These suspended graphene QDs offer a platform which will be useful for studying the effects of strain on Dirac fermion transport and e-v coupling. High-frequency suspended graphene NEMS can be used as ultra sensitive force/mass sensors.

In wider devices, $W > 30$ nm, we measure coherent ballistic transport consistent with theoretical predictions for Dirac fermions [10] (in preparation). These devices form n-p-n transistors. A p-n junction is an interface between two types of semiconductors which are hole (p) and electron doped (n). p-n junctions are the building blocks of modern integrated circuits. To fabricate a graphene based ballistic p-n junction it is necessary to create a charge carrier density gradient in a sub-micron region. Usually, a global back gate and a local top gate are used to dope graphene and create this charge carrier density gradient. Although there has been a lot of effort to reduce the size of p-n junctions [11, 12, 13], the thickness of the necessary insulating layer between the gate and graphene limits the downsizing of the junction p-n. We

demonstrate ≈ 23 nm long suspended graphene ballistic *n-p-n* and *n-n'-n* junctions (10 nm *p-n* junctions. To make these small *p-n* junctions, the smallest reported, we dope graphene using the gold contacts themselves. Since the spacing between the graphene and the gold film deposited on the graphene is ≤1 nm, it does not limit the size of the *n-p* or *(n-n')* junction.

We observe Fabry-Pérot (FP) interference in the conductance (G) of our transistors as a function of the charge carrier density and bias voltage, which demonstrate quantum coherent transport [10]. FP oscillations arise from interferences between the wavefunctions of reflected and transmitted carriers. The maximum coherence length (up to 700 nm) in our devices is much longer than the length of the transistor channel. This demonstrates that the ballistic transport is extended in graphene buried under the gold contacts. Thus, our graphene transistors are connected by graphene contacts which can transmit the quantum information in the phase of the charge carriers over a distance of ≈ 700 nm [10]. These ballistic *n-p-n* transistors and wires (graphene contacts) are the building blocks needed to develop graphene-based quantum nanoelectronics. The devices that we fabricate also provide a platform for future studies of the effects of strain (gauge field) on the phase of the carriers in 10 nm scale *p-n* junction.

The structure of this thesis is as follows: the remainder of Chapter 1 will provide a brief introduction to graphene. In Chapter 2 we will describe the microfabrication procedures required to create suspended gold break-junctions covering graphene. In Chapter 3 we will describe a nanoetching technique which we have developed to fabricate ≈ 30 nm long suspended graphene QDs. We will also discuss the signatures of *e-v* coupling in our suspended QDs which indicate vibrational frequencies up to ≈ 100 GHz. In Chapter 4, we will explain how to fabricate ballistic transistors, whose widths is > 30 nm, using the nanoetching technique described in Chapter 3. We will then demonstrate ballistic transport in ≈ 23 to 105 nm long ballistic (*n-p-n*) transistors in agreement with the theory of Dirac fermions. We will show that the charge carriers have phase coherence length up to ≈ 700 nm in these transistors, indicating the formation of coherent ballistic transport under the gold contacts.

1.1 Graphene

Graphene is a one-atom thick carbon crystal with a two-atom basis hexagonal lattice. It is an ideal two-dimensional system. Graphene has outstanding properties such as a linear band dispersion at low energy, is the strongest material known, and has very high heat conductivity. These qualities make it a promising material for fundamental studies and industrial applications [14, 15, 16].

The low energy dispersion relation of charge carriers (electrons and holes) in graphene is linear. The behavior of these carriers can thus be described by the theory of Dirac fermions. One of the interesting properties of Dirac fermions is that they cannot be stopped by a potential barrier when incident at a zero angle. In other words, the transmission probability of Dirac fermions through a potential barrier of any height is unity at normal incidence ($\theta = 0$) [17]. This anomalous tunneling property is called Klein tunneling and gives rise to a very high electronic mobility in graphene [18], which makes graphene a promising candidate for high-speed electronics [19]. Graphene has incredible mechanical properties. It can sustain up to a 25% strain [7, 20], which makes it an ideal material for high-frequency NEMS [7, 4]. NEMS can have applications in mass/force sensors [21, 22] and in computation [4]. Graphene can also tolerate very high current densities and high temperatures [18, 23, 24, 25]. This offers the possibility to anneal graphene at high temperatures using Joule heating, to remove any absorbed contaminants [18, 23]. Graphene has a very high heat conductivity which can have applications in heat management in nanoelectronics [23, 26].
In the following subsections we will describe graphene's band structure, and introduce Klein tunneling.

1.2 Band structure of graphene

We calculate the band structure of graphene using the tight-binding approximation. Figure 1.2 shows the hexagonal lattice of graphene with lattice vectors $\vec{a}_1 = \frac{a}{2}(3, \sqrt{3})$ and $\vec{a}_2 = \frac{a}{2}(3, -\sqrt{3})$, where $a = 1.42$ $\mathring{A}$ is the carbon-carbon distance [14]. Fig. 1.2 shows that the lattice structure of graphene consists of two sublattices, sublattice A (blue circles) and sublattice B (red circles). The nearest neighbor vectors connect

the two lattices, and are as following [14]:

$$\vec{\delta}_1 = \frac{a}{2}(1, \sqrt{3}) \qquad \vec{\delta}_2 = \frac{a}{2}(1, -\sqrt{3}) \qquad \vec{\delta}_3 = -a(1, 0) \tag{1.1}$$

The wave function of electrons can be considered as a superposition of the wave

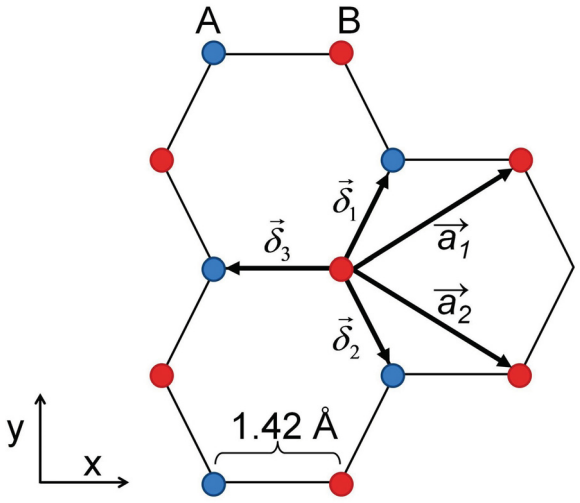

Figure 1.2: Graphene's hexagonal lattice. Details the hexagonal lattice of graphene with lattice vectors $\vec{a}_1 = \frac{a}{2}(3, \sqrt{3})$ and $\vec{a}_2 = \frac{a}{2}(3, -\sqrt{3})$, where $a = 1.42$ $\mathring{A}$ is the carbon-carbon distance. The lattice structure consists of two sublattices, sublattice A (blue circles) and sublattice B (red circles). $\vec{\delta}_1$, $\vec{\delta}_2$ and $\vec{\delta}_3$ are the nearest neighbor vectors.

functions on sublattice A and sublattice B:

$$\psi(\mathbf{r}) = \sum_{A_i} e^{i\mathbf{k}\cdot\mathbf{r}_{A_i}} \phi(\mathbf{r} - \mathbf{r}_{A_i}) + \lambda \sum_{B_j} e^{i\mathbf{k}\cdot\mathbf{r}_{B_j}} \phi(\mathbf{r} - \mathbf{r}_{B_j}) \tag{1.2}$$

Where $\lambda = 1$ is a prefactor and used to factorize the wavefunctions. The Hamiltonian of the lattice can be approximated as:

$$H = H_0 + \Delta U \tag{1.3}$$

Where H_0 is the Hamiltonian of and electron due to the potential of a single carbon atom, and ΔU is a correction due to hopping to nearest neighbour atom. The energy

band structure can be extracted by finding the eigenvalues of the Hamiltonian as:

$$H\psi(\mathbf{r}) = (H_0 + \Delta U)\psi(\mathbf{r}) = E(\mathbf{k})\psi(\mathbf{r}) \tag{1.4}$$

The above equation leads to two equations be solved by projecting into $< \phi(\mathbf{r} - \mathbf{r}_{A_i})|$ from the left, then repeating the same thing with $< \phi(\mathbf{r} - \mathbf{r}_{B_j})|$. $E(\mathbf{k})$ can be found by diagonalizing these two equations. To do so, we make use of the fact that the atomic wavefunctions of the different carbon atoms are orthogonal ($\int d\mathbf{r}\phi^*(\mathbf{r} - \mathbf{r}_{A_i})\phi(\mathbf{r} - \mathbf{r}_{A_j}) = \delta_{ij}$ and $\int d\mathbf{r}\phi^*(\mathbf{r} - \mathbf{r}_{A_i})\phi(\mathbf{r} - \mathbf{r}_{B_j}) = 0$). Finally, the band structure of graphene can be written as:

$$E(\mathbf{k}) = E_o \pm \sqrt{3t^2 + 2t^2\cos(k_y\sqrt{3}a) + 4t^2\cos(k_x\frac{3a}{2})\cos(k_y\frac{\sqrt{3}a)}{2}} \tag{1.5}$$

where E_o is the energy given by H_o, t is the nearest neighbor hopping energy $t = (\int d\mathbf{r}\phi^*(\mathbf{r} - \mathbf{r}_{A_i})\Delta U\phi(\mathbf{r} - \mathbf{r}_{A_j}) \approx 2.8$ eV [14]. Figure 1.3 shows the energy as a function of k_x and k_y (Eq. 1.5). It demonstrates that close to the crystal momentum points ($\mathbf{K} = (\frac{2\pi}{3a}, \frac{2\pi}{3\sqrt{3}a})$ and $\mathbf{K'} = (\frac{2\pi}{3a}, -\frac{2\pi}{3\sqrt{3}a})$) the energy is linear as a function of momentum (see Fig. 1.3). This can be written as $E(\mathbf{k}) = \pm\hbar v_F\mathbf{k}$, which is similar to the dispersion relation of photon $E(\mathbf{k}) = \pm\hbar c\mathbf{k}$, but with the velocity of light replaced by the Fermi velocity $v_F \approx c/300$.

1.2.1 Klein tunneling in graphene

It is predicted that Dirac fermions can traverse any potential barrier with perfect transmission at normal incidence. This transmission does not depends on the barrier height in contrast to non-relativistic quantum tunneling, in which the transmission exponentially decays with barrier height. This anomalous tunneling for Dirac fermions is known as Klein tunneling [27]. Fig. 1.4(a) shows a cartoon of Klein tunneling for a Dirac fermion with Fermi an energy of E and a linear energy dispersion through a potential barrier with a height of V_0. Since Dirac fermions are superposition states of matter (electron or conduction band state) and anti-matter (hole or valence band state), an electron-like particle can shift into a hole like particle when it hits the potential barrier (potential well for a hole) and revet back to an electron state on the other side of the barrier [14]. Fig. 1.4(b) shows the transmission of carriers as a

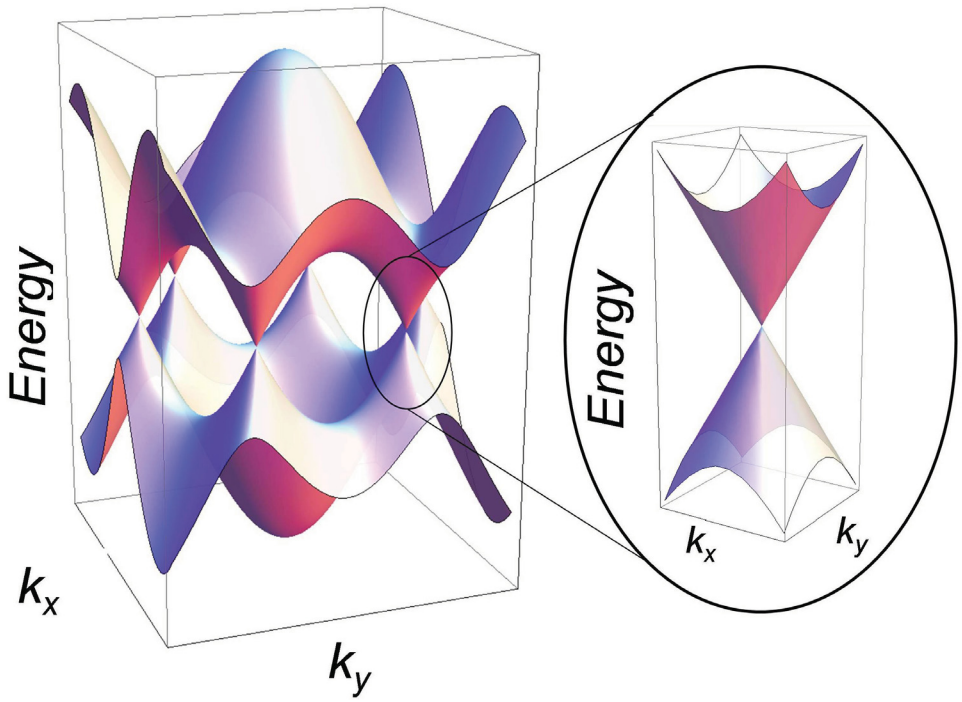

Figure 1.3: The tight-binging band structure of graphene. Energy of electronic states vs k_x and k_y. The inset shows that close to the $\mathbf{K} = (\frac{2\pi}{3a}, \frac{2\pi}{3\sqrt{3}a})$ and $\mathbf{K'} = (\frac{2\pi}{3a}, -\frac{2\pi}{3\sqrt{3}a})$ points is linear. Courtesy of Andrew McRae.

function of the incident angle. The transmission is perfect for an incident angle of $\theta \approx 0$, and drops quickly as the incident angle increases. This figure also indicates that the transmission at $\theta \approx 0$ is weakly dependent on V_0.

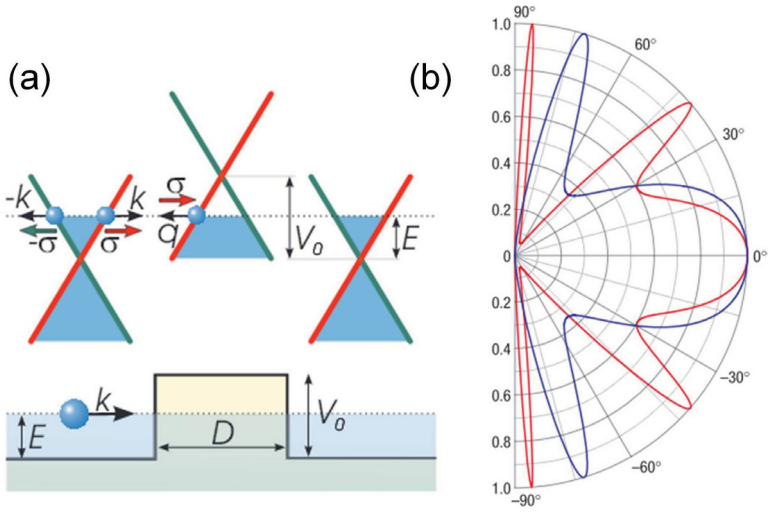

Figure 1.4: Klein tunneling in graphene. (a) Shows a cartoon of Klein tunneling for a Dirac fermion with an energy E and linear energy dispersion through a potential barrier with a height of V_0. (b) Transmission vs incident angle for two barrier heights 200 meV (red) and 285 meV (blue curve). Reproduced from reference [27].

Chapter 2

Fabrication of suspended gold-on-graphene break-junctions

We are interested in exploring the electronic properties of graphene at the 10-100 nanometer scale. This objective requires the delicate fabrication of clean and suspended graphene devices. Fig. 2.1(a) is a tilted SEM image of a suspended gold bowtie-shaped bridge covering graphene, where the center of the bowtie is $\approx$ 100 nm and is $\approx$ 500 nm at the base. These bowtie-shaped bridges are known as break-junctions. Fig. 2.1(b) shows a schematic indicating the geometry and structure of our completed devices. This suspended geometry allows us to tune the electronic properties of 10 nanometer scale graphene devices by changing the carrier density in graphene.

In this chapter we will discuss the multi-step fabrication process required to obtain such suspended gold bowtie-shaped bridges covering graphene. We will later break this bridge using an electromigration technique which will open a gap in the gold to expose a 10 nm section of graphene (see Fig. 2.1 (b)) [2, 28, 29]. We will explain the details of electromigration in chapters 3 and 4, since electromigration can be used either to tailor graphene down to a narrow quantum dot or a wide ballistic transistor. In this chapter, we will also demonstrate the instrumentation and electronics which we use to do low-temperature electron transport in our nanometer-sized graphene devices.

We will describe the microfabrication procedures required to create suspended

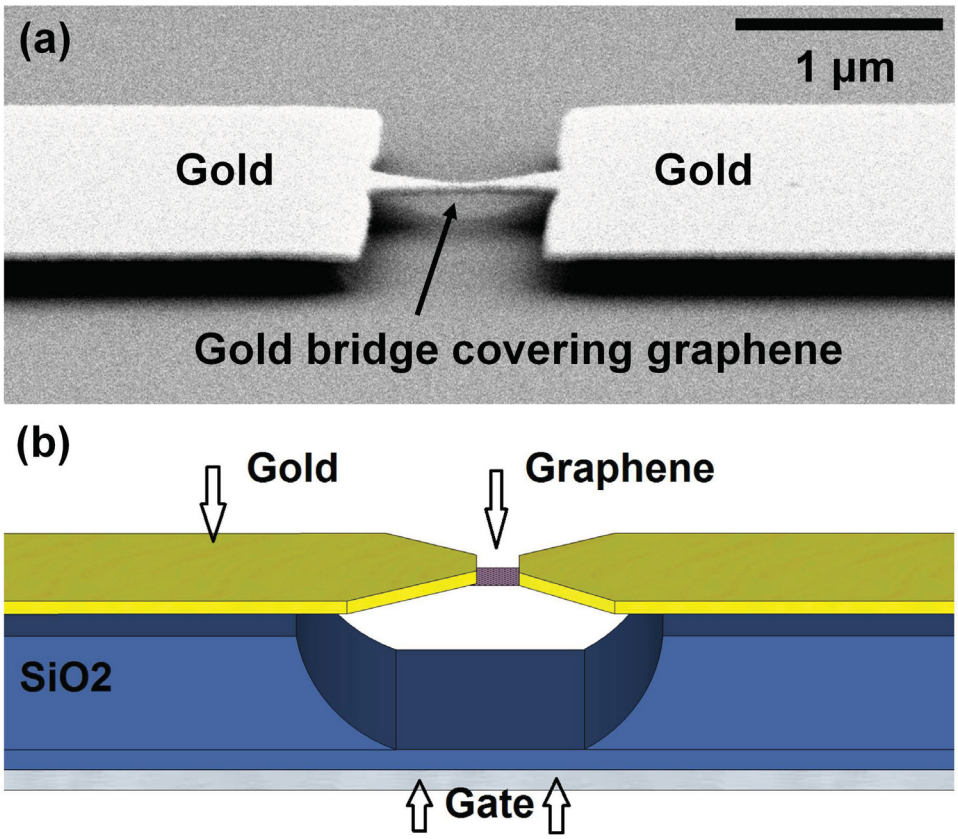

Figure 2.1: Suspended gold bowtie-shaped bridges covering graphene. (a) Tilted SEM image of a suspended gold bowtie-shaped bridges covering graphene (break-junction) before electromigration. A cartoon of the ultra short graphene device showing the graphene flake is suspended over etched SiO_2. Gold electrodes act as source and drain and the bottom Si layer works as gate electrode.

gold break-junctions covering graphene. This includes graphene deposition, locating graphene, making electrical contacts, wiring and packaging the devices.

We start with a 4" SiO_2/Si wafer upon which we build our devices. Using photolithography followed by metal evaporation, we define reference grids on the wafer which will help us to locate graphene after the deposition. We use optical microscopy and Raman spectroscopy to distinguish between single-layer and multi-layer graphene. We pattern gold break-junctions and gold contacts on the graphene flakes using electron beam lithography (EBL) followed by photolithography. We suspend our devices using a buffered oxide etch (BOE) to remove the silicon dioxide under the gold break-junction and suspend the bridge. Finally, we wire up and package our devices to be connected to BNC cables.

Fig. 2.1(a) and (b) demostrate our fabrication objective: an ultra small graphene device suspended over the back gate. The graphene channel acts as a field effect transistor with source, drain (gold contacts) and gate (Si layer) electrodes. Suspension decouples graphene from the disordered substrate. Moreover, graphene is anchored to the gold bridge from both sides and is free to vibrate, forming an ultra short graphene NEMS. Also, suspension reduces heat dissipation through the substrate and makes it possible to anneal the graphene flake by flowing a large current (as will be explained in Chapter 3).

2.1 Deposition and locating graphene

In this section we describe how to deposit graphene on a wafer, and create a reference grid to allow us to find and locate the flake. Then we discuss Raman spectroscopy and optical contrast ratio technique which allow us to identify single-layer graphene crystal.

2.1.1 Wafer back-side etching

We use 4" (100 mm) wide and 550 micron thick wafers. The wafers are made of highly doped Si covered by thin layers of 300 nm thermally grown SiO_2 on both sides. We use the conductive Si layer as the back-gate electrode. This requires removing the insulating layer of SiO_2 from the back side of the wafers to make electrical contact to the doped-Si layer. To do so, we use RIE etching to remove the SiO_2 layer.

RIE is an anisotropic dry etching method based on a reactive plasma. It uses radio

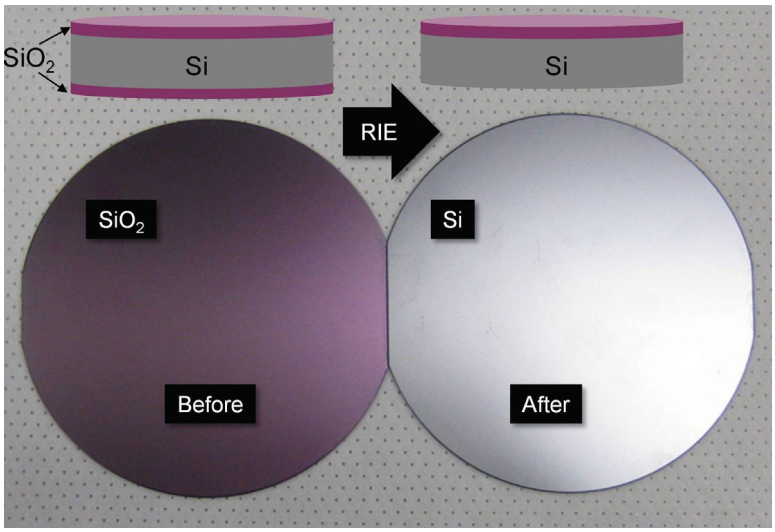

Figure 2.2: RIE etching a wafer. Image shows that after RIE process SiO_2 layer (purple color) is removed and Si layer (grey color) is visible. The top cartoon shows the cross section of the wafer before and after etching.

frequency (RF) voltage source to ionize and accelerate gas molecules inside a chamber into a reactive plasma. RIE etches the surface of materials through chemical and physical etching. The chemical etching results from the reaction between the ions and the surface, while the physical etching is the result of bombarding the surface with high energy molecules. The chemical etching is isotropic while the physical etching is highly anisotropic.

We start by cleaning the chamber with an O_2 plasma, using a 20 SCCM flow rate, a power of 300 W, and a pressure of 100 mTor for 15 minutes. Then we place the wafers face down in the RIE chamber, to etch the back side of the wafer while protecting the front side. We then flow a mixture of CHF_3 and O_2 gases, with flow rates of 22.5 and 2.5 SCCM respectively. In addition, the pressure and RF power are set to 100 mTorr and 300 W respectively. We etch for 15 min then, the chamber is purged 3 times with N_2 and the samples are taken out. The Si layer has a distinct grey color compared to the purple color of the SiO_2, which allows a visual confirmation that SiO_2 has been removed. Fig. 2.2 shows the back side of a wafer before and after RIE etching. We measure the thickness of SiO_2 with ellipsometry to ensure that the SiO_2 film has been removed.

2.1.2 Ellipsometry

We use ellipsometry to measure the thickness of the SiO_2 film. Ellipsometry takes advantage of the change in polarization between the incident and reflected light from a thin film in order to measure its thickness. Fig. 2.3 shows an ellipsometer with a UV polarizer and analyzer. The wafer is placed and aligned on the stage so that the reflected light reaches the four detectors in the analyzer. The software can extract the thickness of the film by comparing the change in polarization between the reflected and incident light. After RIE etching the backside of our wafers we use the ellipsometer to confirm that there is no oxide left.

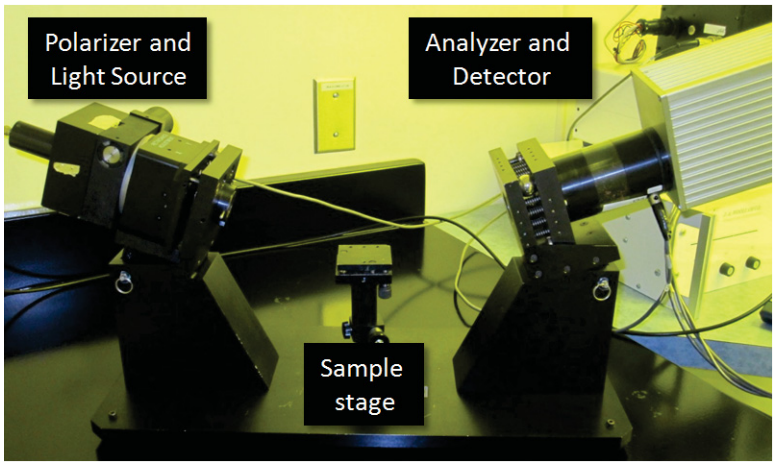

Figure 2.3: Ellipsometry measurement. Ellipsometry measures the change in polarization between incident and reflected light from a thin film to characterize a thin film. We use ellipsometry to measure the thickness of the SiO_2 film.

2.1.3 Photolithography of reference grids

We create reference grids on the wafers to create precise micron-scale coordinate systems, which will later be used to locate graphene crystal. We use photolithography to fabricate reference grids on the SiO_2/Si wafer. Fig. 2.4 shows a 4" wafer with reference grids. We divide 4" wafers in 5×5 mm chips. Each chip has a 4×4 mm grid which includes letters, numbers and $\ulcorner$ shapes to divide the 4×4 mm area into

100×100 μm squares.

Photolithography is a typical technique used to define a micron-size pattern on

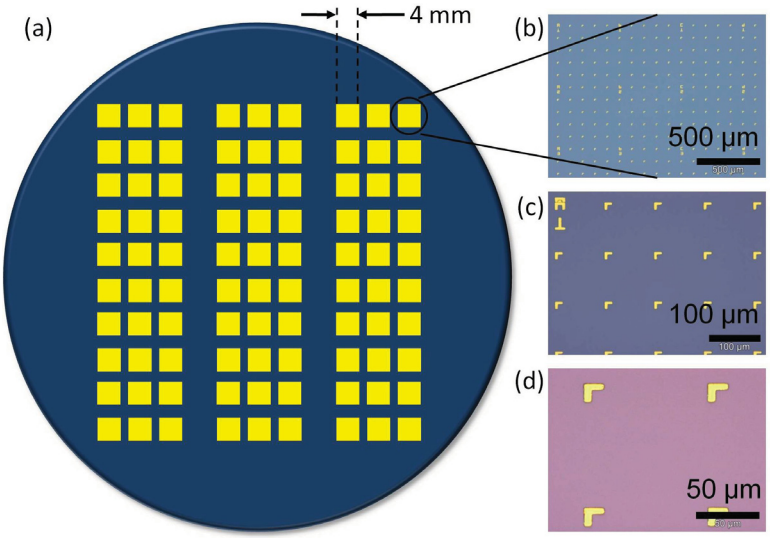

Figure 2.4: Photolithography pattern. Using the photolithography mask we designed, we can make 90 grids on each 4" wafer panel (a). The size of each grid is 4×4 mm and contains letters, numbers and $\ulcorner$ shapes, panel (b) and (c). $\ulcorner$ shapes divide the grid to 100×100 μm squares, panel (d).

a substrate. The substrate is spin-coated by a thin layer of photo-sensitive material called photoresist. Then, the substrate is covered by a mask with a pre-defined pattern and exposed to UV light. The exposure changes the chemical properties of the photoresist and makes it more or less soluble (positive or negative resist) in a developer. Developing removes the exposed photoresist and results in the transfer of the mask pattern to the resist. Fig. 2.5 shows the different steps of photolithography.

We spin-coat S1813 as a positive resist on 4" wafers at 4000 rpm for 30 seconds, with a ramping acceleration of 456 rpm/s^2. This results in a uniform thickness of about 1.5 μm. After the spinning process, we soft-bake the sample on a hotplate at 115^o C for 60 seconds and let the sample cool down for a few minutes. The hard-contact mode is used to bring the wafer in contact with the mask. Given the thickness of the resist and the size of the pattern, the exposure dose is chosen to be ≈ 40 mJ/cm^2. After exposure, the wafer is soaked in photoresist developer MF-318 for 60 seconds followed by rinsing with deionized water to remove the developer. Optical microscopy is used to check the quality of the process.

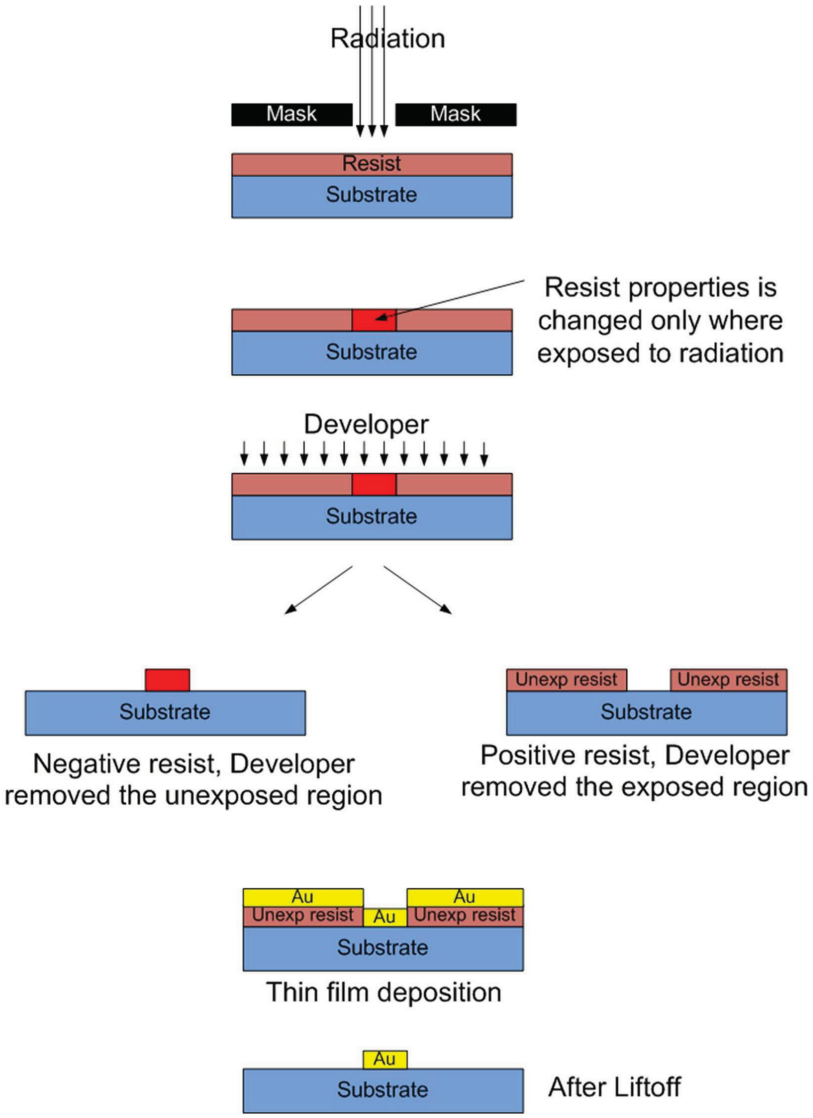

Figure 2.5: Photolithography procedure. Cartoon of the photolithography procedure from exposure to metal lift-off. Photoresist is spin-coated and baked on the wafer to form a thin layer. Then, the substrate is covered by a mask with a pre-defined pattern and exposed to UV light. A developing agent removes the photoresist where it was exposed. A thin film of a metal is evaporated on the sample. Finally, the sample is put into a warm solvent (usually acetone) which dissolves the photoresist and lifts-off the metal layer, except where it sits directly on the substrate.

2.1.4 Metal deposition

After the photoresist is developed we deposit a thin layer of metal, usually gold, on the developed sample to create a visible and permanent reference grid. Fig. 2.6(a)-(c) show the thermal evaporator, RF sputterer and E-beam evaporator which we use for metal deposition. The thermal evaporator and RF sputterer are very useful for a quick metal deposition for micron sized lithography patterns, and the E-beam evaporator provides a wider range of deposition material. We deposit 5 nm of Ti (or Cr) followed by 80 nm of gold for reference grids. The Ti or Cr layer is as an adhesive layer between the gold and SiO_2 film. After deposition of the metal, the wafer is placed in a warm solvent (usually acetone) which dissolves the photoresist. It lifts-off the metal layer except where it sits directly on the substrate. Fig. 2.6 (d) and (e) show the sample after development and after metal lift-off, respectively.

2.1.5 Graphene crystals: Deposition and measurement of the number of layers

We use mechanical exfoliation [15, 30] to deposit graphene crystal on 5×5 mm SiO_2/Si chips. This method makes the highest quality graphene reported and provides some single-layer crystals of several microns. We start by placing a few millimeters-sized pieces of Kish Graphite on Scotch tape. Then, we fold the tape and smooth it out with tweezers to remove any air pockets. Peeling apart the tape cleaves the graphite flakes into thinner and thinner flakes. We do this repeatedly, 15 to 20 times. At last, we stick the tape on the chip and use tweezers to smooth it out. After waiting 10 min, we gently peel-off the tape from the chip. Using optical microscopy, we identify and locate the graphene flakes. A single layer of graphene is not visible on most substrates, but has good contrast on a 300 nm-thick SiO_2 layer on top of Si. A single layer of graphene can change the reflection of the light from the substrate and slightly modify the contrast so that the graphene becomes visible under optical imaging [31]. Fig. 2.7 shows some single and bilayer graphene flakes that we deposited and located with respect to reference grids.

Data extracted from the CCD camera, which is mounted on the optical microscope, can be analyzed to distinguish the number of layers of graphene flakes, as we will discuss here. Fig. 2.8(a) shows our BX51M Olympus optical microscope equipped

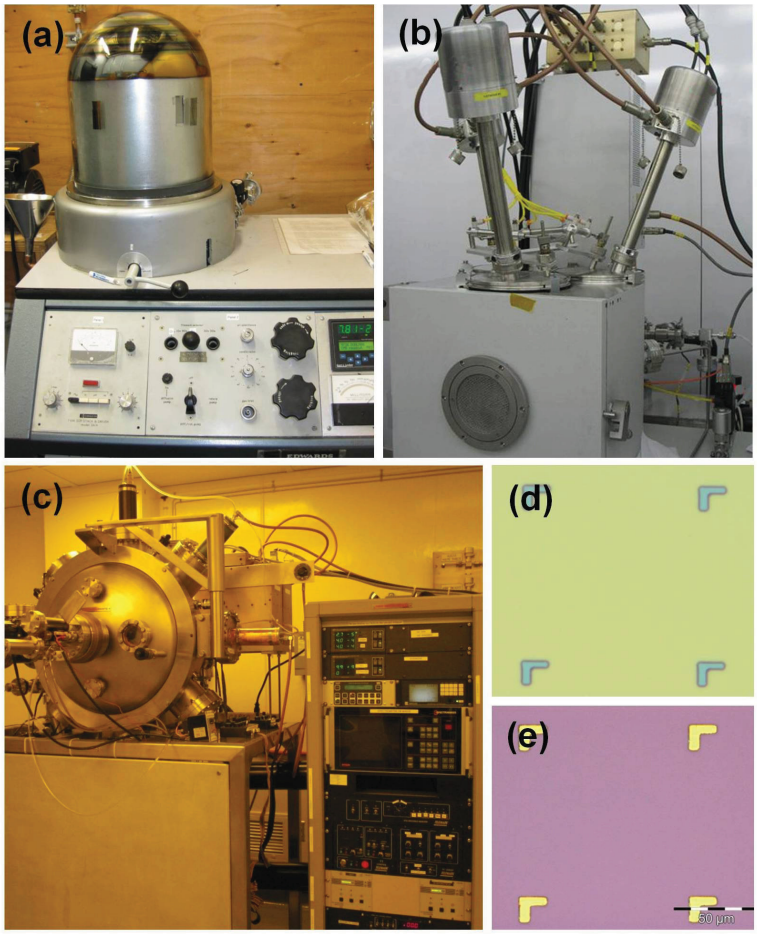

Figure 2.6: Metal deposition. (a), (b) and (c) show the thermal evaporator, RF-DC Sputterer and electron beam evaporator respectively that we use for metal deposition. (d) Optical image of a sample before metal deposition (after development). (e) Optical image of a sample after lift-off.

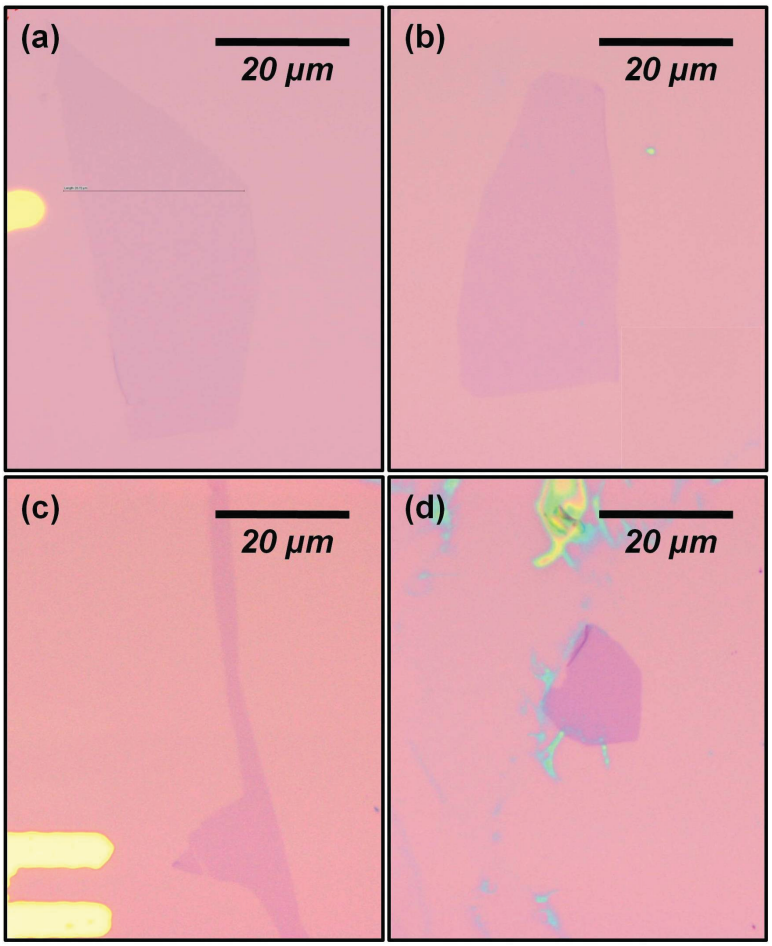

Figure 2.7: Optical characterization of graphene. Optical images of graphene flakes deposited on SiO_2/Si chips using the mechanical exfoliation technique. (a),(b)and (c) are single-layer graphene flake and (d) is a bilayer flake (confirmed by Raman spectroscopy and contrast ratio analysis.)

with a CCD camera which we use to locate and identify graphene crystals. It allows us to extract the individual intensity of red, green and blue light s as well as the total intensity at each pixel. Fig. 2.8(b) shows an interesting flake with different thicknesses. The number of layers is reasonably easy to estimate due to the geometry of the flake. The reflected intensity for red, green, blue and total ($I_{total} = (I_{Red} + I_{Green} + I_{Blue})/3$) are extracted along the dashed lines shown in Fig. 2.8(b). Fig. 2.8(c) shows how the intensity of different colors changes along line 1 in Fig. 2.8(b). Black dashed lines in Fig. 2.8(c) indicate where the flake starts and ends. We use contrast ratio [32] to see how the average intensity changes for the pixels taken on the flake compared to the pixels taken on the background substrate. The contrast ratio is defined as:

$$C = \left| \frac{I_{on the flake} - I_{background}}{I_{background}} \right| \tag{2.1}$$

In Fig. 2.8(d) we plot the contrast ratio for red, green, blue and total light. The contrast ratio for green and total light are quantized and scale linearly with the number of layers in Fig. 2.8(b). We used this method for different flakes of different thicknesses. We found a good agreement between the extracted number of layers in the flake with the results from Raman spectroscopy. This method is an easy and quick way to measure the number of layers in a flake [32].

We discuss Raman spectroscopy as another technique to count the number of layers in graphene crystals. Raman spectroscopy is based on inelastic scattering of visible light from a crystal. The frequency shifts of the scattered light provides information about the phonons or vibronic modes of the system.

Fig. 2.9(a) shows the Raman shifts for single and bi-layer graphene [33]. The Raman spectrum of graphene has four major peaks, G, D, G' and D'. The G peak is around 1582 cm^{-1} and arises from the in-plane optical phonons of graphene. The D peak is around 1350 cm^{-1} which is strongly dependent on the disorders within the flake and shifts to higher frequencies with increasing laser excitation. The D' peak is around 2700 cm^{-1} and is an overtone of the D peak. The G' peak is around 3248 cm^{-1} and is an overtone of the G peak [33, 34, 31]. These peaks not only give information about the number of layers, but the stacking of the layers as well [34].

Fig. 2.9(b) and (d) show the evolution of the G peak with an increasing number of layers [33, 34]. In graphene, the G peak position is around 1585 ± 1 cm^{-1} which is about $3-5$ cm^{-1} higher than in graphite (1582 ± 1 cm^{-1}). The G peak for bi-layers is

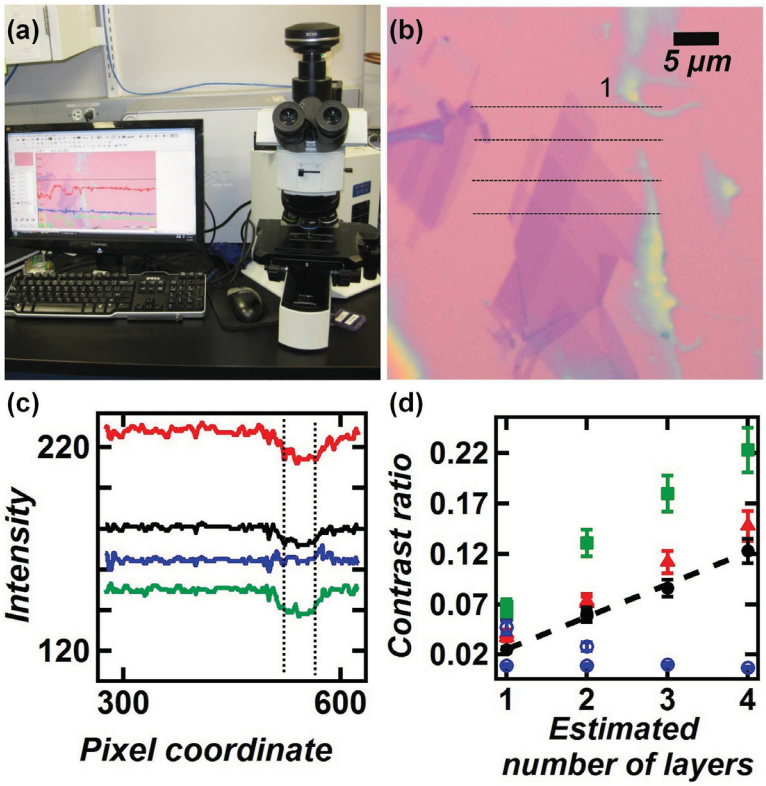

Figure 2.8: Optical contrast of graphene. (a) Our BX51M Olympus optical microscope equipped with a CCD camera and Analysis Imager software. (b) Optical image of a flake with different thicknesses. (c) Individual intensity of red, blue, green and total light versus the pixel coordinates. The data were extracted from the flake shown in (b) along line 1. (d) Intensity ratio for red, green, blue and total light are plotted versus the number of layers for the flake shown in (b). The dashed line is the linear fit to the data for total light. The data are extracted along the dashed lines in (b) to compare the contrast ratio of different colors for different thicknesses.

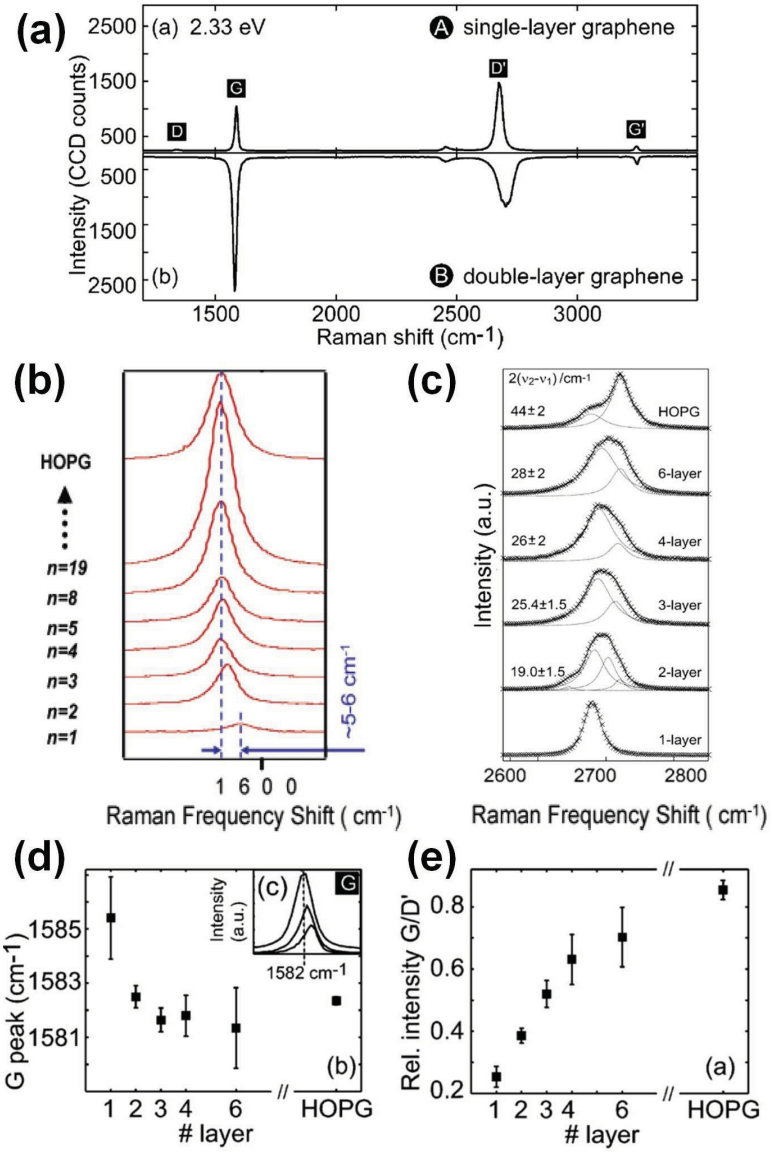

Figure 2.9: Raman spectrum of graphene. (a) Raman spectrum of single-layer graphene (top) and bilayer graphene (bottom). Reproduced from reference [33]. (b) and (c) show the evolution of the G and D' peaks as the number of layers increases. Reproduced from reference [33, 34]. (d) Indicates the shift of the G peak as the number of layers increases. (Inset shows the G peak for single(bottom), bilayer (middle) and graphite (top)). (e) Shows that the ratio of the integrated intensities of the G and D peaks increases almost linearly when the number of layers increases from one to four layers. Reproduced from reference [33].

also located at 1581 ± 1 cm^{-1}. Fig. 2.9(c) shows the evolution of the D' peaks with an increasing number of layers [33, 34]. Graphene has a single sharp D' peak at 2678.8 ± 1 cm^{-1} but the bilayer has a broader D' peak which contains four components. The two innermost peaks are positioned at 2683 ± 1 cm^{-1} and 2701.8 ± 1 cm^{-1}. The intensity of the D' peak significantly decreases with a decreasing number of layers. D' in graphite is small, broad, and contains two inner peaks. Fig. 2.9(e) also shows the behavior of the ratio of the integrated intensities of G/D' peaks as a function of the number of layers [33]. This ratio changes almost linearly as the number of layers increases from one to four layers.

We use a Raman microscope with an excitation laser at 514 nm. Trying different power and exposure times, we obtained a excellent result with power = 25 μW and a 50 second exposure time. Fig. 2.10 shows the Raman spectrum for single-layer graphene, bilayer graphene and graphite. Fig. 2.10 (a)-(c) show the Raman spectrum of single-layer graphene. The G and D' peaks are positioned at 1583 ± 1 cm^{-1} and 2678 ± 1 cm^{-1} respectively. The ratio of the integrated intensities of the G/D' for this flake is about 0.18, which is in agreement with the reported spectrum for single-layer graphene. Fig. 2.10(d)-(f) show the spectrum for a bilayer graphene flake. The G and D' peaks are positioned at 1581 ± 1 cm^{-1} and 2699 ± 1 cm^{-1} respectively. We can almost distinguish the four components in the bilayer D' peak. The ratio of the integrated intensities of the G/D' is about 0.32 which is close to the expected value for a bilayer. Fig. 2.10(g)-(i) show the spectrum for a thick graphite crystal. The G and D' peaks in the graphite flake are located at 1582 ± 1 cm^{-1} and 2726 ± 1 cm^{-1} respectively. The shape of the D' peak is very similar to the theoretical prediction. The ratio of the integrated intensities of the G/D' is about 0.74 which is very close to the expected value. We use Raman spectroscopy to distinguish single and bilayer graphene flake which we located using optical microscopy. Compared to AFM and optical spectroscopy, Raman spectroscopy is a more powerful and reliable way to distinguish single-layer and bilayer graphene crystals. It is the best way to count the number of layers in the flake due to their specific fingerprints.

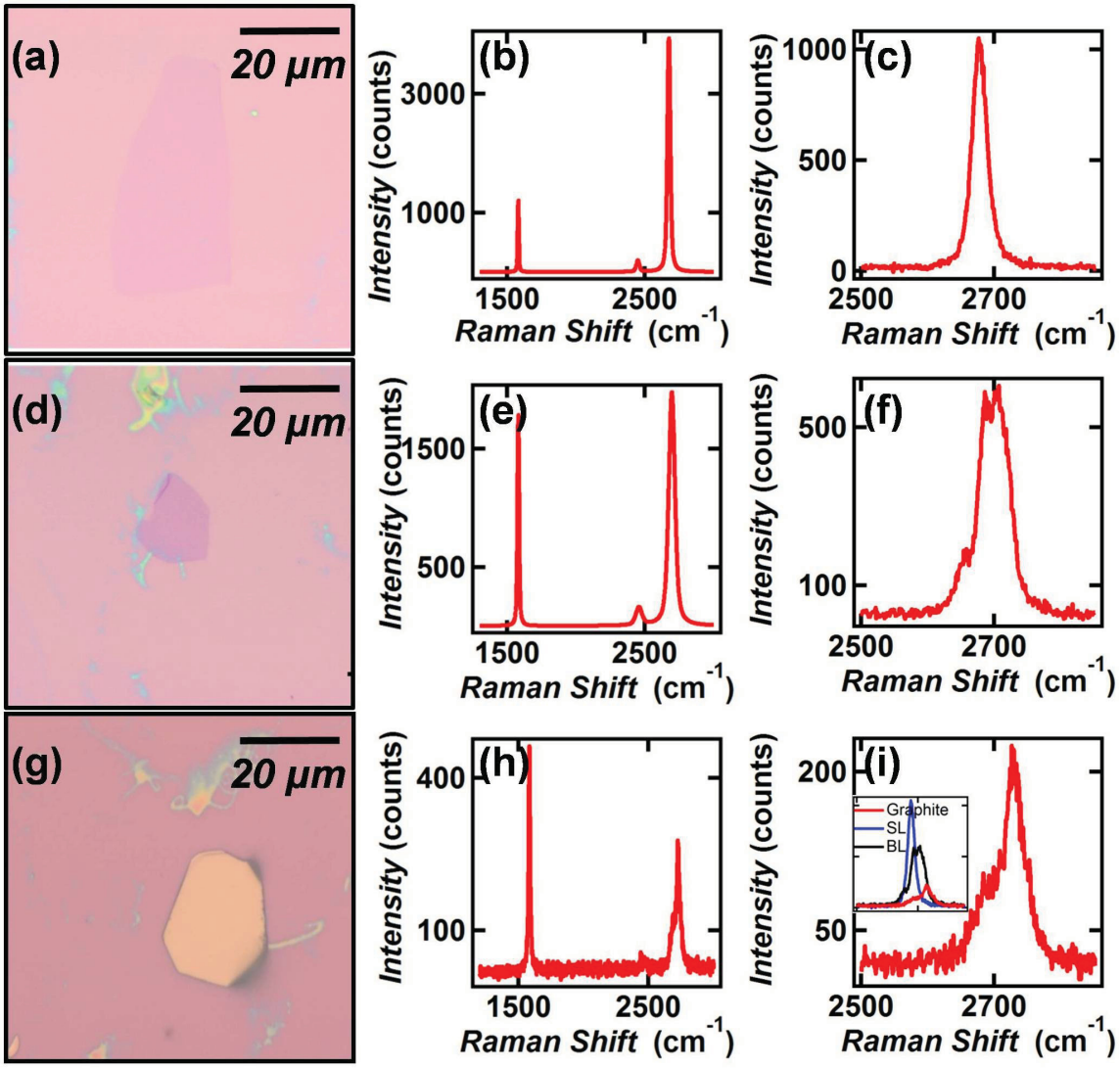

Figure 2.10: Raman spectrum of our graphene flakes. (a) Optical image of single-layer graphene. (b) Raman spectrum of single-layer graphene flake in (a). (c) Zoom-in on the D' in (b). (d) An optical image of a bilayer graphene flake. (e) Raman spectrum of the bilayer shown in (d). (f) Zoom-in on the D' peak in (e). (g) Optical image of a graphite flake in (g). (h) Raman spectrum of the graphite flake. (i) Zoom-in on the D' peak. Inset in (i) the D' peak of single-layer graphene (blue), bilayer graphene (black) and graphite (red).

2.2 Making gold break-junctions

In this section we will explain the fabrication steps required to make suspended gold break-junctions covering graphene. We use electron beam lithography to generate gold break-junctions on graphene. Using photolithography, we connect electrical contacts to the break-junctions. Then, we remove the graphene which is not covered by the gold break-junction with O_2 plasma. Finally, we use HF acid to etch some of the SiO_2 substrate to suspend the gold break-junction.

2.2.1 Electron beam lithography

Electron beam lithography (EBL) is a technique used to define nanometer scale patterns and circuits. The principle is the same as photolithography, except that it uses an electron beam and electron sensitive resist instead of photoresist. In EBL, the desired pattern is designed in a Design CAD software and converted using the pattern generator software. An EBL generator focus the electron beam on the substrate and trace the pattern define in the CAD design to expose the resist. Alignment of the nanometer scale break-junctions on graphene is crucial at this stage. We use ⌜ shapes made in section 2.1 to find the exact location of the graphene flakes and also align the CAD designed break-junctions on top of them. After exposure, the sample is developed in an EBL developer and metal film is deposited, followed by lift-off. Fig. 2.11 shows the geometry of some of our e-beam patterns. Using EBL we generate two kinds of patterns: break-junctions (see Fig. 2.11(a),(b) and (c)) and short length gap junctions. Fig. 2.11(a) shows an optical image of three break-junctions on top of graphene. Fig. 2.11(b) and (c) show zoom-in SEM images of the three break-junctions shown in (a). Fig. 2.11(d) indicates the geometry and dimensions of a break-junction. The center of the break-junction needs to be the narrowest section of the entire circuit, since it will electromigrate from here as a result of its high resistance (will be explained in Chapter 3). Gap junctions are two rectangular contacts with a spacing of 100 nm up to a micron. Optical and zoom-in SEM images of 100 nm long gap junctions are shown in Fig. 2.11 (e) and (f).

We prepare our samples for EBL by spin-coating 5×5 mm chips by electron beam resist. We use single and double layer resist for different resolutions. Since the thickness of the metal deposition has to be at least three times thinner than the resist,

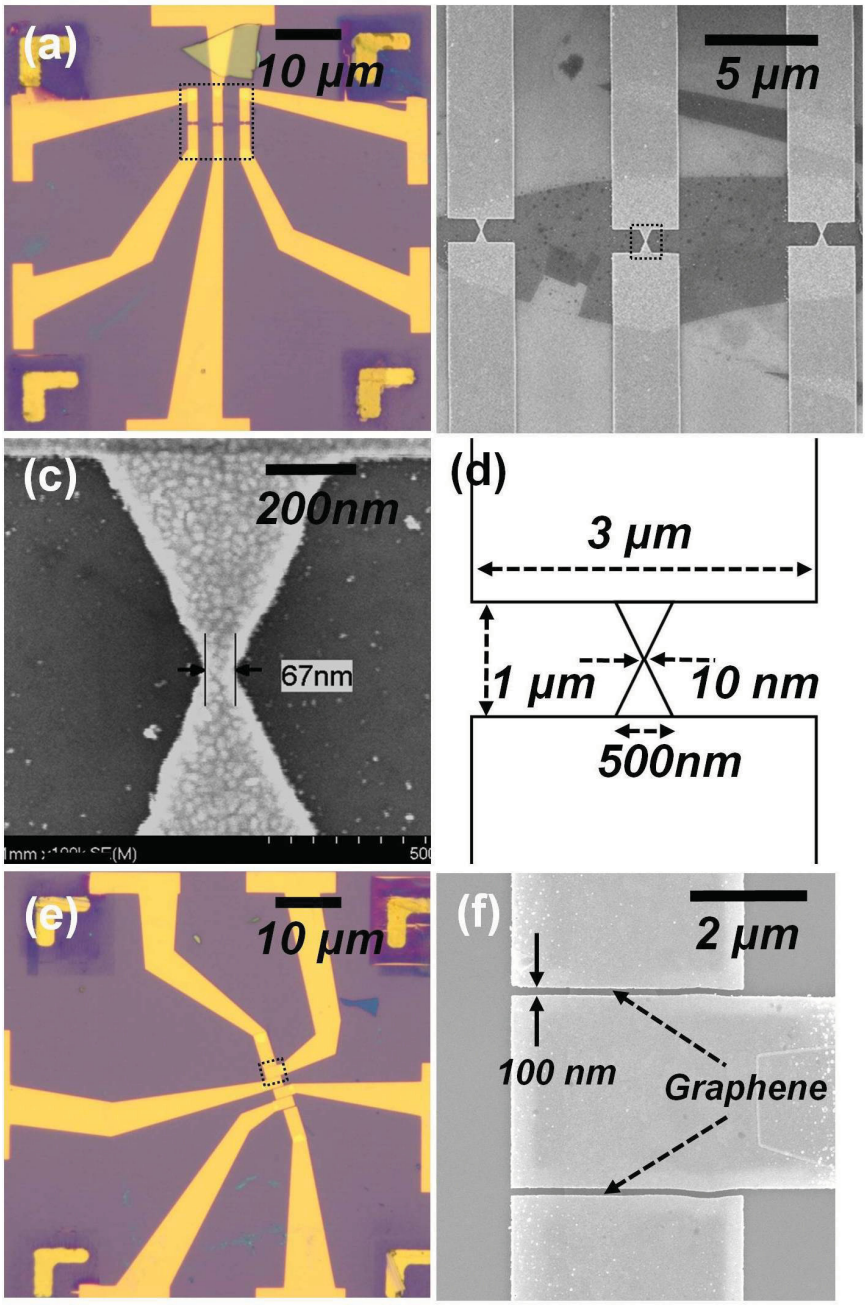

Figure 2.11: Electron beam lithography patterns. (a) Optical image of three gold break-junctions fabricated by EBL on top of a graphene flake. (b) SEM image of the three break-junctions shown in the dashed box in (a). (c) Zoom-in view of the break-junction shown in the dashed box in (b). (d) The CAD design dimensions and geometry of the break-junction. (e) Optical microscopy image of 100, 200 and 300 nm gap junctions made by EBL on graphene. (f) SEM image of the 100 nm gap junction shown in the dashed box in (e).

thinner resist can be used for thinner metal films. Thinner resist allows a higher resolution. We use Copolymer EL9 (9% in ethyl lactate) and PMMA A4 (polymethyl methacrylate 4% in anisole) as a bilayer resist, or a single layer of PMMA A4 for the highest resolution. Both resists are spin-coated for 60 seconds at 3000 rpm and baked at 170° C for 15 min. This gives copolymer and PMMA thicknesses of ≈300 nm and ≈200 nm respectively. After EBL exposure we develop the chips in a solution of 1:3 MIBK:IPA for 30 seconds, then quickly transfer them to methanol for 15 seconds and finally rinse with IPA. EBL is followed by a 40 nm gold deposition and lift-off. We do not use any adhesive layers such as Ti or Cr in this step. Adhesive layers leave an undesirable film during the electromigration process and contaminate the graphene channel. The electromigration procedure will be discussed in chapter 3.

Later in this chapter we will show how we interconnect the nanometer-sized break-junction to the centimeter-sized BNC cables and measuring electronics.

2.2.2 Contact pads

The EBL pattern is too small to connect to macroscopic electronics. Thus, we first connect micron scale gold arms to the nanometer scale EBL pattern. For this purpose we make use of another photolithography step which attaches 300 μm long arms and 200×200 μm square pads to the EBL pattern. Fig. 2.12 shows the photolithography pattern connected to the EBL pattern. This photolithography step is followed by a 5 nm Ti/ 80 nm gold deposition and lift-off. Another reason for using this additional lithography step is that the EBL pattern is made of only 40 nm thick gold with no adhesive layer (Ti or Cr,) which makes it difficult to wire-bond (see next section). The samples must be tested in this multi step fabrication process. After connecting the 200×200 μm square pads to the EBL pattern, we may test the sample. Using a probe station, we measure the resistance of each junction. The resistance range should be about 50 Ω for ≈ 100 nm wide break-junctions. We repeat this step to test the samples one by one throughout the fabrication process until the sample is loaded in the cryostat. Fig. 2.13(a) shows the probe station and (b) two probes connected to the photolithography pads for electronic testing.

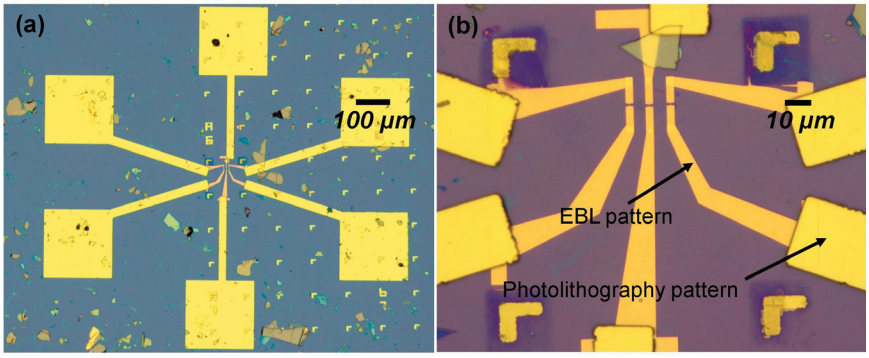

Figure 2.12: Large contact pads. (a) Optical image of photolithography contact pads (200×200 μm) with 300 μm long arms and 200×200 μm square pads. (b) Optical image of the interconnections between the contacts pads and the EBL pattern.

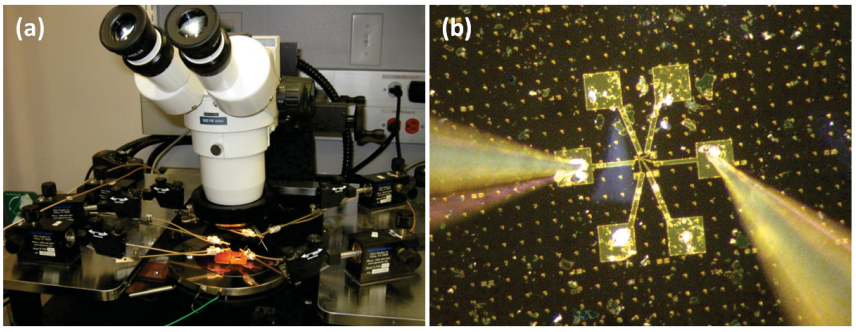

Figure 2.13: Probe station set-up. (a) Image of the electrical probe station that we use to test the samples. (b) Probes are contacted to the sample via the 200×200 μm square pads.

2.2.3 Graphene etching

The break-junction samples are built on top of micron-sized graphene flakes. To prepare the junctions for electromigration and make a nanometer sized graphene junctions, we have to remove the portion of graphene which is not covered by the gold break-junctions (see Fig. 2.14). To do this we expose the sample to an oxygen plasma. The O_2 plasma etches the graphene completely, except where it is masked by the gold break-junction. We use a 20 SCCM flow rate of oxygen, a chamber pressure of 200 mTorr and a power of 300 W for 45 seconds. Fig. 2.14 shows SEM images of a sample before and after O_2 plasma.

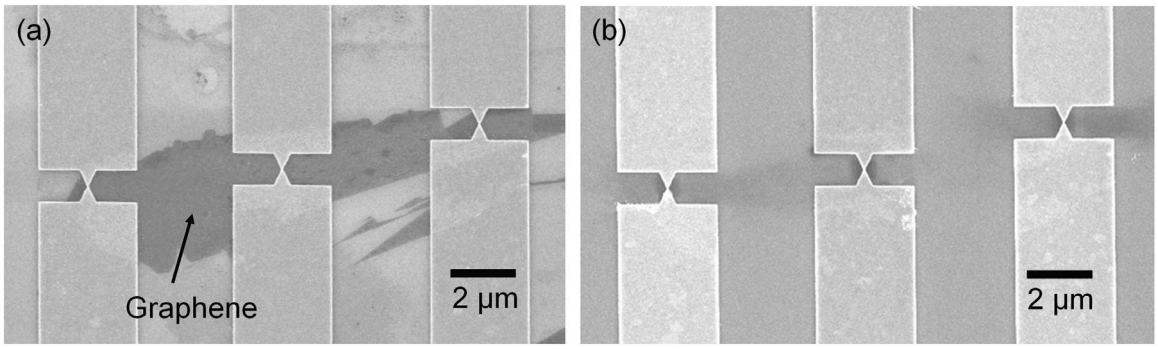

Figure 2.14: Removal of graphene by oxygen plasma. (a) SEM image of three break-junctions on top of a graphene flake before oxygen plasma. (b) The same sample after oxygen plasma. Graphene has been removed by the oxygen plasma where it was not masked by the gold break-junctions.

2.2.4 Suspension of the gold break-junctions

After the O_2 plasma etch, the samples are ready for suspension. The suspension is not only to decouple devices from the substrate's electrostatic disorders, but also to provide a mechanical degree of freedom to the device, which can be used to study the electromechanical properties of the device, as well as to thermally decouple the graphene from the substrate.

A buffered solution (BOE) of HF (hydrofluoric acid) is used to etch the SiO_2 beneath the gold bridge and graphene. Fig. 2.15 (a) shows a tilted-SEM image of suspended gold break-junctions. Suspending graphene devices is a challenging process since the HF solution etches the SiO_2 under graphene much faster than bare SiO_2. It

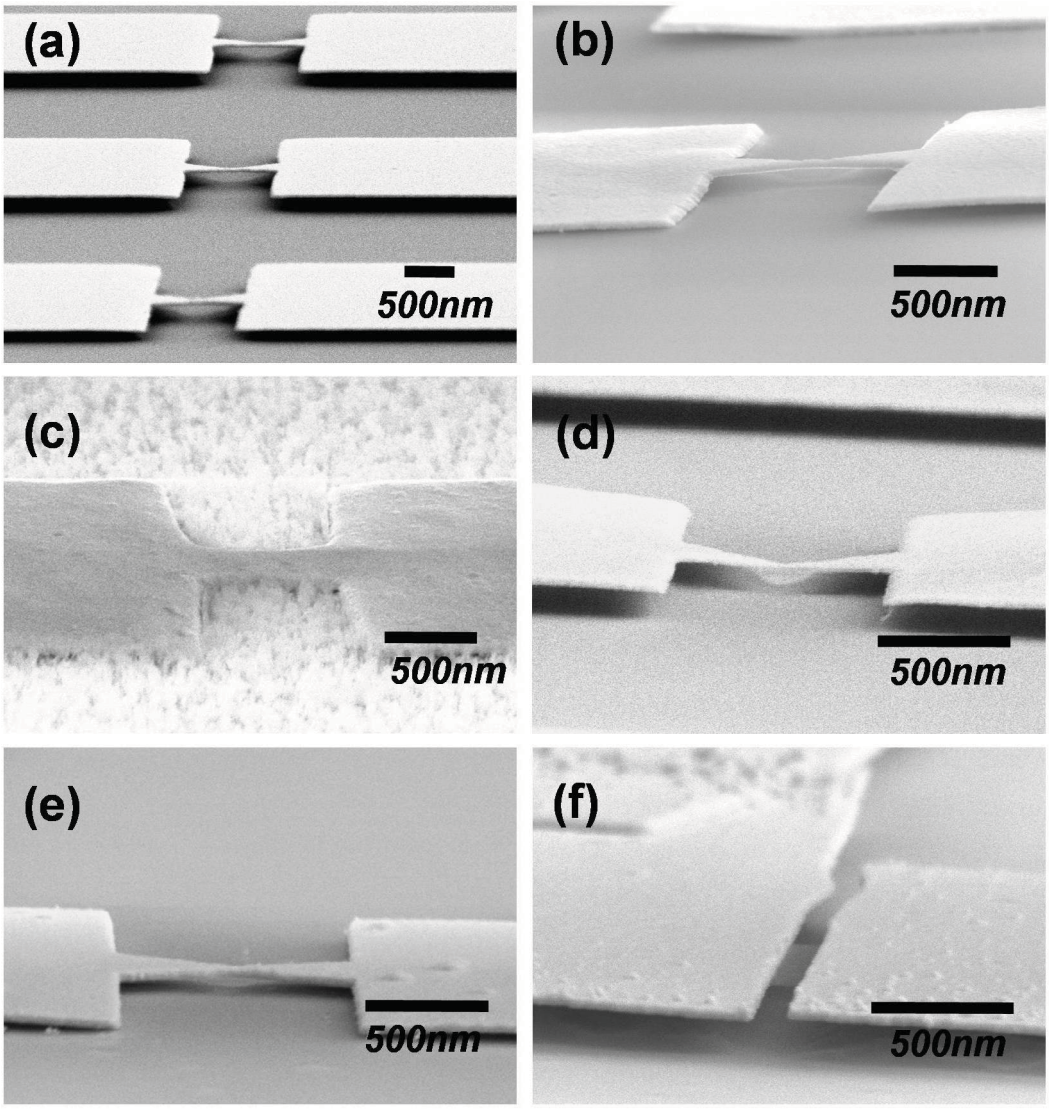

Figure 2.15: Suspension of gold break-junctions. (a) Tilted-SEM image of suspended gold break-junctions with no graphene underneath. The sample is etched 75 nm vertically (1 min in the solution). (b) Image of a break-junction on graphene. Sample is also etched 75 nm vertically. (c) Tilted-SEM image of a break-junction etched using HF vapor for 20 min at 45° C. (d) Image of a suspended break junction on graphene, etched using a two step process of RIE for 80 nm and BOE for 70 nm. (e) A suspended break junction on graphene, BOE (1:7 ratio of 49%HF:NH4F) etched for 25 nm. (d) Image of a suspended gap junction on graphene. Sample is BOE (1:7 ratio of 49%HF:NH4F) etched for 145 nm.

makes the etching rate in the horizontal direction under graphene much faster than in the vertical direction. The thickness of the gold bridges is only 40 nm, such that suspending the bridge over a long distance can cause the entire bridge to collapse. Fig. 2.15 (a) and (b) show tilted SEM images of suspended gold break-junctions with no graphene and with graphene respectively. Both sample are etched for 75 nm (1 min in the solution). Break-junctions with no graphene are uniformly suspended. However, break-junctions on graphene are not uniformly etched due to the fact that the SiO_2 film was etched much faster horizontally.

We tried different techniques to find the best method of suspension. Fig. 2.15 (c) is a tilted SEM image of a sample which was etched using HF vapor. The result was not very interesting since the etching of the surface was quite rough. Fig. 2.15 (d) shows a suspended junction using a combination of dry and wet etching. We used RIE followed by HF etching. RIE etches the SiO_2 vertically, except where it is masked by gold, while HF etches the SiO_2 both horizontally and vertically, resulting in suspension of the gold bridge. The suspension looks reasonable but the resistance of the samples was too high after this step. This might be due to RIE induced to damaged the gold break-junctions.

We found that using a buffered solution of HF gave the best yield. This buffered solution, BOE, consisted of a 1:7 ratio of 49%HF:NH4F. We measured and calibrated the etching rate of BOE for different times. The thickness of the SiO_2 film was measured precisely using ellipsometry to find the etching rate. After measuring the precise etching rate, the required time of etching is calculated for each sample. The samples were placed into the solution for the calculated time and then quickly transferred to DI water. Finally, the samples were soaked in IPA and gently dried with a nitrogen gun. Fig. 2.15 (e) and (f) show tilted-SEM images of a suspended break-junction and a gap junction respectively. We used the same solution to etch the break-junction in (e) and the gap junction in (f) for 25 nm and 145 nm respectively.

2.3 Packaging the sample

In this section, we will explain how we package the devices so that they can be connected to the centimeter scale BNC cables and measurement electronics. We dice and mount our chips into a chip carrier (see Fig. 2.16(a)) and, use a wire bonder

to connect the gold pads of the samples to the chip carrier's pins. Finally, the chip carrier is mounted into a cryostat for measurement.

2.3.1 Wire-bonding

We explained in subsection 2.2.2 how we connect the nanometer scale EBL pattern to the micrometer scale photolithography pattern. Here, we show how we interconnect the micrometer scale photolithography pattern to a centimeter chip carrier.

We use a wire bonder (uses ultrasonic power) to weld thin (25 μm) Al wires to

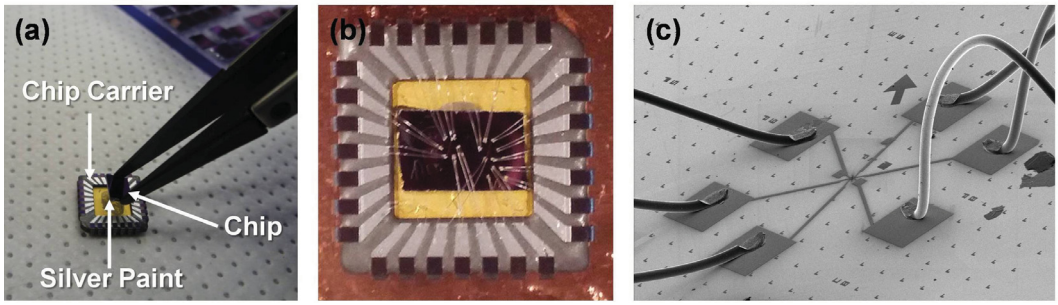

Figure 2.16: Wire bonding. (a) Image of mounting the chip in the chip carrier using silver paint courtesy of Andrew McRae. (b) Image of a wire bonded chip. Photolithography square pads are connected to the chip carrier using Al wires. (c) Tilted SEM image of a wire bonded chip. Bonds are connected from the square pads to the chip carrier pins.

the gold contact pads of our samples to the chip carriers contacts. Fig. 2.16 shows the wire bonding steps. A 5×5 mm chip is mounted into a chip carrier using silver paint. Silver paint is a conductive glue that we use to make a connection between the Si layer (on the back side of the chip) and the gold pad of the chip carrier to make the back gate electrode. Once the chip is mounted to the chip carrier, we use the wire bonder to weld the Al wires from the photolithography pads to the pins of the chip carrier. Fig. 2.16(b) shows an image of a wire bonded chip. We sometimes use double bonds to each pad to have more robust contacts. Fig. 2.16(c) shows a zoom-in tilted-SEM image of the Al wires attached to the photolithography pads. After wire bonding, the chip carrier is mounted into the cryostat. Throughout the wiring procedure, it is crucial to be electrically grounded to prevent electric discharge which would destroy the nanometer size break-junctions (extremely small "fuses").

2.4 Cooling down to low temperatures

Most of the exciting physics in graphene, briefly described in Chapter 1 and on which we will elaborate later, happens at low energies. Thus, to explore these delicate electronics and suppress the noise from thermal fluctuations we have to cool down the samples. We use different methods and cryostats to cool down the samples. Fig. 2.17 (a) shows a liquid helium (LHe) dewar with a top-loaded electronic measurement stick. Using a LHe dewar is a quick method to reach 4.2 K. It is also very easy and convenient to load and unload the sample for testing purposes and data acquisition. Fig. 2.17(b) shows our He-4 cryostat. The He-4 cryostat uses LHe-4 to cool down the sample. It provides high cooling power and has been designed in such a way that the sample space can be pumped down to high vacuum. It also has a 14 Tesla superconducting magnet (0-14 Tesla) which allows temperature control from $1.5-420$ K. Fig. 2.17 (c) shows our He-3 cryostat which can cool the samples down to 0.3 K. It also has a 9 Tesla superconductive magnet. The He-3 cryostat does not require any LHe refilling. It uses close cycle He-4 and He-3 gases to reach a base temperature of 0.3 K.

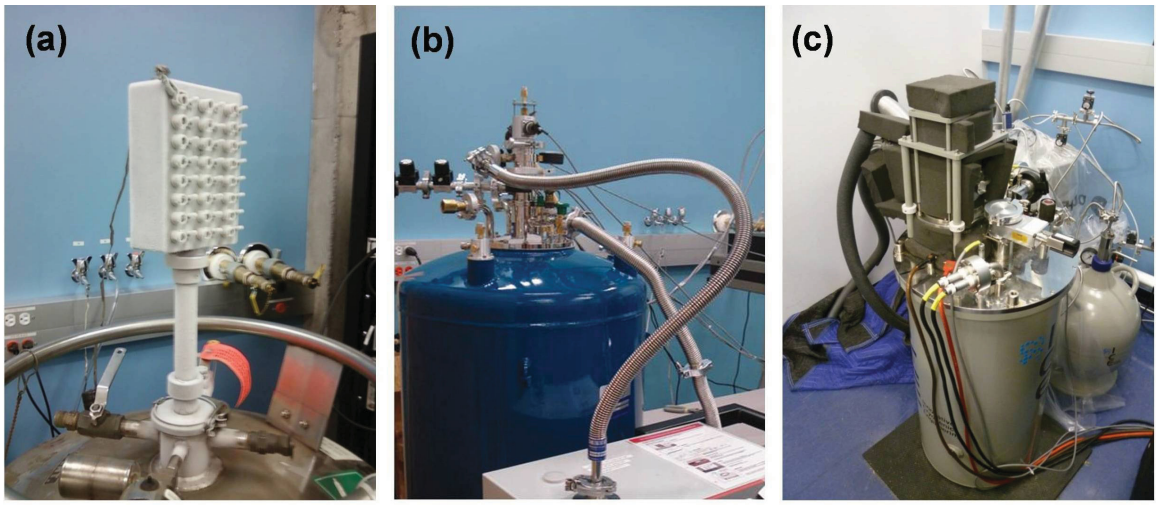

Figure 2.17: He-4 and He-3 Cryostats. (a) A liquid He dewar with a top-loading measurement stick. (b) Our He-4 cryostat provides a temperature range of $1.5-420$ K and magnetic field up to 14 Tesla. (c) Our He-3 cryostat provides a temperature range of $0.3-300$ K and magnetic field of up to 9 Tesla.

2.5 Circuits and electronic setup

The methods we use for data acquisition are firstly centered around protecting the sample, and secondly to reduce noise. We always keep the samples grounded when not being measured, use a personal ground at all times and minimize the number of ground loops in our system. To collect data we use a National Instruments Data Acquisition System (DAQ) with custom measurement software. The circuits we use for DC measurements are shown in Fig. 2.18. The lines from the sample to the Ithaco current pre-amp are wrapped in an additional coaxial cable for shielding and kept as short as possible to prevent noise pick-up. We optimize the sampling rates, sensitivity, and rise-time averaging on the Ithaco, and all pre-amps are zeroed before data acquisition to prevent offsets. Low pass filters are used on the Keithley voltage source to prevent spikes in gate voltage, and voltage dividers are used when applying bias voltage. Data is collected by the DAQ and stored on the controlling computer.

In this chapter we presented the fabrication procedures used to make suspended graphene/gold break-junctions. The samples are the wired-up and cooled down. At this stage they are ready for the final step of electromigration. In the next chapter we will discuss the fabrication of 10 nm scale graphene transistors. We will explain how we use a electromigrating technique to open a gap in the gold break-junction in order to expose graphene, and study electron transport in the quantum dot regime.

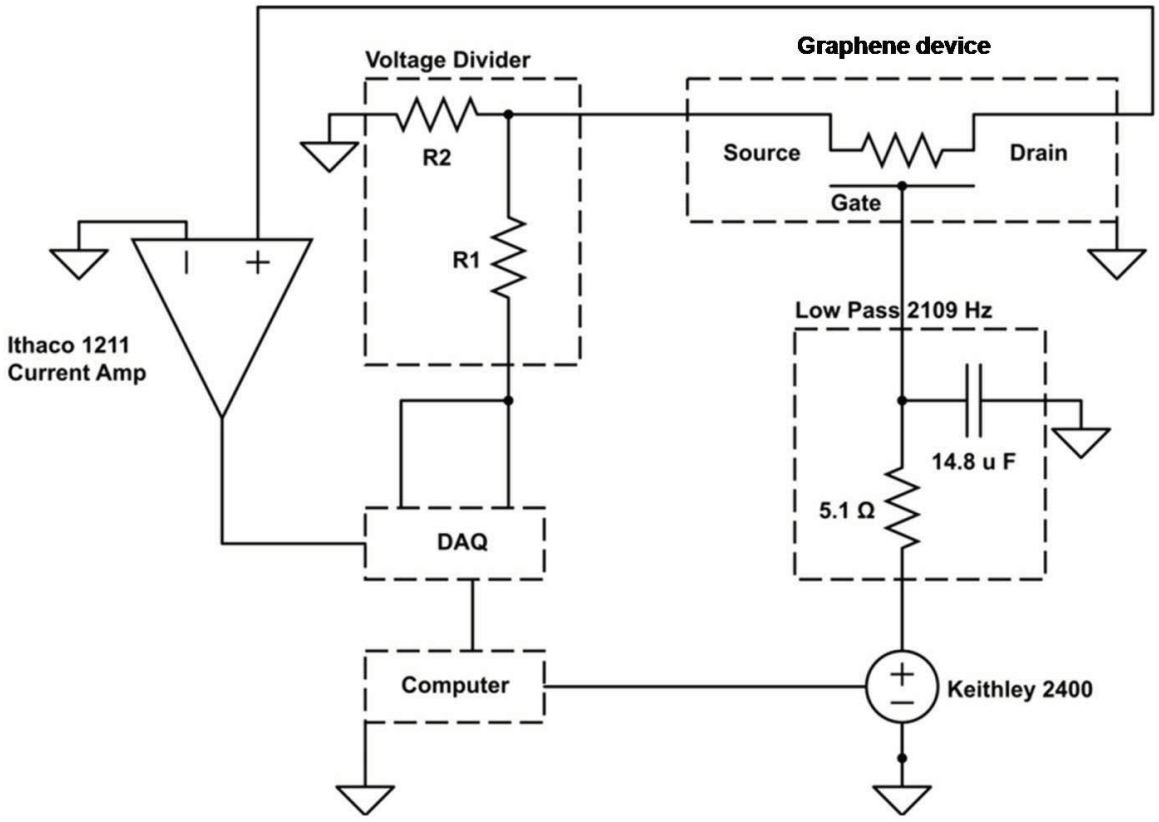

Figure 2.18: Circuits used for measurements. Electrical circuit for DC measurement, courtesy of Andrew McRae.

Chapter 3

Tailoring of graphene quantum dot transistors via electromigration

Since the discovery of graphene in 2004, much effort has been put towards making graphene quantum dot (QD) transistors because of graphene's potential for ultra-small nanoelectronics and quantum coherent computational applications [15, 16, 35, 36, 37, 38]. A QD transistor is made of a nanometer scale electronic island with discrete energy levels, which is isolated by tunneling barriers from metallic contacts. It can be extrinsically turned on (off) to allow (block) the flow of current through the device.

In principle, the fabrication of a graphene QDs is difficult due to the absence of a band gap in graphene's band structure, Fig. 1.3. It was shown that in a narrow ($\leq$100 nm) graphene constriction a band gap open up due to confinement [16]. *A. K. Geim et al.* [15] fabricated graphene QDs by cutting graphene into narrow constrictions using e-beam lithography followed by an O_2 plasma. Fifty nm scale QDs were later made by the same group and *J. Gttinger et al.*, using a similar approach. It was reported that graphene-based QDs larger than 100 nm behave like conventional QD transistors with a periodic conductance and constant charging energy (E_C) vs the number of electrons in the dot. Such that the amount of energy needed to add one electron to the QD is constant for each electron added to the QD due to the reflection from the rough and disorder edges of graphene [35]. For graphene QDs smaller than 100 nm, E_C becomes irregular and fluctuates with each electron added to the QD. In the recent years, excited electronic states, spin states and the Zeeman effect were

studied in graphene QDs [39, 40, 41].

Although 50 nm scale graphene QDs have been achieved, most of the reported QDs show a disordered transport behavior, irregular E_C and are coupled to substrate disorder. Here, we demonstrate 30 nm-size suspended graphene QD transistors (Fig. 3.1(a)). We have developed a nanoetching technique called feedback-controlled electromigration to make clean and small graphene quantum dots. We have previously used a similar technique to make carbon nanotube QDs (Fig. 3.1(b)).
In Chapter 2 we explained how to make suspended graphene break-junctions covered by gold. Here we will discuss the gold electromigration process, Where we break the suspended gold bowtie, and expose the graphene underneath to form a gold-graphene-gold junction (Fig. 3.1(a)). We can make graphene QDs in two ways using electromigration [1]: 1) By cutting and narrowing down the graphene channel using a large electrical field. 2) By introducing bulk defects (damaging) in graphene, using a lower electric field but a higher power. Thus, we can in principle, decouple and distinguish different sources of disorder. For example, removing substrate disorder by suspension, tuning the effect of edge disorder by making the dot wider, and creating bulk disorders by intentionally introducing defects via electromigration. One could then study the effect of each disorder on charge transport.

Our electron transport data in graphene QDs as a function of the Fermi energy [1] of the QD and the Au leads shows irregular charging energies as expected for graphene QDs smaller than 100 nm [35]. Since the dots are suspended, they can vibrate mechanically. We observed the signature of electrons coupling with quantized mechanical modes (vibron) in our transport data. Since our devices are very short they can have very high vibrational frequencies. We extracted frequencies up to ≈ 100 GHz, which are among the highest reported frequencies for nanoscale graphene resonator systems [7, 4]. We previously reported similar features of electron-vibron (e-v) coupling for the bending mode in single-wall carbon nanotube QDs [3]. The suspended graphene QDs we present here will in future projects serve as a platform for studying the effects of mechanical strain (which creates an effective magnetic field), on charge transport and *e-v* coupling.

The structure of this chapter is as follows. We first introduce the background to understand electron transport in QDs and recent literature results in graphene QD's.

[1] The Fermi energy is the highest occupied single particle energy level in the system.

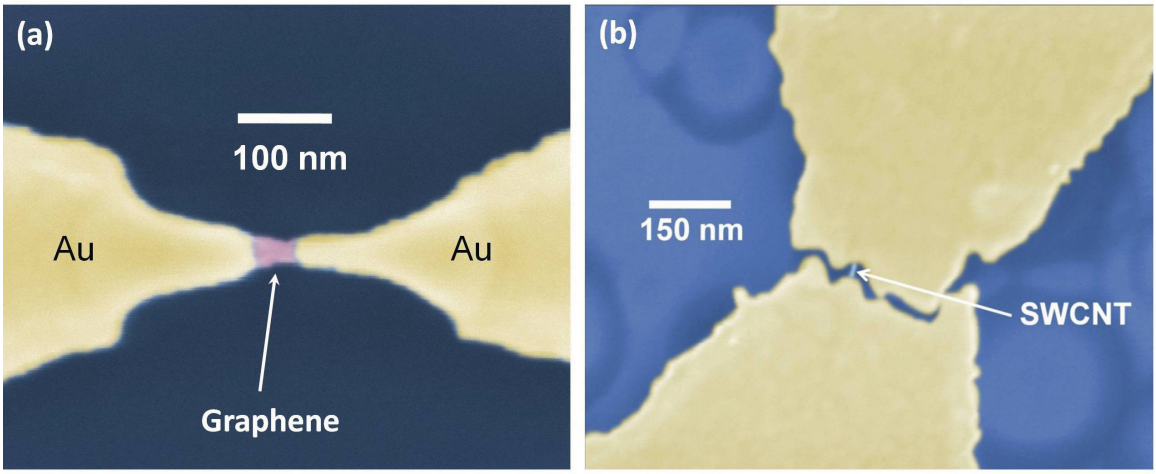

Figure 3.1: Electromigrated graphene and SWCNT QDs. (a) SEM image of a 24×44 nm suspended graphene quantum dot (false color). An ultra-short piece of graphene (pink color) is connected to gold contacts (yellow color). The gaphene and gold contacts are suspended over the SiO_2 (dark blue). (b) SEM image of a 20 nm long suspended single-wall carbon nanotube quantum dot (false color). The carbon nanotube, shown by an arrow, is connecting the gold contacts (yellow color). The nanotube and gold are suspended over SiO_2 (dark blue).

Then, we describe the electromigration and nanoetching techniques used to generate our suspended graphene devices. We explain how we make ≈ 30 nm graphene QDs, by cutting or introducing bulk defects in graphene, and discuss our charge transport data. Finally, we will discuss the signatures e-v coupling in our data. We show that the extracted vibrational frequencies are very close to the frequencies expected based on the geometry of the devices.

3.1 Electronic transport in QD transistors

In this section, we introduce the concepts of electron transport in a quantum dot.

Fig. 3.2 (a) shows a diagram of a QD field-effect transistor. The bottom gate is used to capacitively tune the number of electrons on the dot. Fig. 3.2(b) shows a representation of the electrical circuit of the device, indicating how the QD capacitively couples to the source, drain and gate with respective capacitances of C_S, C_D and C_G. The Γ_S and Γ_D are the tunneling rates between the QD and the source and drain electrodes, which allow electrons to tunnel across the dot. Fig. 3.2(c) is a top view

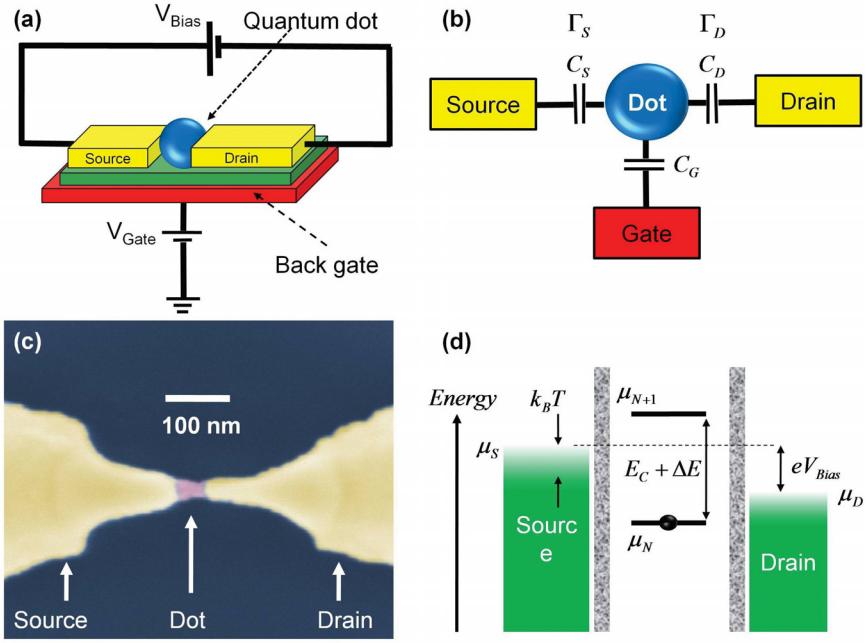

Figure 3.2: Schematic of a QD transistor. (a) QD field effect transistor. (b) A representation of the electrical circuit of the QD transistor. Γ_S and Γ_D are the tunneling rates through source and drain electrodes, respectively. C_S, C_D and C_G are source, drain and gate capacitances respectively. (c) Top view SEM (false color) image of one of our suspended graphene QD transistors. (d) An energy diagram showing the alignment of the electronic energy levels in the source, QD and drain. μ_N and μ_{N+1} are the levels for the N^{th} and $(N+1)^{th}$ electrons.

SEM (false color) image of one of our suspended graphene quantum dot transistors. The graphene QD (pink color) is connected to the source and drain gold electrodes (yellow color). The graphene QD, as well as the source and drain electrodes, are suspended above SiO_2 (dark blue) (see the tilted view in Fig. 2.1). Fig. 3.2(d) depicts the electronic energy state in the leads and QD. The energy spectrum in the leads is continuous and μ_S, μ_D are the Fermi levels in the source and drain respectively. Thermal fluctuations (k_BT) broadening the Fermi energy in the leads are represented by the blurry region. The bias energy, eV_B, is the energy difference between μ_S and μ_D. The energy spectrum of the dot is discrete, and μ_N and μ_{N+1} are the energy levels for the N^{th} and $(N+1)^{th}$ electrons. [42].

When there is no level available in the dot between μ_D and μ_S, there is no current flow as electrons cannot tunnel through the dot ($I = 0$, see Fig. 3.3(b)). This state is called Coulomb blockade, and is the "off" state of the quantum dot transistor. Alternatively, if an available level is between μ_D and μ_S, then current can flow ($I \neq 0$):

$$\begin{aligned} \mu_D < \mu_{N+1} < \mu_S \qquad & I \neq 0 \\ Otherwise \qquad & I = 0 \end{aligned}$$

When the dot is in its off state (see Fig. 3.3(a)) at low bias, increasing V_B increases μ_S until $\mu_S = \mu_{N+1}$ and current starts flowing (see Fig. 3.3(c)). For an even higher V_B multiple QD levels can be in the range of eV_B and enhance conductance.
As the gate voltage, V_G, is swept, the energy levels of the QD shift up or down. As soon as one level lines up between μ_S and μ_D (see Fig. 3.3(b)), the QD transistor switches to its "on" state and current can flow. By plotting I vs V_G, we can observe Coulomb blockade oscillations (see Fig. 3.3(d)). In the Coulomb valleys (blockade regions $I = 0$) the transistor is in its off state and the number of electrons in the dot is well defined.

To visualize the electronic energy spectrum of the QD, the transport data is usually displayed in 2D plots of I or dI/dV vs V_B and V_G (see Fig. 3.4). The Coulomb blockade regions appear as diamonds (charge number=constant), called Coulomb diamonds. The shape of the diamonds reveals specific information about the QD such as, its charging energy, gate, bias and drain capacitance. The gate capacitance,

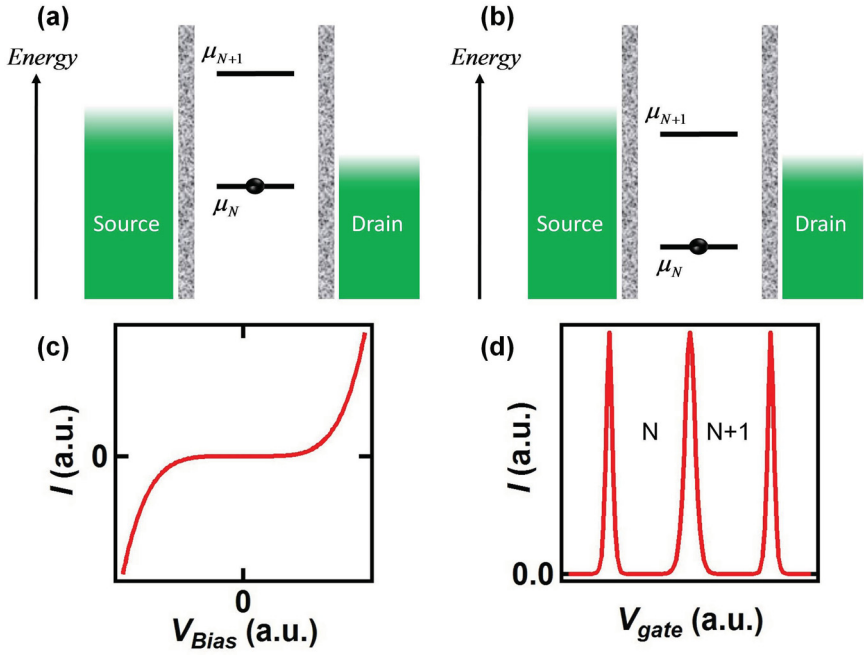

Figure 3.3: Schematic of Coulomb blockade. (a) Energy diagram of a QD transistor in the Coulomb blockade regime (off state). There is no available level for electrons to tunnel on the dot, since $\mu_{N+1} > \mu_S$, μ_D and $\mu_N < \mu_S$, μ_D. (b) Energy diagram of a QD transistor in the on state. There is an available level with $\mu_D < \mu_{N+1} < \mu_S$ for electrons to hop across the dot. (c) Cartoon of $I - V_B$ curve of the transistor showing the blockade at low V_B. As V_B increases, μ_S increases until it reaches μ_{N+1} of the dot and current can flow. (d) Indicates a $I - V_G$ curve of the transistor. Tuning V_G can cause the energy levels on the QD to shift up or down, and align the dot levels μ_S and μ_D. This results in periodic Coulomb peaks for I vs V_G. In the blockade regime the number of electrons on the dot, N and $N+1$, are well defined (ground state regions).

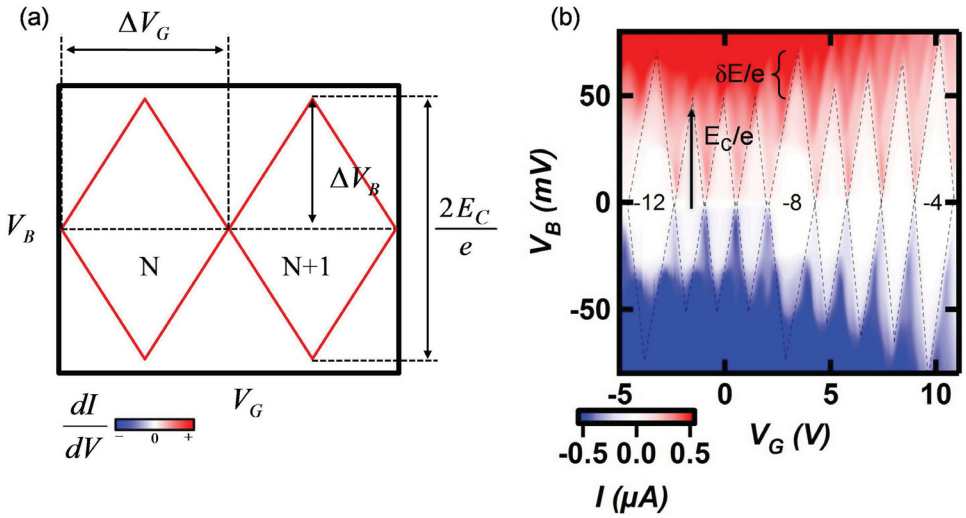

Figure 3.4: Contour plot of a QD transistor. (a) Cartoon of a contour plot of dI/dV vs V_B and V_G of a QD transistor with degenerate levels. ΔV_G and E_C charging energy are shown in the drawing. (b) Data for a SWCN QD transistor. E_C and δE (classical and quantum energy) are shown in the contour plot. Three diamonds have the same height, which is equal to E_C, with a forth one equal to $E_C + \delta E$ due to four-fold degeneracy. The number of electrons in the QD is shown in the plot. SWCNT QD data are courtesy of Andrew McRae.

C_G, can be extracted directly from the width of the diamond (see Fig. 3.4) as:

$$C_G = \frac{e}{\Delta V_G} \tag{3.1}$$

The charge addition energy, $\delta\mu_N$, is given by:

$$\Delta\mu_N = \mu_{N+1} - \mu_N = \delta E + E_C \tag{3.2}$$

where ΔE is the energy spacing between the quantum levels and $E_c = e^2/C_{total}$, is the charging energy: *i.e.* the classical energy necessary to charge the QD. For simplicity, we consider the energy levels of the dot to be spin degenerate and let $\Delta\mu_N = E_C$. E_C can be extracted from the height of the Coulomb diamond (see Fig. 3.4) as:

$$1/2 \; heigh \; of \; the \; diamond = \frac{E_C}{e} = \frac{e^2}{C_{total}} \quad C_{total} = C_S + C_D + C_G \tag{3.3}$$

The height and width of the diamonds are related by a prefactor α, which remains constant for all charge states as long as the QD capacitances remain constant:

$$\Delta V_G = \alpha\frac{E_C}{e} \qquad \alpha = \frac{C_S + C_D}{C_G} + 1 \tag{3.4}$$

An inequality between source and drain capacitances results in a difference between the positive and negative slopes of the Coulomb diamonds. The source and drain capacitances are given respectively by:

$$\Delta V_B = -\frac{C_G}{C_S}\Delta V_G \qquad \Delta V_B = \frac{C_G}{C_D + C_G}\Delta V_G \tag{3.5}$$

Information extracted from the blockade diamonds can be used to determine the physical size of the QDs.

3.1.1 Background on graphene QD transistors

As we discussed in section 1.2 (Fig. 1.3) and 1.2.1 (Fig. 1.4), an infinite graphene crystal has no band gap, and therefore the valence and conduction bands meet each other at the Dirac point (see Fig. 1.3). Additionally, the Klein tunneling effect allows charge carriers to tunnel through any potential barrier without backscattering

(at a normal incident angle, see Fig. 1.4). These characteristics makes it challenging to fabricate graphene QD transistors where electrons or holes have to be confined (localized) on the dot. Basically, a graphene transistor cannot be switched off, since there are always carriers which can Klein tunnel leading to a leakage current. These challenges can be overcome by creating an energy band gap in the graphene's band structure to confine (localize) electrons (holes) in the dot, which forms a graphene QD transistor with on and off states.

Several mechanisms have been suggested to open up an energy band gap in graphene's band structure, including chemical modification [43], hydrogen adsorption [44], special periodic substrates [45], and cutting it into narrow constrictions [16]. Thus far the majority of experiments use the method of cutting graphene into narrow constrictions [16, 35, 36]. Fig. 3.5(a) shows a cartoon of a narrow graphene transistor connected with source and drain contacts. It has been shown that the band gap in the graphene constriction is inversely proportional to its width, given by the following expression [16]:

$$E_g = \frac{2\pi\hbar v_F}{W} \tag{3.6}$$

where W is the width of the constriction, and $\hbar$ and $v_F \approx 10^6$ m/s are Planck's

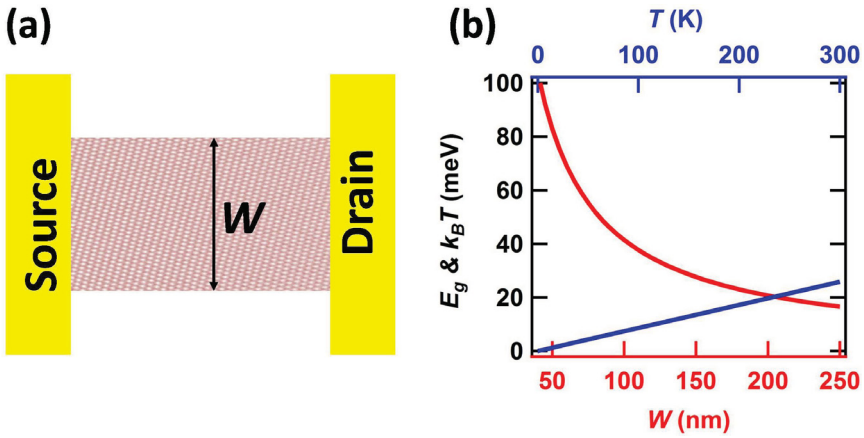

Figure 3.5: Width dependence of band gap in graphene. (a) Cartoon of a graphene nanoconstriction, width W, contacted with source and drain contacts. (b) Blue line represents the energy gap plotted as a function of W (bottom axis). Red line represents the k_BT (top axis), thermal fluctuations, as a function of temperature.

constant and the Fermi velocity in graphene, respectively. Fig. 3.5(b) shows the

energy gap as a function of the width (bottom axis) and k_BT as a function of T (top axis). It is important to note that confinement effects can be observed only when $E_g \geq k_BT$.

In the following section we will summarize some of the most recent literature results, discuss their limitations and describe how our work contributes to this body of literature.

3.1.2 Graphene QDs: recent results and their limitations

In this section we briefly discuss recent experimental work done in the field of graphene QDs. We describe what has been achieved with respect to graphene QD transistors, the limitations of these experiments and what our contributions will be to resolve some of these issues.

In the majority of data reported on graphene QDs by *A. K. Geim* and colleagues, and *K. Ensslin's* group (two leaders in the field) the band gap, E_G, was engineered by cutting the graphene using plasma etching [16, 35, 36, 37, 40]. Fig. 3.6(a) is a SEM image of one of their graphene QDs (bright blue). The dark blue lines are the etched lines. The graphene dot (central island) is connected to the source and drain electrodes (made of graphene as well). The side gates are used to tune the tunnel barriers (narrowest junctions made of graphene). Charge transport in this device is measured as a function of V_B, and the back and side gates (V_G). This technique has since been used by several other groups to fabricate graphene quantum dots.

In Fig. 3.6(b) the transport data as a function of V_B and V_G is shown, for the quantum dot shown in Fig. 3.6(a). Coulomb diamonds are visible in the 2D plot, indicating the Coulomb blockaded charge states. Using this technique, QDs ranging in size from a few hundreds down to 40 nm have been fabricated and studied [16, 35]. *A. K. Geim* and colleagues have shown that for graphene QDs larger than $\sim$ 250 nm in diameter, the Coulomb diamonds are periodic. However, for diameters smaller than 100 nm, the Coulomb diamonds become highly non-periodic. This non-periodic behavior can be explained by the fact that any confinement for Dirac fermions leads to quantum chaos, due to the chaotic trajectory of the Dirac fermions reflected by the rough edges of the QD [35].

Thus far, 40 nm scale graphene QD transistors on substrate have been achieved [35]. However commonly used techniques (such as plasma etching) which are used

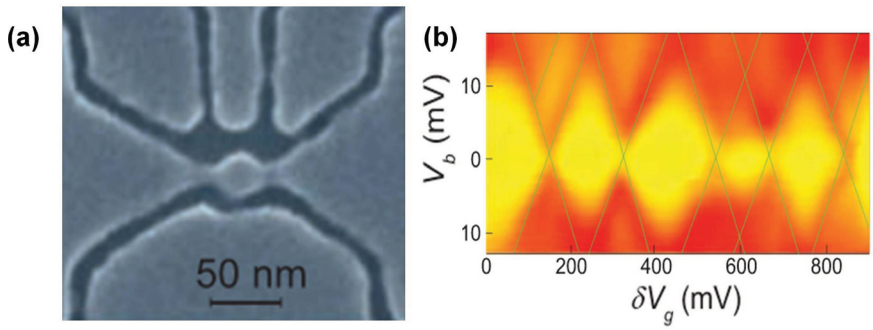

Figure 3.6: Formation of a graphene QD using plasma etching. (a) is an SEM image of a graphene QD (bright blue) made by plasma etching of graphene. The dark blue lines are the etched lines. The graphene dot (central island) is connected to the source and drain electrodes, also made of graphene. (b) Conductance of a 40 nm graphene QD as a function of V_B and V_G at $T = 4$ K. Reproduced from reference [35].

to make graphene quantum dots result in disordered edges. Additionally, most of the reported graphene quantum dots are fabricated on substrate and are therefore coupled to substrate disorder. Due to the complexity of fabrication it is very difficult to suspend such QDs.

We can make QDs as small or smaller than the leading groups, $\approx 30-40$ nm, and are also able to suspended them and tailor their shape. We are able to distinguish different sources of disorder which can affect the QD, such as substrate and bulk disorder. Since our devices are suspended, they can be used as ultra-high frequency graphene resonators and graphene based nanoelectromechanical systems (NEMS). These will be used as a platform by our group, in the future, to study the effect of mechanical strain on quantum transport and electron-vibron coupling in graphene.

In the next section we will describe the methods we have developed to fabricate our suspended graphene quantum dots.

3.2 Electromigration: making gold-graphene-gold nanogap

In chapter 2 we explained how we fabricate suspended gold-covered graphene bowtie junctions. Here, we discuss how to open up a gap in the gold to expose a $\approx 10-100$ nm long graphene channel.

Using standard micro- and nano-fabrication techniques, it is currently impossible to make 10 nm suspended channels with good metal contacts. At this scale, lift-off of the deposited metal becomes extremely difficult (see section 2.1.4). Therefore, we use different, innovative techniques which make it possible to construct much smaller devices.

We use a nanoetching technique based on electromigration to make 10 nm scale

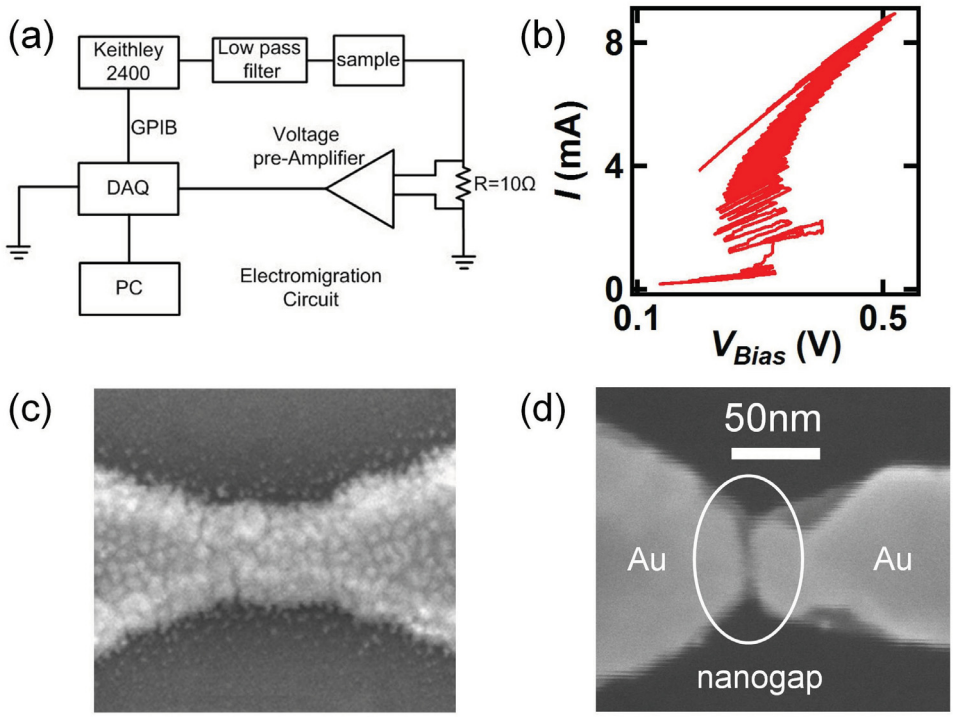

Figure 3.7: Electromigration and making nanogaps. (a) Feedback controlled electromigration circuit . (b) $I - V_B$ curve of feedback-controlled electromigration circuit showing sequential nanoetching of the junction, where each zig-zag of the $I - V_B$ trace corresponds to one nanoetching step. (c) SEM of a break-junction before electromigration. (d) SEM image of a break-junction after electromigration. It can be seen that the gold break-junction was electromigrated and a 5 nm-long graphene channel is exposed.

gold-graphene-gold nanogap. Electromigration has been previously used in the fabrication of QD transistors made of different materials such as gold nanoparticles, C_{60}, carbon nanotubes and single organic complexes [2, 3, 28, 46, 47, 48, 49].

In standard electromigration, a bias voltage is ramped up so that the gold break-junction heats up due to Joule heating, resulting in increased mobility of the gold

atoms. This increased mobility, combined with momentum transfer from the electrons, knocks the gold particles out of the beak-junction. Typically, a sudden break will happen and a gap will open in the break-junction [28, 49].

The geometry and size of the electromigrated gap depends on several variables, such as temperature, total series resistance, thickness of the gold film and suspension of the break-junction. As etching takes place, resistance (R) increases so that Joule heating increases, therefore electromigration speeds up. This is an avalanche process which leads to an uncontrolled break, giving rise to a large gap and damage in the graphene channel [49, 50, 51]. We adapted this feedback electromigration method to suspend graphene break-junctions at high vacuum and low temperature, to better control the electromigration process. Fig. 3.7(a) shows our electromigration circuit. We use a Keithley 2400 as a DC voltage source in series with a low pass filter. The current flowing through the junction is monitored via the voltage across a 10 Ω series resistor, using voltage pre-Amp and DAQ connected to a computer. We increase the voltage gradually, with an adjusted rate, while the real time resistance of the junction is monitored by the feedback system. As soon as the resistance of the junction changes by a pre-defined amount, the feedback system lowers the voltage by a given percentage allowing the junction to cool down (the breaking process will not start until the local temperature of the gold reaches $\sim 400K$ [52]). We repeat this step multiple times, until the resistance of the sample reaches a target resistance (R_{max}). This allows us to either partially or completely break (or etch) the junction. Fig. 3.7(b) shows an $I-V$ curve of sequential breaking steps using the feedback control process. Fig. 3.7(c) and (d) show SEM images of a break-junction before and after electromigration. We can see that the gold break-junction has been electromigratated and a 5 nm-long graphene channel is exposed (see Fig. 3.7(d)).

How to control the size and shape of the junction? We are interested in making ultra-short junctions with a rectangular geometry and smooth edges. We aim to optimize the feedback control process to meet these goals. Fig. 3.8 shows the electromigration procedure for different junctions and the SEM images of these junctions afterwards. Fig. 3.8(a) and (b) show a high power electromigration and the resulting junction. Breaking the junction at a high power results in asymmetric and pointy contacts. Moreover, it will likely damage the graphene crystal as we will discuss in section 3.3. Fig. 3.8(c) and (d) show the electromigration of a wide junction ($W \approx 400$

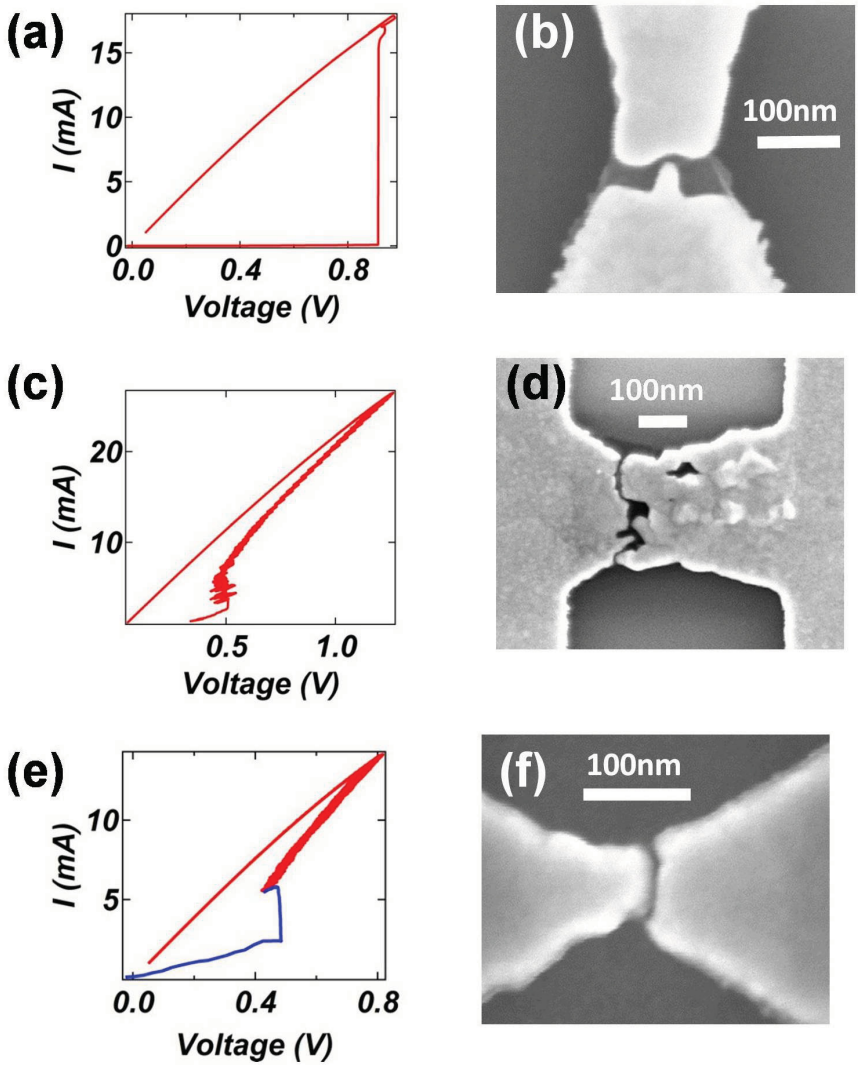

Figure 3.8: Optimizing the feedback controlled electromigration. (a) $I-V$ trace of the feedback controlled electromigration process showing a high power breaking. (b) SEM image of the break-junction after the electromigration in (a). (c) $I-V$ curve of the feedback controlled the electromigration of a wide junction. (d) SEM image of the break-junction after electromigration in (c). (e) $I-V$ curve of the feedback-controlled electromigration at low power. (f) SEM image of the break-junction after the electromigration in (e).

nm). Electromigration of wide junctions leads to channels with very rough edges. This is likely due to the formation of a temperature gradient surrounding impurities (hot spots) resulting in different electromigration rates across the break-junction. Fig. 3.8(e) and (f) show a very low power electromigration. Electromigrations at very low powers form atomic-scale gaps, where the edges of the gold contacts are not sharp. Such atomic-scale junctions cannot be described with the theoretical models for graphene transport, since their structure is unknown. We conclude that the electromigration of ≈ 100 nm wide suspended beak-junctions at low temperatures, with powers ranging from $3 - 20$ mW, results in $\approx 5 - 40$ nm long graphene channels. Fig. 3.9 shows the lengths of the electromigrated gaps versus their electromigration breaking powers, which indicates that increasing the breaking power results in a longer channel.

To control the breaking power in the electromigration process, we developed a two-step process called *fixed power breaking*. Fig. 3.8 (e) shows a trace for the *fixed power breaking* method. We partially electromigrate a break-junction to a predefined power, and terminate the process by ramping down the voltage to zero when it reaches this desired power (see Fig. 3.8 (e) red curve). This narrowed the junction for the second step. Then, the voltage is ramped up across the narrowed (partially etched) junction while the feedback loop is disabled. At the predetermined power, the avalanche electromigration process takes over and opens a 10 nm size gap in the junction. This technique can be used to define the breaking power. Using the *fixed power breaking* method we can engineer the length and geometry of the junction.

In sections 3.3 and 3.4 we will explain how to use this *fixed power breaking* method to fabricate graphene QDs. In Chapter 4, we will elaborate on how to use it to make ballistic graphene devices.

3.3 Fabrication of graphene QDs via defect engineering

In this section we describe a method to fabricate graphene QDs by introducing defects in the graphene channel during electromigration.

We use the feedback control system while electromigrating the junction continuously, to a small power of less than a few mW, and a voltage of a few hundreds of

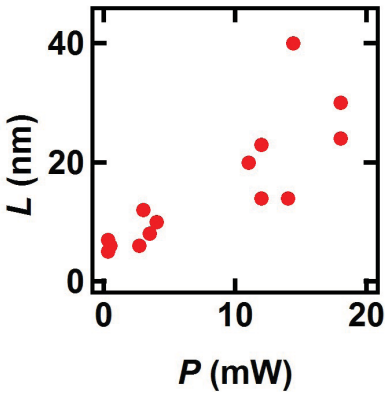

Figure 3.9: Length of the electromigrated gaps versus their electromigration breaking power.

mV (e.g. see Fig. 3.7). This forms a very short channel (sub-10nm, see Fig. 3.7(d)), a smooth and relatively wide junction (about $W \approx 100$ nm) which creates a very transparent (high conductance) channel for the electrons. This transparent channel is useful for studying ballistic charge transport in graphene, which will be discussed further in chapter 4. However, such devices are too conductive to study QD transport.

Starting with such short and wide devices with a high conductance, we can gradually damage the graphene channel (add a defect) to increase the resistance of the device and transform the device to a QD. To add controllable defects, we continue the electromigration even after the graphene channel is completed. These additional "current heating" steps can be used both to anneal graphene (remove fabrication residues) or, if pushed to a higher power, introduce defects in the flake in a controlled manner. Fig. 3.10 (c) and (e) show an $I - V_B$ curve of current annealing which locally heats the flake up to a few hundred degrees [18] and evaporates the EBL residues and absorbed water. To do so, typically V_B is ramped up to a specific voltage and power, and kept constant for a few minutes. The resistance of the sample is monitored and V_B is lowered manually.

Because the junctions are very short, the transport within it is ballistic, and not much power dissipates in the graphene channel. Therefore, it is possible to apply a very high electric field (V_B/L) across the junction. We repeat the voltage ramp-up multiple times, each time slightly increasing the final V_B and consequently the electric

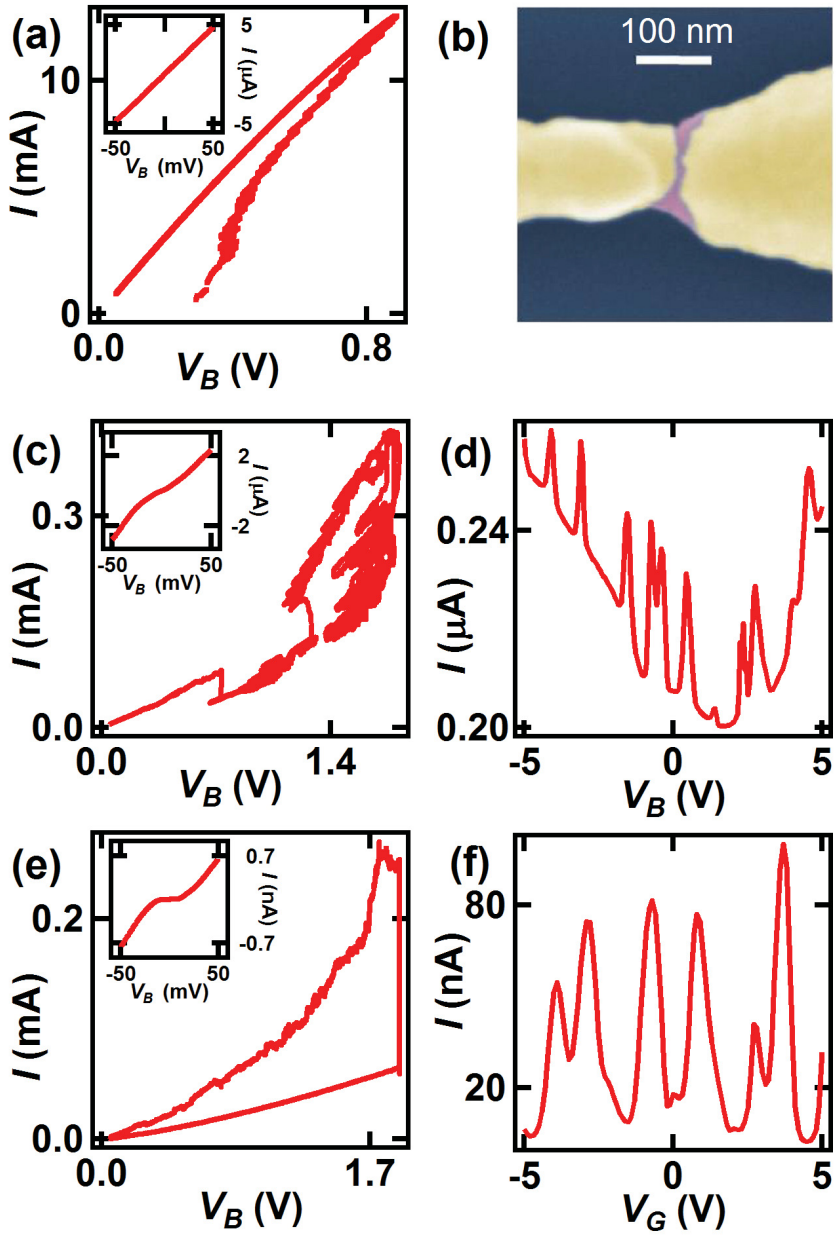

Figure 3.10: Fabrication of a graphene QD by introducing defects in the graphene channel. (a) Electromigration curve of the gold bridge using the feedback-controlled process. Inset in (a) shows the $I - V_B$ curve after gold electromigration. (b) SEM top view image of the device in (a), scale bar is 100 nm. (c) Defect creation in graphene completed after electromigration in (a). Inset in (c) shows the $I - V_B$ curve after the defect creation. (d) Gate sweep of the device $I - V_G$ following step (c). (e) The second step in the creation of defects, to create a stronger charge confinement. Inset in (e) shows the $I - V_B$ curve after step (e). (f) Shows the sweep $I - V_G$ after step (e), where clear Coulomb Blockade oscillations are visible.

field. A very high electric field is known to tear graphene [53, 54]. Using sequential annealing steps, we observe a transition from 2D to 0D and electron transport regime, which signals the formation of a QD. Fig. 3.10 shows the electromigration step, subsequent annealing steps and how the transport changes from 2D to 0D (see the inset of Fig. 3.10 (c) and (e)). Fig. 3.10 (a) shows the electromigration curve using the feedback control mechanism. The final break occurs at a very small power and voltage ($P \approx 0.3$ mW, $V \approx 0.3$ V and $I \approx 1$ mA). Inset in Fig. 3.10 (a) shows a linear $I - V_B$ curve taken immediately following electromigration. The $I - V_B$ curve indicates that the graphene is not damaged and acts as a 2-dimensional electron gas. Fig. 3.10 (c) shows the first defect creation step. The device in Fig. 3.10 was not suspended and was thermally anchored to the substrate. The main cause of defect formation was therefore the strong electric field. Different jumps in Fig. 3.10 (c) show that R suddenly changes due to the introduction of defects. The inset in Fig. 3.10 (c) shows the $I - V_B$ curve of the sample following the step in (c), and indicates a significant change in $I - V_B$. The bias sweep is no longer straight and shows a weak Coulomb blockade at low V_B (resistance of the sample at 1 mV is about 46 kΩ). Fig. 3.10 (d) shows the $I - V_G$ curve following the step in (c). Interestingly, it shows both 2D transport (parabolic shape) on top of 0D (Coulomb oscillations). Fig. 3.10 (e) is the final defect creation step. V_B is ramped up to about 1.8 V where a sudden break occurs. The inset of Fig. 3.10 (e) shows a clear Coulomb blockade in the $I - V_B$ curve (resistance of the sample is about 10 MΩ at 1 mV). Fig. 3.10 (f) shows the $I - V_G$ curve following the step in (e), indicating that 2D transport has disappeared and a clear Coulomb blockade is visible. When comparing Fig. 3.10 (d) and (f), one notices that the peak spacing (width of the Coulomb diamonds) becomes larger in (f). This indicates that the QD becomes smaller (smaller C_G).
Although the junction experienced a high V_B, the shape of the gold contact remained symmetric. This is consistent with the fact that the transistor is sitting on the substrate and thus does not reach $T > 400$ K.

Here, we described the method used to fabricate QDs by creating defects in the graphene channel, using feedback controlled electromigration. In the next section we will discuss how we fabricate a QD by cutting graphene into narrower channels.

3.4 Fabricating QDs by "cutting" graphene

In this section we describe how to make a graphene quantum dot by tearing the flake along the length of the channel using high electric fields.

If the electromigration step which creates the channel (first step) takes place at a high power and within a high electric field, it forms asymmetric and pointy contacts (see Fig. 3.11). We observed that this process not only breaks and narrows down the gold contacts, but at the same time tears the graphene channel into narrow constrictions. It has been predicted that tearing graphene with an electric field can create ordered edges [53, 54]. Thus, we expect to have much less edge disorder in samples fabricated using this method. This would mean that the final area of the channel corresponds to a single QD, rather than multiple dots of uncontrolled sizes.

By using the *fixed power breaking* method (explained in section 3.2) we are able to break the junction at a predetermined power. Fig. 3.11(a)-(b) show the *fixed power break* and an SEM image of a junction broken at high power ($P \approx 15$ mW, $I \approx$11.7 mA and $V_B \approx 1.1$ V). The length and width of the produced channel are about 23 nm and 32 nm respectively. Fig. 3.11(c)-(d) show a device electromigrated at a high power ($P \approx 20$ mW, $I \approx 14.8$ mA and voltage $V_B \approx 1.36$ V). The length and width of the channel are about 29 nm and 67 nm respectively. By comparing the geometry of the two devices from their SEM images, we can see that the device in (d) is more asymmetric (higher power) than the one in (b). The device in Fig. 3.11(e)-(f) was not broken in a single step as the samples in (a) and (c), but rather with a series of small breaks as can be seen in (e). Eventually, the final break takes place at high power ($P \approx 15.6$ mW $I \approx$12.7 mA and $V_B \approx 1.23$ V). After the break at high power, we current annealed the sample (shown in (e)-(f)) in multiple steps up to 1.7 V. The inset of Fig. 3.11(e) shows the final annealing step. The sample is suspended, and annealing at a high power (after the final gold break) heats up the gold junction (Joule heating) which allows its contacts to anneal into a more symmetric shape.

As we increase the gold breaking power, the length of the channel becomes longer (see Figs. 3.9 and 3.11) and the contacts become pointier and more asymmetric. This method can be used to fabricate narrower constrictions. By comparing the devices shown in Fig. 3.11(b) and with (f), we can see that they were both created with a similar power ((b) at $P \approx 13$ and (f) at $P \approx 15.6$ mW) but the device shown in (f) has more symmetric contacts than the device shown in (b). This demonstrates

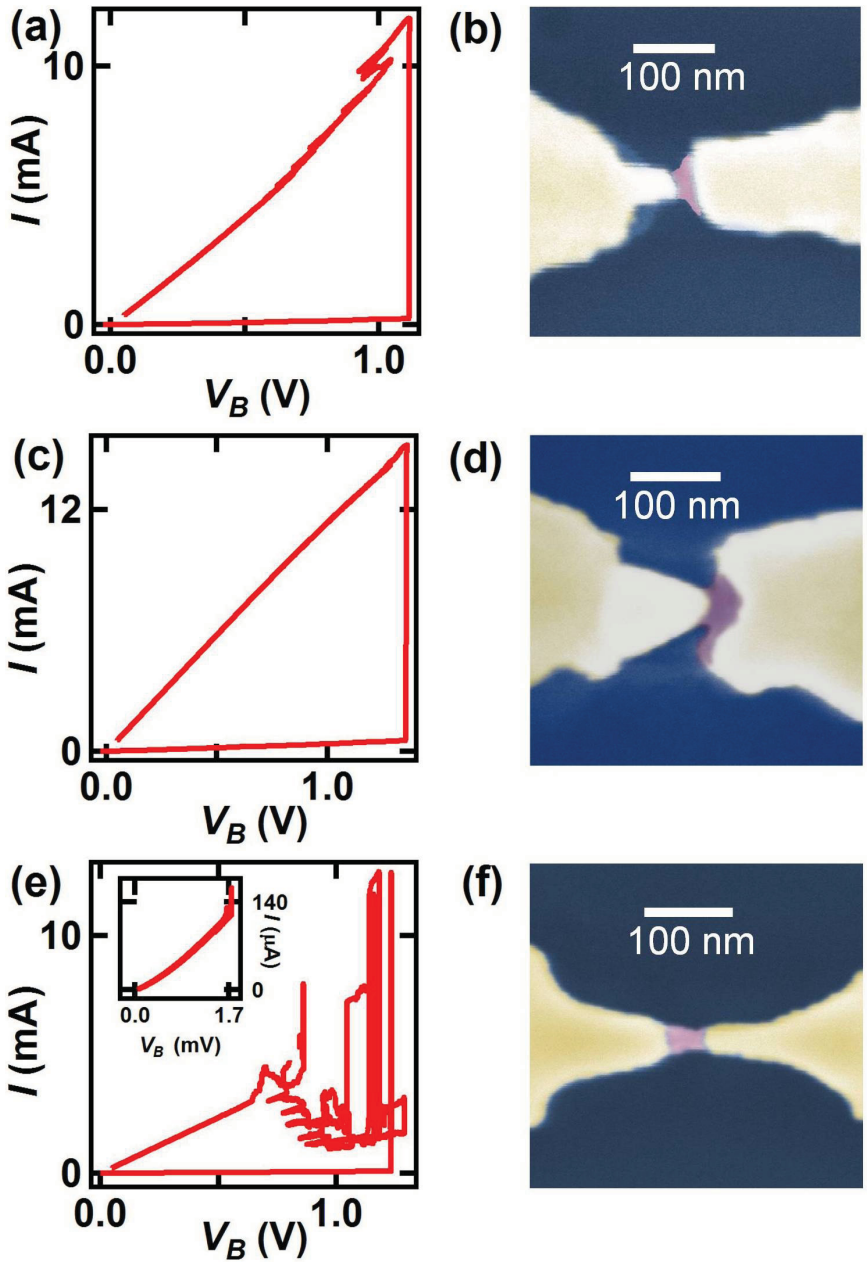

Figure 3.11: Fabricating QDs by cutting graphene. (a) $I - V_B$ curve of the gold electromigration for the sample (b). The final break takes place at high power ($P \approx 13$ mW, I$\approx$ 12 mA and $V_B \approx 1.1$ V. (b) Top view SEM image of the sample in (a). (c) $I - V_B$ curve of the electromigration for sample (d). The final break takes place at high power ($P \approx 20$ mW, $I \approx 14.8$ mA and $V_B \approx 1.36$ V. (d) Top view SEM image of the sample in (c). (e) $I-V_B$ curve of the electromigration. The final break takes place at high power ($P \approx 15.6$ mW, $I \approx 12.7$ mA , $V_B \approx 1.23$ V). Inset of (e) shows the final current annealing step. The sample was annealed up to $V \approx 1.74$ V, $I \approx 160\mu$A. (f) SEM image of the sample in (e) after annealing .

how important the annealing step is (after the final break) to make the contacts symmetric.

Here, we explained how to make a QD by cutting graphene at high power. The electron transport data of the devices in sections 3.3 and 3.4 will be presented in the following section.

3.5 Electron transport data in QDs

In this section we analyze the transport data taken in the suspended graphene QDs presented in the previous section (Figs. 3.10 and 3.11). We use standard single electron transistor spectroscopy (section 3.1) to extract the charging energy and gate capacitance of the dots. We will show that the area of the QD extracted from the transport is in close agreement with the area measured in the SEM images, confirming that we can engineer the shape and size of our QDs.

Fig. 3.12(a) shows a 2D contour plot of $\frac{dI}{dV_B}$ vs V_B and V_G for the device shown in Fig. 3.10. Fig. 3.12(b) shows the 1D cut (along the dashed dark line in (a)) for I vs V_G at $V_B \approx 3$ mV for the same device, showing Coulomb oscillations. In most of our devices we study a small V_G range so as to avoid collapse of the suspended device due to large electrostatic forces.

Fig. 3.12(c) is a 1D $I - V_B$ sweep (along the dashed red line in (a)). It shows the Coulomb blockade around $V_B \approx 0$. The average charging energy, E_C, over the V_G range is 8.8 ± 1.5 meV. The average gate capacitance, C_G, extracted from the width of the diamonds is $1.7 \pm 0.3 \times 10^{-19}$ F. Using the parallel plate capacitor approximation, we calculate the area of the graphene QD to be 1848 ± 343 nm^2. The area extracted from the top view SEM image is 2380 ± 210 nm^2 (see Fig. 3.10). Thus, this is in agreement with the area extracted from the transport data. This area is equivalent to a square of $\approx 48 \times 48$ nm. As expected for graphene QDs with diameters less than 100 nm, we see non-periodic Coulomb diamonds. This means that the charging energy is not the same for each electron/hole added to the QD. This variable E_C is due to edge disorder, an effect which is enhanced in smaller QDs. The edge disorder creates various angles of reflection. These angles depend on the energy of the electrons, and affect transmission and charging energy of the QD.

Fig. 3.13 (a) also shows a 2D contour plot of $\frac{dI}{dV}$ vs V_B and V_G for the device shown

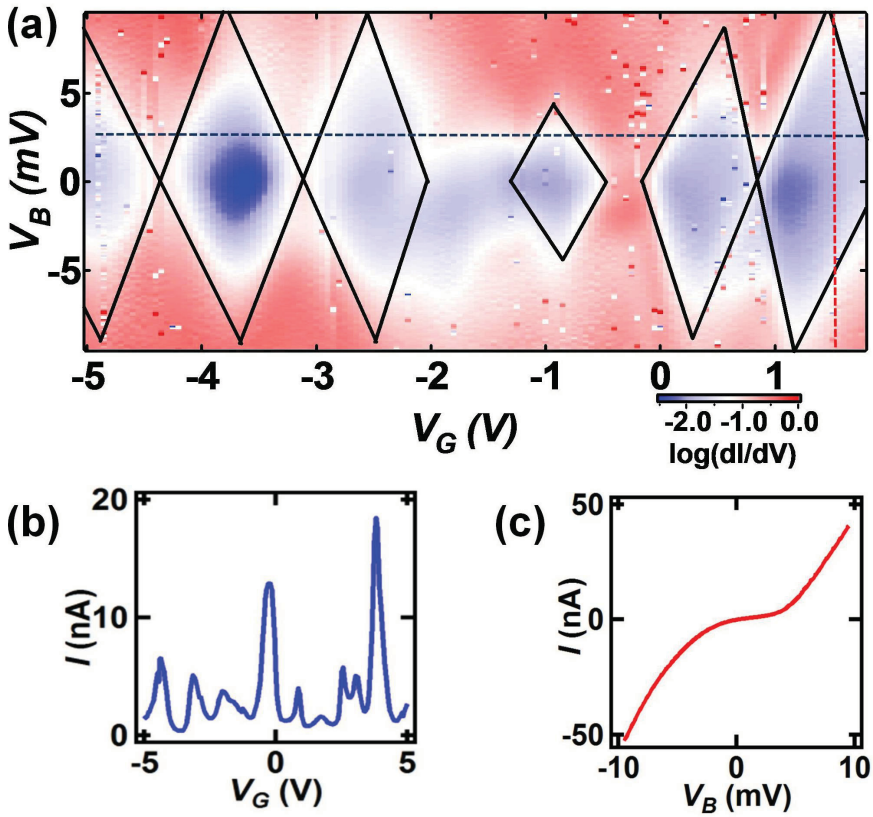

Figure 3.12: Transport data from the graphene QD device shown in Fig. 3.10. (a) 2D plot of $\frac{dI}{dV_B} - V_B - V_G$. (b) 1D $I - V_G$ along the dark dashed line in (c). (c) 1D cut $I - V_B$ along the red dashed line in (c).

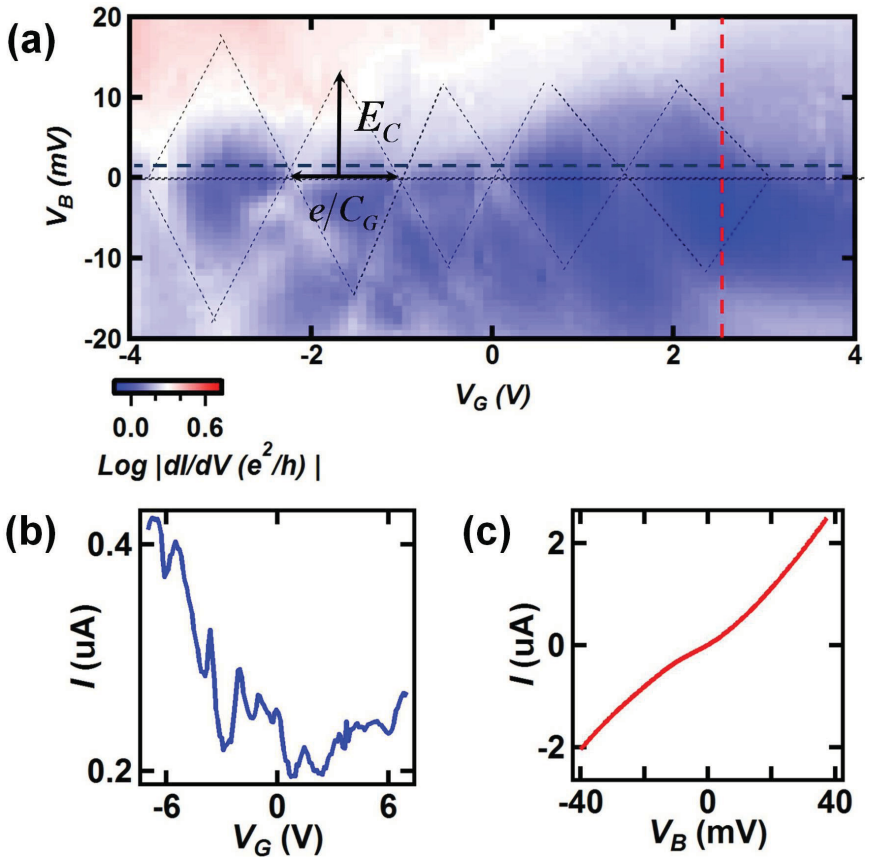

Figure 3.13: Electron transport data for the suspended graphene QD shown in Fig. 3.11 (a)-(b). (a) $\frac{dI}{dV_B} - V_B - V_G$ for the suspended graphene QD shown in Fig. 3.11 (a)-(b). (b) $I - V_G$ along the blue dashed line in (a). (c) $I - V_B$ along the red dashed line in (a).

in 3.11 (b). Fig. 3.13 (b) and (c) show the 1D cuts along V_G and V_B respectively. The average E_C and C_G for this device are 12 ± 1.5 meV and $1.1 \pm 0.15 \times 10^{-19}$ F respectively. The area extracted from C_G is 1395 ± 242 nm^2 which is very close to the calculated SEM area of 1220 ± 170 nm^2, (see Fig. 3.11).

Fig. 3.14(a) also shows a 2D contour plot of $\frac{dI}{dV_B}$ vs V_B and V_G for the device

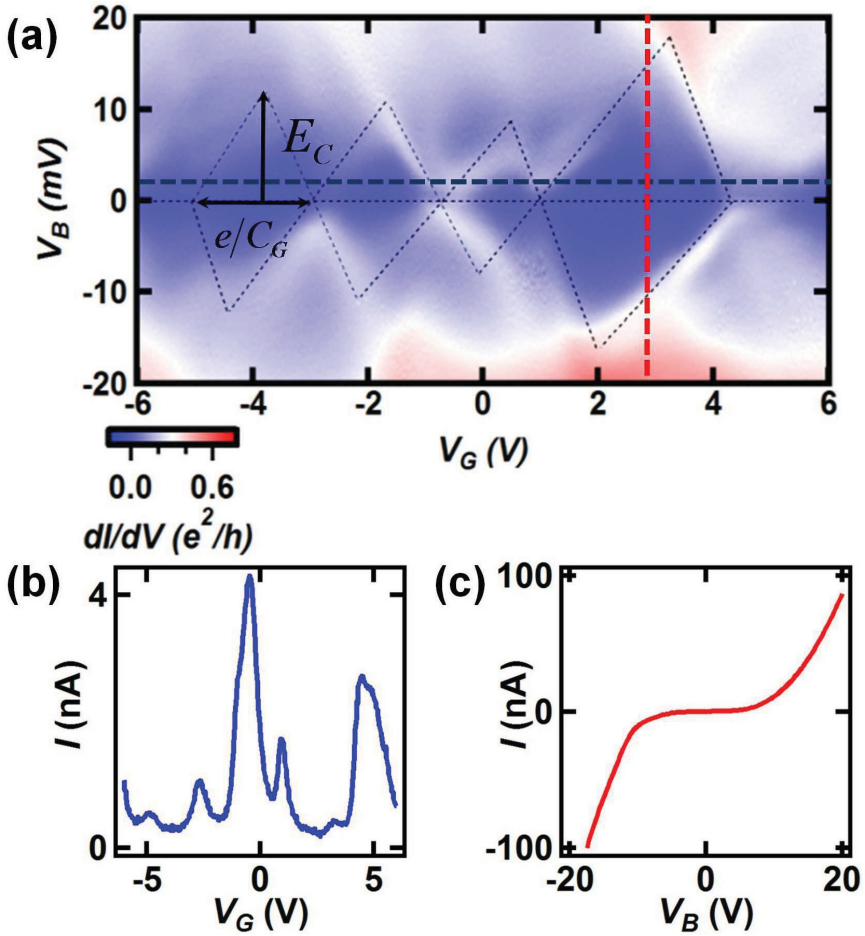

Figure 3.14: Electron transport data for the suspended graphene QD shown in Fig. 3.11 (e)-(f). (a) $\frac{dI}{dV_B} - V_B - V_G$ data for the suspended graphene QD shown in Fig. 3.11 (e)-(f). (b) $I - V_G$ along the blue dashed line in (a). (c) $I - V_B$ along the red dashed line in (a)

shown in Fig. 3.11(f). The average E_C and C_G for this device are 8.5 ± 2.6 meV and $8.8 \pm 1.9 \times 10^{-20}$ F respectively. The area extracted from the C_G is 990 ± 215 nm^2, which is in agreement with the SEM area, 1062 ± 190 nm^2, $\approx 24 \times 44$ nm (see Fig. 3.11 (f)).

In summary, we have fabricated suspended graphene QDs as well as $\approx 20-30$ nm (devices shown in Fig. 3.11(b) and (f)) which are the smallest graphene QDs produced to our knowledge, and the first such small QDs to be suspended. All three of our QD devices show clear Coulomb blockade at low V_B. Non-periodic charging energies is observed in all of the QDs, as expected for graphene QDs smaller than 100 nm [35]. The area of each of the QDs, extracted from the transport data, is in agreement with the corresponding area extracted from the SEM images. This confirms that we are able to engineer the size and shape of our suspended graphene QDs, and there is a very little "bulk" disorder in the dots (we removed bulk disorder due to substrate). The data suggests that the electric field during electromigration can cut graphene with relatively low edges disorder [54].

In this section we explained how to electromigrate gold/graphene to create ultra-short suspended graphene QDs. In some of these suspended dots we observed signatures of electron-vibron coupling, and vibrational frequencies up to the 100 GHz range. In the next section we discuss these data.

3.6 Graphene NEMS and the detection of the flexural vibrational mode

The very large stiffness (Young's modulus of ≈ 1.0 TPa) of graphene makes it an ideal membrane for nanometer scale resonators and NEMS. There has been much effort in fabricating micron scale graphene resonators. So far, megahertz range graphene resonators have been achieved [4, 7]. Graphene NEMS have a vast range of applications such as sensing (mass/force) and information processing (quantum computing). In this section we present the electron transport data for nanometer-scale graphene resonators. This initial data suggests resonance frequencies of up to 100 GHz.

In suspended QDs with high Q-factors (Quality-factor[2]) coupling between electrons and out-of-plane vibrons (bending modes) can give rise to a positive feedback between the tunneling electrons hopping on/off the QD and the mechanical vibrations of the dot. This can lead to self-actuation of the vibrations when the tunneling rate

[2]The Quality factor is a parameter proportional to how many oscillation cycles a resonator can do before it loses its energy. A high Q-factor means that the energy in the oscillator is not dissipated rapidly.

of the electrons matches the resonant frequency of the oscillator [3, 55]. When the oscillator is driven on resonance by the current flow, the large amplitude vibrations show a distinct dI/dV signature. This resonance can lead to current flow inside the normally blockaded Coulomb valleys. The frequency of the oscillator can be extracted from the amplitude of this current, deep within the normally blockaded region as:

$$f \approx \frac{I}{e} \approx \Gamma \tag{3.7}$$

Where f is the frequency of flexural vibronic mode, I is the current, e is the electron charge and Γ is the tunneling rate of the electrons.

We have previously seen this signature in very short suspended single-wall carbon nanotube (SWCNT) QDs. We measured NEMS frequencies in these SWCNT-QDs up to 280 GHz [3]. We also observe these signatures in our suspended graphene QD transistors, and find that the frequencies extracted from transport data are close to the vibronic frequencies expected based on the length of the devices measured by SEM [4]:

$$f = ([A(\frac{E}{\rho})^{1/2}\frac{t}{L^2}]^2 + A^2 0.57\frac{T}{\rho L^2 wt})^{1/2} \tag{3.8}$$

where f is the frequency of the graphene resonator, $E = 1.0$ TPa is the Young's modulus of graphene, $\rho = 220$ kg/m^3 is the mass density, $t = 0.335$ nm, w and L are the thickness, width and length of graphene respectively, A is the clamping coefficient which is 1.03 for a doubly clamped beam, and T is the tension applied to the flake.

Figure 3.15(a)-(b) are contour plots of the $dI/dV_B - V_B - V_G$ data showing the strong dI/dV signature, which signals the onset of the vibrations in device Q1 (shown in Fig. 3.11(b)). Fig. 3.15(c) is I (blue) and dI/dV (red) vs V_B showing the dI/dV peaks (circled). Figure 3.15 (d) expands the $I - V_B$ data around the resonance in (a) and shows a clear step in I. ΔI is the difference between the current after and before the dI/dV peak. We use this ΔI in (d) to extract the vibrational frequencies for positive and negative V_B.

We note that ΔI is either equal to or smaller than $e \times f$, because the vibrons and I may be out of phase. The extracted frequencies for the device shown in Fig. 3.15 cover a frequency range from ≈50 GHz to ≈100 GHz which correspond to theoretical frequencies with 1 to 2% strain while $w \approx 50$ nm and $L \approx 25$ nm. The strain here is a static strain resulting from bending of the gold bridge due to the suspension process.

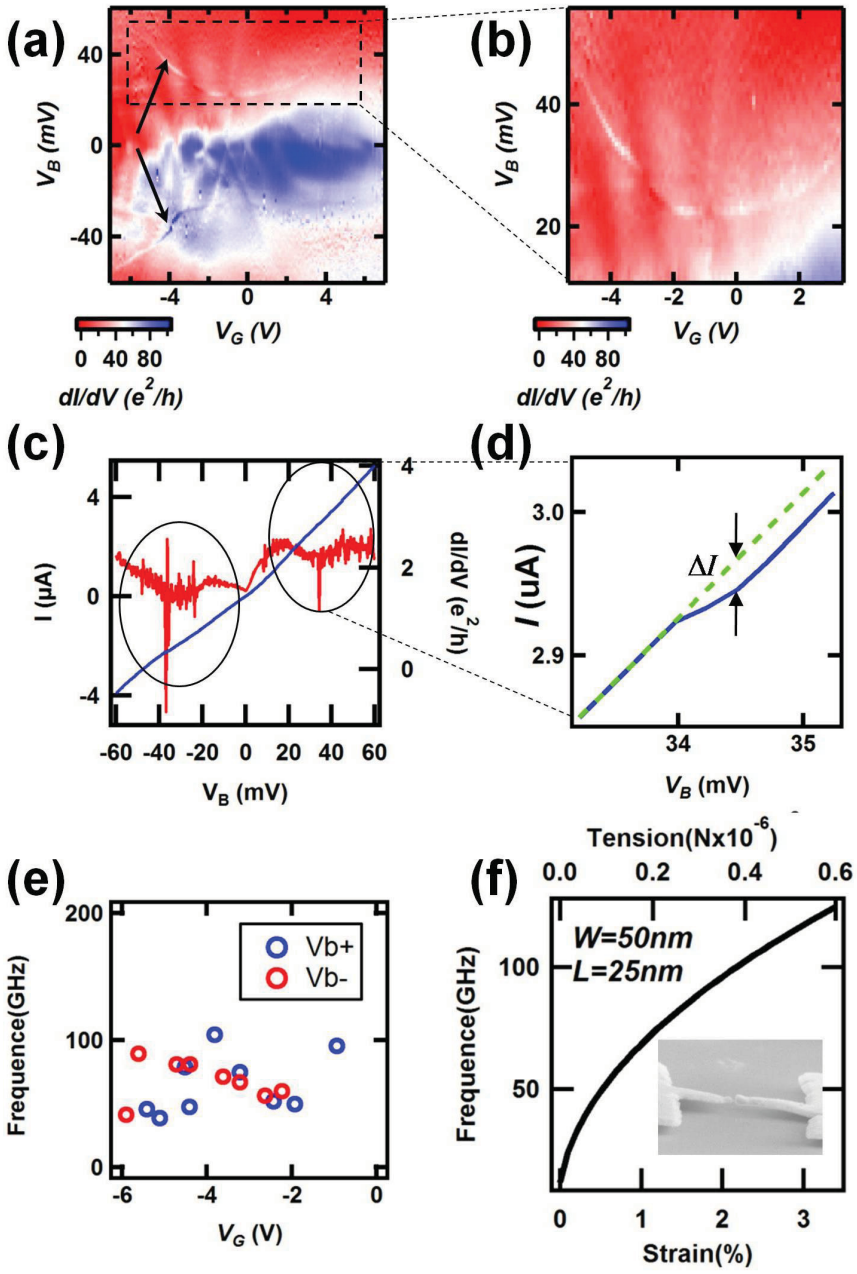

Figure 3.15: Signature of e-v coupling in the transport data of device Q1 (SEM in Fig. 3.11(b)). (a) $dI/dV - V_B - V_G$ data for device $Q1$ showing the strong dI/dV signature at negative and positive bias. (b) Zoom-in on the rectangular section of (a). (c) I (blue) and dI/dV (red) vs of V_{Bias}. The sharp dI/dV is visible (circled). (d) Zoom-in of I vs V_B of circled sections of (c). This indicates how ΔI is extracted. (e) Extracted vibrational frequency vs V_G for positive (blue) and negative (negative) V_B. (f) Frequency as a function of strain and tension for a suspended graphene resonator with the dimensions of Q1 from SEM imaging ($W = 50$ nm and $L = 25$ nm). Inset is a tilted SEM image of the device.

We see similar dI/dV signatures in Device Q3 (shown in Fig. 3.11(f)) as shown in

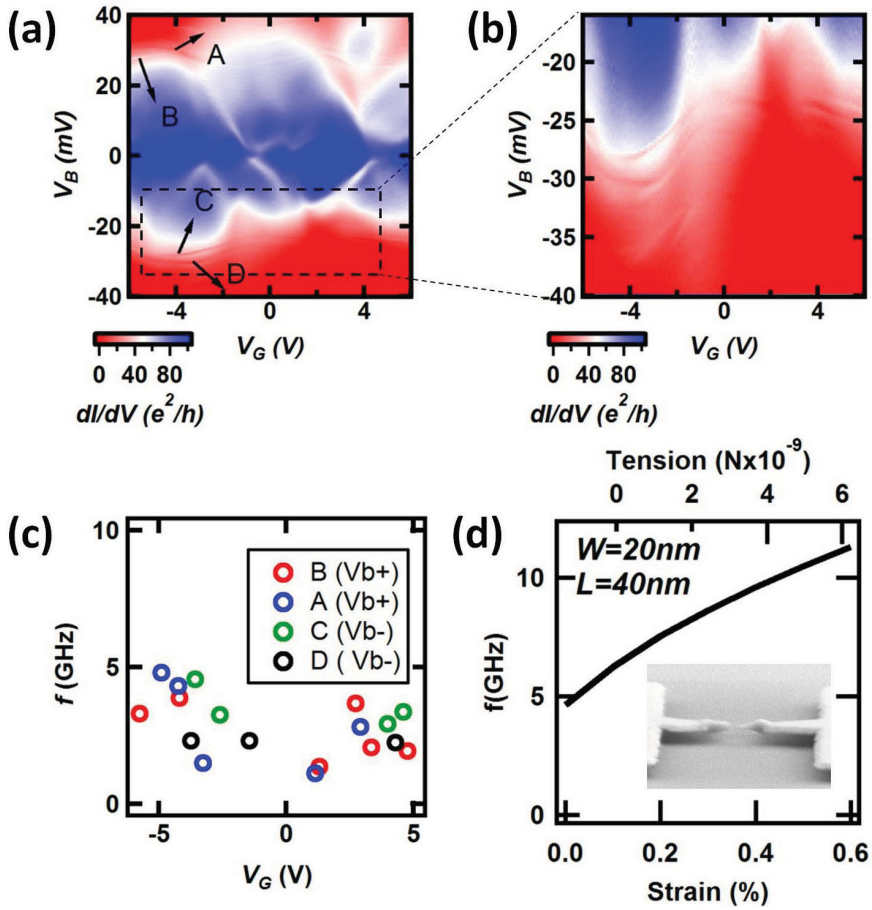

Figure 3.16: Signature of e-v coupling in transport data of device Q3. (a) $dI/dV - V_B - V_G$ data for device Q3 showing the strong dI/dV 2 pairs of signatures at negative and positive bias indicated by arrows and letters. (b) Zoom on the rectangular section of (a). (c) Extracted vibrational frequency vs V_G along the 4 line in (a) A, B, C and D. (d) Frequency as a function of strain and tension for a suspended graphene resonator with the dimensions from the SEM of the (W = 40 nm and L =20 nm). Inset is tilted SEM image of the device.

Fig. 3.16 which shows strong dI/dV vibrational features. Fig. 3.16(a) is the contour plot $dI/dV - V_B - V_G$ data of device Q3 showing 2 pairs of dI/dV signatures in positive and negative bias, shown by arrows and letters A, B, C and D. Fig. 3.16(b) expand the data range around the resonance in (a). Vibrational frequencies are extracted as far device Q1 from the ΔI from (a) and plotted in (c). We extract a frequency range of a few GHz, which is close to the 5 GHz theoretical frequency at zero tension and

strain (with $L = 40$ nm and $W = 20$ nm). A tilted SEM image of the device also confirms that the leads are suspended and almost straight (see inset of 3.16(d)), we would therefore expect very small tension on the flake.

We have shown that the extracted frequencies of the bending vibrons in our suspended graphene QDs are in reasonable agreement with the theoretical frequencies expected for graphene resonators of these dimensions. These QD-NEMS provide a platform for the study of electron-vibron coupling in samples with different geometries, as a function of magnetic field, temperature and external strain. Additionally, there is the potential to develop ultra-high frequency NEMS for mass and force sensors.

In this chapter, we described the electromigration and nanoetching technique used to generate our devices. We described how to make QDs by defect creation or graphene cutting. We achieved $\approx 20-30$ nm suspended graphene QDs, the smallest graphene QDs produced to date to our knowledge. The size of each of the QDs visible SEM imaging matches the area extracted from electron transport data, indicating that there is a very little "bulk" disorder in our dots. We observed signatures of e-v coupling in our devices through transport data. We extracted up to 100 GHz vibronic frequencies for our ultra-short graphene QDs. Suspended graphene quantum dots offer a platform to study the effects of strain in transport and e-v coupling. Our fabrication method offers the prospect of studying the various sources of disorder in graphene QDs.

Chapter 4

Ballistic transport in ultra short suspended graphene devices

Since the discovery of graphene there has been a growing interest in fabricating and studying nanometer scale graphene ballistic channels and *p*-*n* junctions [11, 56, 12, 13, 57, 58]. These devices are expected to be the building blocks for few nanometer-scale graphene quantum transistors [19, 59, 60]. In very small and disorder-free devices, electrons (or holes) can move ballistically. Having a ballistic channel requires that the length of the channel be smaller than the mean free path (mfp) and phase-coherence length of the carriers. Recently, a mean free path of up to the micron scale has been reported [12, 19] which has made it possible to fabricate micron scale long ballistic channels [19]. Ballistic charge carriers do not scatter, but preserve their quantum phase information, which makes them a platform to explore the quantum behaviour of Dirac electrons in graphene. Such optics-like phase coherence transport is very promising for the development of quantum wires, and quantum bits for quantum computing applications [61].

Transistors and logical circuits are based on *p*-*n* junctions. A *p*-*n* junction forms at the interface of two semiconductors (or semi-metal in the case of graphene) which are respectively hole (p) and electron doped (n). Thus, to fabricate a graphene-based ballistic *p*-*n* junction it is necessary to create a charge carrier density gradient in a sub-micron region. Usually, a secondary gate electrode (top or bottom) is used to form the density gradient [11, 19]. Fig. 4.1 shows a cartoon of a graphene *p*-*n*-*p* junction. A global back gate and a local top gate are used to electrostatically dope

graphene and create a charge carrier density gradient at the edges of the top gate. This configuration forms two p-n (or n-p) junctions back to back, i.e p-n-p (or n-p-n). The p-n-p junction is created when the global back gate hole, and local top gate electron, dope the graphene (or the other way around for a n-p-n junction). There has been a lot of effort to reduce the size of graphene p-n junctions. However the thickness of the necessary insulating layer between the gate and graphene limits the downsizing of the junction. So far $\gtrsim$ 50 nm scale p-n-p ($\approx$ 25 nm p-n) junctions have been achieved by using a local top gate [11, 13].

Here we demonstrate the fabrication of several suspended graphene ballistic n-

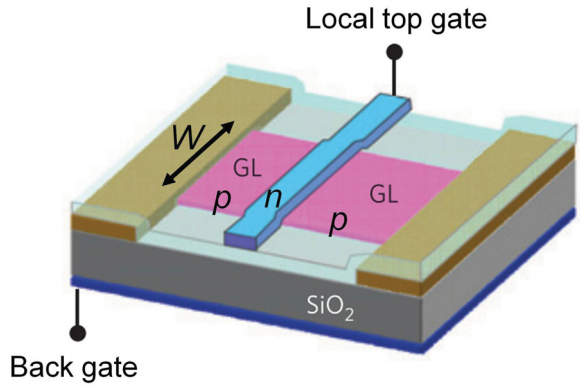

Figure 4.1: Cartoon of graphene p-n-p junction. It shows that the graphene p-n junction is formed by creating a density gradient using a local top gate. Adapted from reference [11].

p-n (or n-n'-n) junctions, whose sizes range from $\approx$ 100 nm down to only $\approx$ 23 nm ($\approx$ 10 nm p-n junction). To achieve this resolution we used gold contacts, not only to electrically contact the graphene, but also to dope (local gate) the graphene and create an ultra sharp density gradient. The difference in the work functions of the gold film and graphene leads to a charge transfer and doping of the graphene layer. There is also contribution from a metal-graphene chemical interaction, which results in a charge redistribution at the interface [57, 58, 62, 63, 64].

Because the spacing between graphene and the gold film deposited on the graphene is $\leq$ 1 nm, we can reduce the size of the n-p or (n-n') junction down to $\approx$ 10 nm. Fig. 4.2 (a)-(b) show tilted SEM images of 10 and 100 nm scale suspended graphene

transistors respectively. In the following section, we will describe the ballistic transport through the *n*-*p*-*n* junction formed in these devices. In our devices, we observed ballistic transport in agreement with the theory of Dirac fermions. We see Fabry-Pérot (FP) oscillations demonstrating coherent ballistic transport. FP oscillations result from the interference between the wavefunctions of reflected and transmitted carriers. The maximum coherence length (up to $\approx$ 700 nm) extracted from the FP oscillations in our devices is much longer than the length extracted from SEM images for these devices. This demonstrates that the ballistic transport extends under the gold contacts [10].

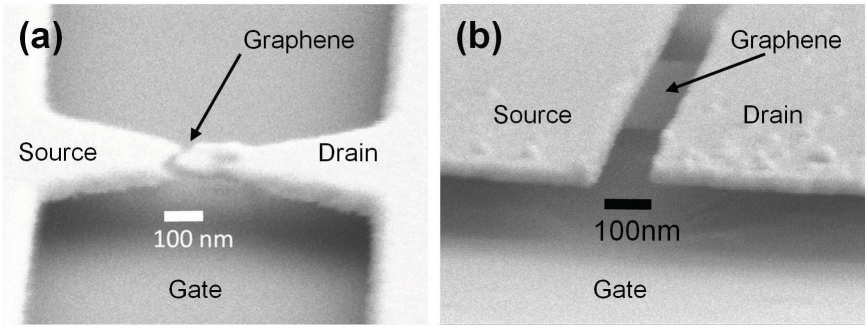

Figure 4.2: Tilted SEM image of our suspended graphene transistors. (a) 10 nm long suspended graphene transistor. (b) 100 nm long graphene ballistic transistor suspended between two gold contacts.

4.1 Theory of ballistic transport in graphene

In chapter 3 we discussed the fabrication of narrow and short graphene devices which can have band gaps and form graphene quantum dots. Here, we discuss wider channels which give rise to open quantum dots and ballistic transistors. The term open quantum dot refers to a QD where the discrete energy levels of the dots are broadened due to highly transparent tunnel barriers (i.e G is a sizeable fraction of e^2/h). Thus, an open QD is the intermediate regime between a regular QD and a fully ballistic channel. In this section we introduce a theoretical model, presented by *Tworzydlo et al.* [56] which describes ballistic transport in graphene. This model predicts the conductance due to Dirac fermions as a function of the Fermi energy for different

lengths, L, widths, W, and aspect ratio, W/L, of the channel. We also show that the predictions of this model are consistent with ballistic transport through graphene n-p-n or p-n-p junctions.

Fig. 4.3 shows a schematic of a graphene transistor contacted by two gold leads

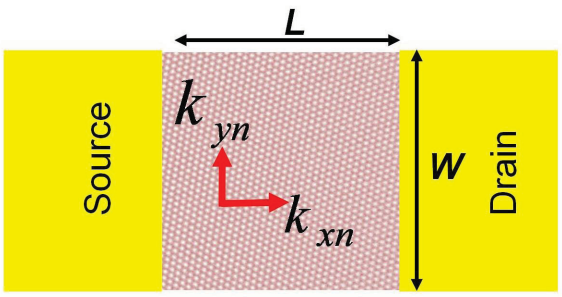

Figure 4.3: Cartoon of a graphene transistor contacted with gold leads (source and drain). k_{xn} and k_{yn} are the longitudinal and transverse momentum of carriers in the n^{th} ballistic mode (sub-band).

(source and drain). L and W are the length and width of the graphene transistor respectively. k_{xn} and k_{yn} are longitudinal and transverse momentum of the carriers injected into the n^{th} mode (i.e. subband) of the channel. The conduction modes form due to confinement from W, which quantizes the possible values of $k_y \rightarrow k_{yn}$ where n labels the n^{th} mode. The values of k_{yn} are [56]:

$$k_{yn} = \frac{\pi}{W}(n + 1/2) \tag{4.1}$$

where n is an integer number (mode number). It was predicted that Dirac fermions [17] experience perfect transmission at a normal incident angle ($\theta = 0$) due to Klein tunneling (see section 1.2.1). Fig. 4.4 shows the transmission for Dirac fermions as a function of their incident angle on the potential barrier [17]. It shows that transmission is highly angle dependent, and decreases for $\theta \neq 0$ on the potential barrier. The angle of injection for each mode is given by $\theta = \tan^{-1}(\frac{k_{yn}}{k_{xn}})$. Thus, a larger n results in a larger incident angle. Fig. 4.4 shows that for small incident angles ($\theta \approx 0$), *i.e.* small k_{yn} and n, transmission ≈ 1. Meaning, these modes cannot be stopped by any potential barrier. As k_{yn} increases the transmission drops quickly

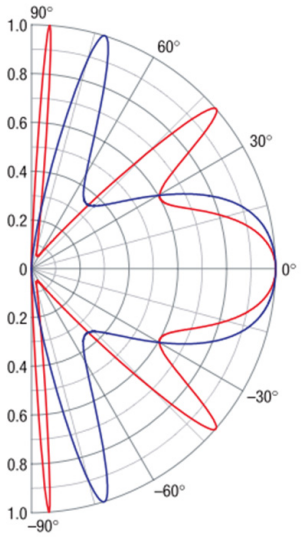

Figure 4.4: Angle dependence of Klein tunneling. Transmission probability of Dirac fermions through a potential barrier in graphene, as a function of the incident angle for a barrier height of 200 meV (red) and 285 meV (blue). The angle θ is defined by $\theta = \tan^{-1}(\frac{k_{yn}}{k_{xn}})$. Transmission decreases to values ≤ 1 when $\theta \neq 0$, but remains at 1 for any barrier height fir $\theta = 0$. Reproduced from reference [17].

to small values when $\hbar v_F k_{yn} > \mu$ where μ is the Fermi energy[1]. Thus, high angle and high energy modes are filtered (reflected) by the potential barrier. We can see in Fig. 4.4 the effect on the transmission of different barrier heights (200 meV (red) and 285 meV (blue)).

Transmission of the n^{th} mode is given by the following equation, considering that the Fermi energy in the leads is $\mu_{leads} = \infty$ [56]:

$$T_n = \left| \frac{k_{xn}}{k_{xn}\cos(k_{xn}L) + i(\frac{\mu}{\hbar v_F})\sin(k_{xn}L)} \right|^2 \tag{4.2}$$

$$k_{xn} = \sqrt{(\frac{\mu}{\hbar v_F})^2 + (k_{ny})^2} \tag{4.3}$$

Where T_n is the transmission for the n^{th} mode. $v_F = 10^6$ m/s is the Fermi velocity in graphene, μ is the Fermi energy of the carriers in graphene and can be tuned by V_G and temperature, [23, 24]:

$$\mu = \hbar v_F \sqrt{\pi n_{total}}, \quad n_{total} = \sqrt{(n_G^2 + 4(n_o)^2)} \tag{4.4}$$

$$n_G = \frac{C_G}{e} V_G, \quad n_o = \sqrt{(\frac{n_{imp}}{2})^2 + (n_{th})^2}, \quad n_{th} = \frac{\pi}{6}(\frac{k_B T}{\hbar v_F})^2$$

Where n_G and C_G are the carrier density induced by the back gate, and the back gate capacitance per unit area respectively. n_{imp} is the impurity density and n_{th}, k_B, T are the thermally generated carrier density, Boltzmann constant and temperature respectively. Finally, the conductivity of the transistor, σ, is given by the sum over the conductivity of each mode as follows:

$$\sigma = \frac{4e^2}{h}\frac{L}{W}\sum_{n=0}^{N-1} T_n \tag{4.5}$$

In the next sub-sections we will discuss the predictions of this model that are relevant to our measurements.

[1]Fermi energy, E_F, is the highest occupied single particle energy level in the system. At $T = 0$, E_F is the same as the chemical potential, μ.

4.1.1 Conductivity, σ, vs charge density and dimensions

Minimum conductivity: The *Tworzydlo et al.* [56] model predicts that the minimum conductivity, σ_{min}, of graphene when its Fermi level is at the Dirac point (zero charge carrier), is non zero (see Fig. 4.5(a)). This means that graphene-based transistors cannot be switched off. This is due to Klein tunneling, where there are always some evanescent modes (imaginary momentum) which travel between the leads with perfect transmission. σ_{min} depends on the aspect ratio, W/L, and for a wide transistor ($W \gg L$) it is close to $\frac{4e^2}{\pi h}$ ($\approx 25k\Omega$) (see Fig. 4.5(b)-(c)). The red curves in Fig. 4.5 (b)-(c) are σ_{min} (σ at $\mu = 0$) as a function of the aspect ratio, using $L = 100$ nm and $L = 10$ nm respectively. We see that for small aspect ratios σ_{min} can be much smaller than $\frac{4e^2}{\pi h}$.

Change in conductivity as the Fermi energy is gate modulated: *Tworzydlo et al.*

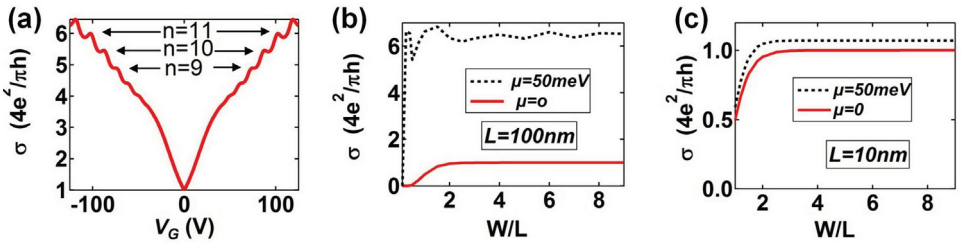

Figure 4.5: Conductivity, σ, vs charge density and dimensions. (a) σ as a function of gate voltage. (b) σ_{min} (red), *i.e.* at $\mu = 0$, and σ at $\mu = 50$ meV as a function of aspect ratio (W/L) for $L = 100$ nm. (c) σ_{min} (red) and σ at $\mu = 50$ meV as a function of aspect ratio (W/L) for $L = 10$ nm.

also predict that σ in longer graphene transistors can be more widely tuned by V_G. The black curves in Fig. 4.5 (b)-(c) show σ at $\mu = 50$ meV (corresponds to $V_G \approx 5$ V in our devices) as a function of W/L for $L = 100$ nm and $L = 10$ nm respectively. It shows that the change in conductivity modulation, $\Delta\sigma$=($\sigma_{max} - \sigma_{min}$), is much larger for long channels than for short ones for the same change in Fermi energy.

Conductivity oscillations: Some oscillations in σ are visible at high V_G in Fig. 4.5 (a). These oscillations are due to additional conduction modes becoming transport modes with a real $\vec{k}$, rather than evanescent modes with an imaginary $\vec{k}$ vector. As V_G increases the Fermi energy of the charge carriers increases. Since $k_{yn} = \frac{\pi}{W}(n+0.5)$ and the Fermi energy is $\mu = \hbar v_F \sqrt{(k_{yn})^2 + (k_x)^2}$, higher energy modes become transport

modes as V_G increases, and their contribution to the total transmission increases the conductance in steps. This is only expected if there is no mode mixing, and we expect our contact to mix modes so we should not see these features [65].
In the next section we will discuss ballistic transport through a single p-n junction and how it is consistent with the model discussed in this section.

4.1.2 Graphene based *p-n* junction

In this section we discuss transport across a single p-n junction. We conclude that transmission through a sharp p-n junction is very similar to the ballistic model discussed in section 4.1. A p-n junction is the interface between two types of semiconductors which are hole (p) and electron doped (n). A p-n junction in graphene is formed by creating a potential step or carrier density gradient. Figure 4.6 shows a cartoon of the potential step across a graphene p-n junction. The left side of the junction is hole (p-doped) and the right side is electron (n-doped) doped. A p-n junction can be created by using a local gate to locally dope graphene and form a carrier density gradient (see Fig. 4.1). [11, 19, 66]. It was calculated that the resistance of a

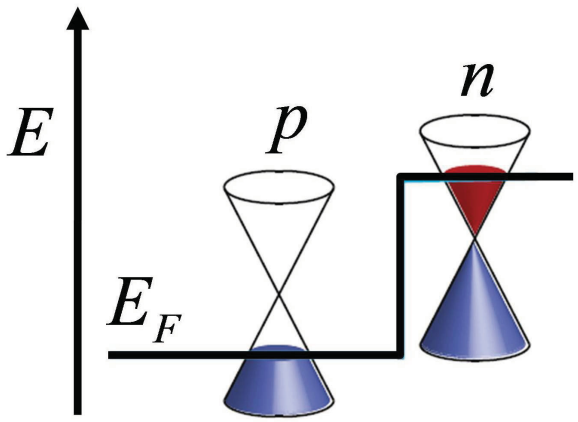

Figure 4.6: Diagram of a p-n potential barrier. A p-n junction is formed at the interface of a hole-doped (left) and electron-doped (right) graphene. Adapted from [19]

graphene p-n junction, R_{pn} is given by [66, 67]:

$$R_{pn} = \frac{\pi h}{2e^2}\frac{1}{W}\sqrt{\hbar v_F/e|F_{pn}|} \tag{4.6}$$

$$e|F_{pn}| \;=\; 2.5\hbar v_F \alpha^{1/3} (\rho')^{(2/3)} \tag{4.7}$$

Where F_{pn} is the electric field at the p-n junction, and can be extracted from the carrier density gradient, ρ', and $\alpha = e^2/\kappa\hbar v_F$ is the strength of the Coulomb interaction, where κ is the effective dielectric constant. Equation 4.6 shows that transmission through a p-n junction is very sensitive to the gradient of carrier density as well as the width, W, of the junction. Equation 4.6 can be expressed as a function of the density induced by the global back gate, ρ_2, and local gate ,ρ_1, as follows [67]:

$$R_{pn} = \frac{1}{W}\frac{0.7}{\alpha^{1/6}}\frac{h}{e^2}\left(1 - \frac{\rho_1}{\rho_2}\right)^{2/3}\left|\frac{D}{\rho_1}\right|^{1/3} \tag{4.8}$$

Where D is the spacing between the local back gate and graphene.

In Fig. 4.7 we calculate the conductance, G, vs V_G for $L = 100$ nm and $W = 1.5$ μm , with $\mu_{leads} = \infty$ (red solid line), and $\mu_{leads} = 0.26$ meV (blue point line) using the ballistic model which was discussed in section 4.1. The $\mu_{leads} = 0.26$ meV is the expected doping for graphene covered by gold [68]. We also plot G vs V_G for resistance of a single p-n junction (equation 4.8) for $\rho_2 = n_{gate}$, $\rho_1 = n_{gate} + 5 \times 10^{12}$ cm^{-2} which corresponds to $\mu_{leads} = 0.26$ meV (black dashed line), $D = 0.5$ nm [57] (spacing between gold and graphene, no adhesive layer is used) and $W \approx 1.5$ μm. All three models are in agreement as long as the doping from the contact is much bigger than the doping from the back gate, which is the case for our samples. In addition, the p-n interface is sharp and forms a large gradient.

It is expected that the ballistic resistance of one p-n junction is almost the same as the resistance of p-n-p (n-p-n) or a series of p-n junctions [69], since the p-n junction potential barrier filters out (reflects) the modes with large incident angles. The modes that are filtered out in the first p-n junction do not contribute to the transmission. However, the following p-n junctions are transparent to the modes which were transmitted from the first p-n junction ($\theta \approx 0$), so the transmission remains the same.

Comparing the p-n junction model and ballistic model (section 4.1), it is expected that both approaches lead to the same result for a sharp p-n density gradient. The ballistic transistor model consists of two sharp p-n junctions back-to-back, which forms a n-p-n junction. The p-n junctions are sharp because they are formed at the interface of suspended and metal covered graphene. While the graphene under the

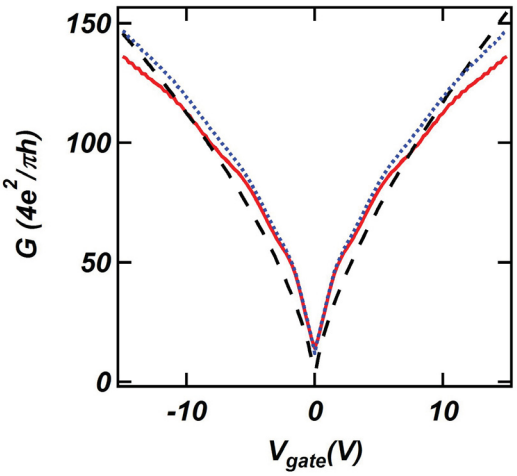

Figure 4.7: Transmission as a function of back gate (global gate). Red curve shows ballistic model for $\mu_{leads} = \infty$. Blue is the ballistic model for $\mu_{leads} = 0.26$ meV. Black curve is the p-n junction model for $\mu_{leads} = 0.26$ meV where $D = 0.5$ nm

metal can be highly doped by the metal, the suspended side charge density is tuned by a back gate voltage. This gives rise to a very sharp p-n junction at the interface of graphene and graphene covered by gold. In our samples, gold directly touches graphene since we do not use any adhesion layer, such as Ti or Cr. Moreover, the junction is suspended and annealed. Thus, we expect to have sharp p-n junctions at the interface of graphene and graphene covered by gold. Since the spacing between gold and graphene is only a few angstroms [57] it will not be a limiting factor in downscaling of the p-n junctions.

In the next section we will briefly summarize state-of-the-art results on graphene p-n junctions and ballistic transistors. We will also discuss the limitations of current results and how our work can make new and significant contributions to this field.

4.1.3 Experimental background

We review a few recent, high profile results to highlight the present state of affairs in ballistic transport in graphene.

Since the discovery of graphene, there has been a growing interest in graphene-based nanoelectronics, p-n junctions and transistors. One of the shortest graphene p-n junctions to date was reported in 2009, *Andrea F. Young et al.* [11] (see Fig. 4.8(a)).

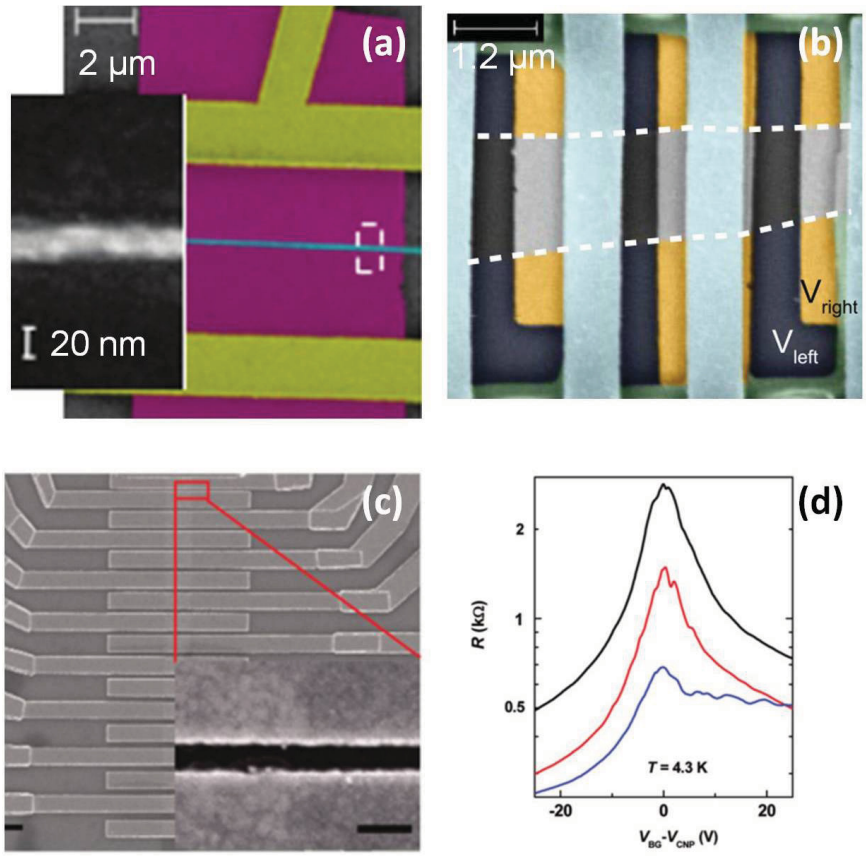

Figure 4.8: Recent experimental results on graphene p-n junctions and ballistic transistors (p-n-p). (a) False color SEM image of a graphene 67 nm p-n junction Andrea F. Young [11]. Contacts and graphene are colored yellow and blue, respectively. The local top gate is also colored blue. The scale bar is $2\mu m$. Inset is a zoom-in on the local top gate. The scale bar is 20 nm. Reproduced from reference [11]. (b) False color SEM image of a graphene p-n junction. Contacts are colored blue and bottom local gates are yellow. Scale bar is $1.2\mu m$. Reproduced from reference [19]. (c) SEM image of a 52 nm long graphene ballistic channel. (d) Resistance as a function of gate voltage for devices shown in (c). (black) 500 nm long, (red) 170 nm, and (blue) 52 nm.

They fabricated a 67 nm-long graphene p-n junction. They made use of a top gate to create a density gradient in graphene deposited on a SiO_2 substrate. In 2012, *Y. Wu et al.* [13] made a 52 nm long ballistic transistor (p-n-p) in graphene on a SiO_2 substrate (see Fig. 4.8 (c)). They observed FP oscillations in R vs V_G data (Fig. 4.8 (d)) as well as an asymmetry between hole transport ($V_G < 0$) and electron transport ($V_G > 0$). The asymmetry in transport is because when $V_G > 0$, the device is p-n-p, while at $V_G < 0$ is p-p'-p. This leads to a different resistance for $V_G > 0$ and $V_G < 0$. In these devices, the p-n junctions are at the interface of graphene and graphene covered by metal. These devices are similar to our devices, however our devices are suspended, annealed and smaller.

In 2013, *Peter Rickhaus et al.* [19], made micrometer-scale suspended and clean graphene ballistic p-n junctions. They made use of two bottom gates to create the p-n junctions (see Fig. 4.8 (b)). Current annealing was used to anneal the sample. They observed coherence transport up to ≈ 1.2 μm in graphene.

In summary, $\geq$ 52 nm ballistic graphene channels (on substrate) and 67 nm p-n junctions have been achieved, but there are some limiting factors which prevent the production of smaller ballistic and p-n junctions. In the next section, we mention these limitations and our approach to resolve some of them.

4.1.4 Limitations of previous work and our contribution

One of the difficulties in downscaling graphene p-n junctions is the thickness of the insulating spacer between the local gate and graphene. This insulating layer has to be thick enough to prevent current leakage, but it complicates the fabrication and limits the sharpness of the p-n junction to a length scale at least comparable to its thickness. The electric field lines from the local gate broaden as the spacing between the local gate and graphene increases. This forms a smooth charge density gradient in graphene, instead of a sharp one, leading to wide p-n junctions. As an example, in the device shown in Fig. 4.8 (a), the width of the local top gate is about 20 nm and the insulator spacer $\approx$ 30 nm, but the length of the p-n junction is reported to be about 67 nm.

Creating a ballistic channel requires removing sources of disorder. Suspension of the channel removes the substrate disorder and high temperature annealing cleans the sample of contamination and fabrication residues. For most of the reported

devices, suspension is very difficult due to the geometry of the device and complexity of the fabrication process. For devices on substrate, the Joule self-heating annealing process would not be effective since the devices are thermally coupled to the substrate, preventing them from reaching the high temperatures needed. These factors can limit achieving high-quality and short graphene ballistic p-n junctions and n-p-n transistors.

We have developed a nanoetching technique to create $5-10$ nm long graphene

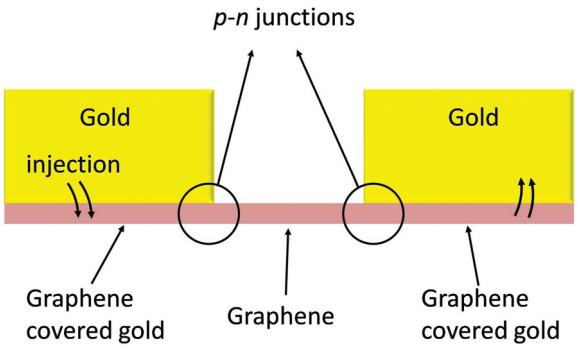

Figure 4.9: Schematic of graphene/graphene-covered-gold interface. Graphene is gated by a gold film forming a p-n junction at the graphene/graphene-covered-gold interface.

p-n junctions. This resolution is beyond the limit of electron beam lithography (see Fig. 4.2). We use BOE etching to etch away the SiO_2 substrate and suspend the device. In this way, we decouple the channel from the substrate disorder. We make use of a current annealing process to self-anneal our devices to high temperatures. It removes the contamination and residues, such as resist and H_2O from the device, which is kept under high vacuum. We also use gold electrodes to gate graphene. Gold in contact with graphene n-dopes graphene[2], which results in the formation of n-p-n or n-n'-n junctions, depending on the doping from the back gate. Since gold is touching graphene, the space between gold and graphene is minimized to a few angstroms, resulting in doping graphene by gold. This doping arises from a difference in the work functions of the gold film and graphene, which leads to a charge transfer and doping of the graphene layer [57, 58, 63, 64]. Figure 4.9 shows that graphene is gated by a gold film forming a p-n junction at the graphene/graphene-covered-gold

[2]Gold can also p-dope graphene if it is not annealed but high temperature annealing removes the oxygen from gold and changes its work function so that n-dopes graphene [70].

interface. This way the device consists of graphene contact (graphene-covered-gold) and gold gates. This allows the formation of a very sharp density gradient and consequently, an ultra short and sharp p-n junction.

In the next section, we will present the electromigration process to make 10 nm scale suspended graphene p-n junctions. We will show how we can use nanoetching to fabricate wide and short channels.

4.2 Electromigration of 10 nm-scale ballistic (p-n-p) transistors

We make use of a feedback controlled electromigration to open a nanogap in suspended break-junctions, as we explained in chapter 3. Here, we discuss how to adapt the procedure to fabricate wider but short junctions, such that graphene is not in the QD regime (with a band gap) but rather is ballistic. Fig. 4.10 shows the electromigration process which led to a 26 nm long n-p-n and 92 nm wide junction (Device A). We made use of the feedback control mechanism to break the junction at low power, with the same technique that was presented in section 3.2. Then, we annealed the junction using Joule self-heating to a high temperature (explained in Section 3.3). Since the junctions are suspended, the heat created by Joule heating increases the temperature of the channel. This ashes the contamination on graphene and on the gold contacts, which results in clean graphene in both the exposed channel and under the suspended gold contacts. The portion of the gold contact which is on the substrate (SiO_2) is not annealed due to thermal anchoring to the substrate, and thus remains disordered. Fig. 4.10 (a) shows $I - V_B$ during electromigration for Device A. The final break happened at about 4.7 mW ($V \approx 0.63$ V and $I \approx 7.8$ mA), and was followed by a current annealing step up to $V \approx 1.7$ V and $I \approx 0.73$ mA (Inset in Fig. 4.10 (a)). Fig. 4.10 (b) shows the false color top view SEM image of Device A after this process (dark blue, yellow and purple correspond to SiO_2, gold contact and graphene, respectively). The channel of Device A is ≈ 26 nm long and ≈ 92 nm wide.

The same recipe is used for Device C (Fig. 4.11), but with a higher voltage. The channel of Device C is ≈ 23 nm long p-n-p and ≈ 32 nm wide. Device C was broken at about 13 mW ($V \approx 1.1$ V and $I \approx 11.8$ mA) followed by current annealing up to $V \approx 0.9$ V and $I \approx 0.16$ mA. SEM images of samples A and C show that the graphene

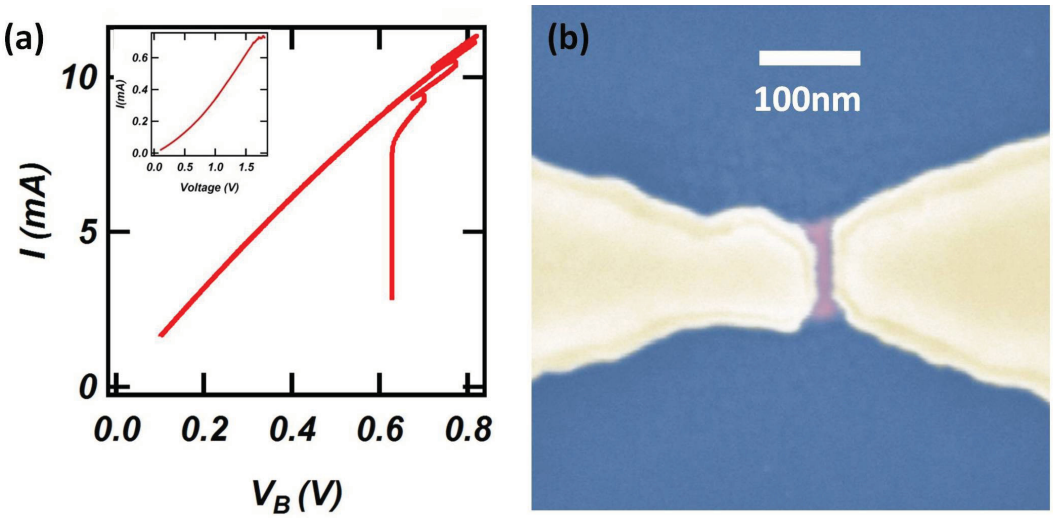

Figure 4.10: Electromigration of ballistic transistor Device A. Low-power electromigration of suspended break-junction followed by current annealing results in the formation of short and wide graphene channels. (a) I vs V_B of the electromigration curve for Device A. Device A was broken at 4.7 mW ($V \approx 0.63$ V and $I \approx 7.8$ mA) followed by a current annealing step (inset) up to $V \approx 1.7$ V and $I \approx 0.73$ mA. (b) Top view false color SEM image of Device A showing the geometry of the graphene channel. Dimensions of the relatively rectangular channel are $L \approx 26$ nm and $W \approx 92$ nm. Dark blue, bright yellow and purple correspond to SiO_2, gold contact and graphene, respectively.

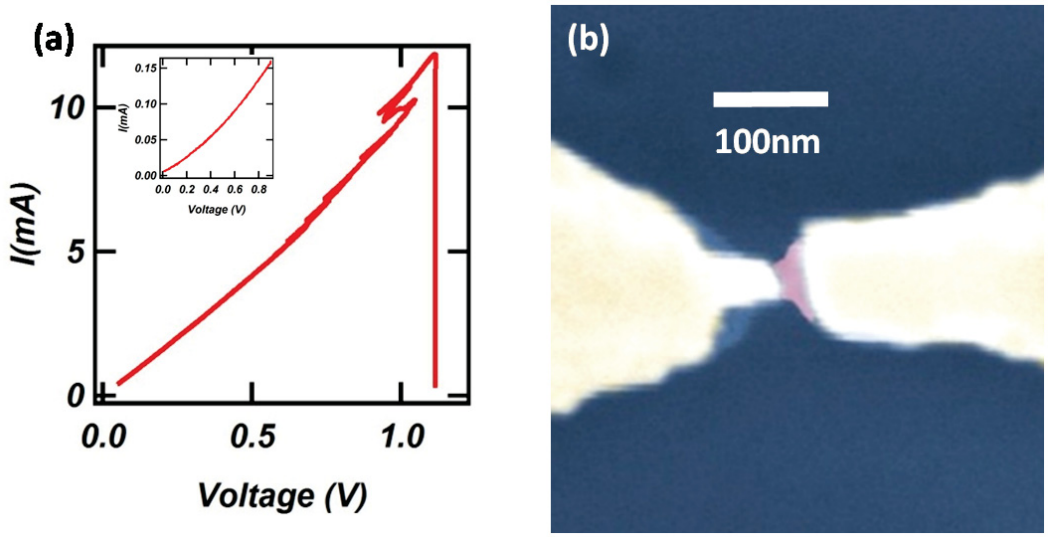

Figure 4.11: Electromigration of ballistic transistor Device C. Low-power electromigration of suspended break-junction Device C. (a) $I-V_B$ data of the electromigration curve for Device C. Device C was broken at 13 mW ($V \approx 1.1$ V and $I \approx 11.8$ mA), and then current annealed (inset) up to $V \approx 0.9$ V and $I \approx 0.16$ mA). (b) Top view false color SEM image of Device C showing the geometry of the graphene channel. Dimensions of the relatively rectangular channel are $L = 23$ nm and $W = 32$ nm. Dark blue, yellow and purple correspond to SiO_2, gold contact and graphene, respectively.

channel is relatively rectangular and of roughly the same length, but of very different widths. This is in agreement with the discussion in chapter 3 where we explained how a larger breaking V (or electric field) leads to cutting the channel into narrower ribbons.
In the next section, we will present the transport data for Device A and C as well as for wider ($W \approx 1$ μm) Devices (F and M).

4.3 Data: ballistic Dirac fermion transport

We present and discuss the transport data measured in devices with an aspect ratio, $W/L \geq 1$ and while length ranges from ≈ 23 nm up to ≈ 105 nm. We fabricated and measured a total of ten devices, and focus our discussion on the four devices for which we have the most complete data set. We show that the data are in good agreement with the theoretical model presented in section 4.1 for the transport of ballistic Dirac fermions in graphene, and demonstrate *n-p-n* transistors as short as 23 nm. To the best of our knowledge these are the shortest such devices reported.

To show the sensitivity of the model (equation 4.2) on the length, L, and width, W, of the channel we plot the experimental and theoretical conductance, G, as a function of V_G in Fig. 4.12. The black line shows the experimental data and the blue dashed line the theory using the L and W extracted from the SEM image of Device C (see Fig. 4.11 (b)). We also plot the theoretical G for the same W but where $L \rightarrow 2L$ ($W = W_{SEM} = 32$ nm, $L = 2L_{SEM} = 46$ nm, green dashed-dotted line) as well as for $W \rightarrow 2W$ and L ($W = 2W_{SEM} = 64$ nm, $L = L_{SEM} = 23$ nm, red dashed line). L_{SEM} and W_{SEM} are the length and width measured from the SEM image, respectively.

The model is also very sensitive to the device geometry, and does not work for rough edges and non-rectangular edges. We plot the experimental (black solid line) and theoretical (dashed-dotted blue line) G vs V_G for Device B in Fig. 4.13. As is clear from the SEM image in Fig. 4.13 (a), the edges of the channel in Device B are not rectangular, which result in a discrepancy from the model. This is explained by the fact that roughness and non-rectangular edges change the angle of the injection and affect the total transmission in a way which is not captured by the theoretical model.

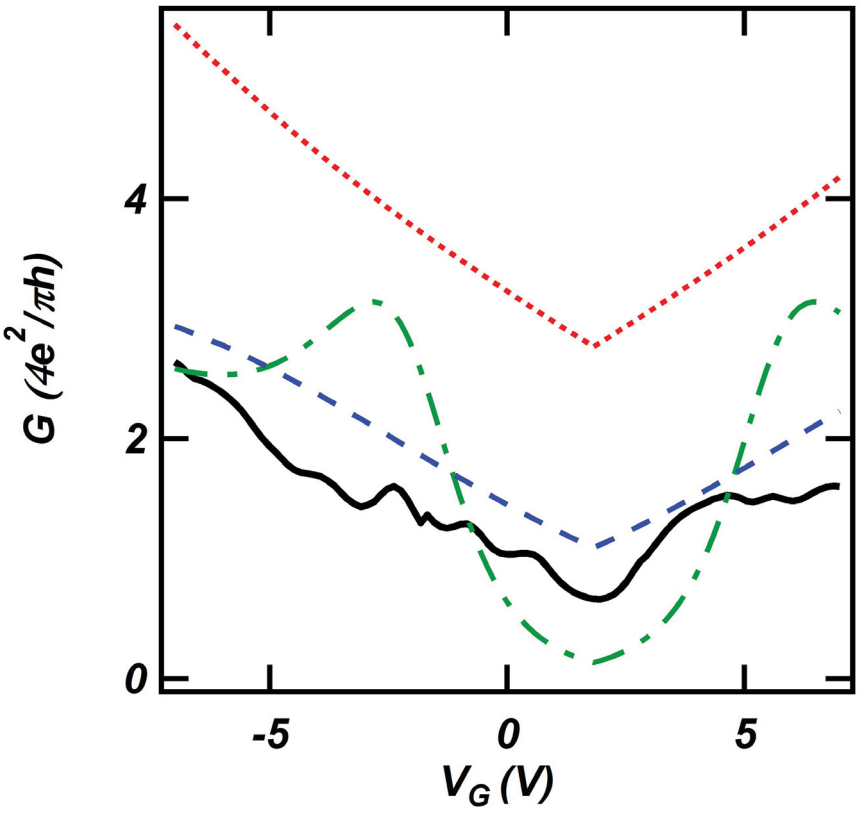

Figure 4.12: Conductance (G) of Device C as a function of gate voltage. Black solid line shows experimental data. Blue dashed line is the theoretical model predicting ballistic transport in graphene for length and width extracted from the SEM image for Device C ($L = 23$ nm and $W = 32$ nm). Green dashed-dotted line is the theoretical model plotted for Device C with width equal to the SEM width, but the length is twice as long ($L = 46$ nm and $W = 32$ nm). Red dotted line is the theoretical model plotted for Device C with length equal to the SEM length, but the width is twice as wide ($L = 23$ nm and $W = 64$ nm)

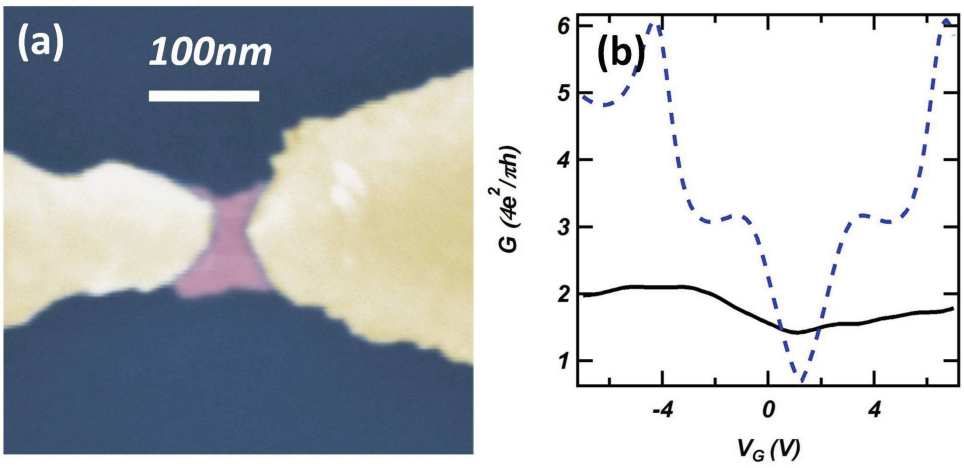

Figure 4.13: Conductance (G) of device B as a function of gate voltage. (a) SEM image of Device B shows non-rectangular edges. (b) G vs V_G for Device B. Black solid line shows experimental data. Blue dashed line is the theoretical model $L_{average} \approx 64$ nm and $W_{average} \approx 54$ nm extracted from the SEM image. (b) indicates that the theoretical model does not work for devices with rough and non-rectangular edges.

No contact resistance or fitting parameter are added. Comparing the experimental data with the theoretical curves show that there is an agreement between the experimental data and model using $W = W_{SEM}$ and $L = L_{SEM}$ for the devices with rectangular edges. It also shows that conductance is very sensitive to geometry, L and W, which confirms that our sample dimensions (SEM) match the ones describing the model. This strongly suggests that the suspended channel visible in the SEM image is not damaged and is ballistic.

Moreover, since the charge neutrality point (Dirac point) is very close to $V_G \approx 0$ (see Fig. 4.12) we conclude that the sample is very clean, since impurities shift the Dirac point away from $V_G = 0$ [18]. In addition, we observe highly reproducible oscillations in conductance (see Fig. 4.12). We will explain in section 4.4 that these oscillations arise from quantum coherent interferences between transmitted and reflected charge carriers. This optics-like interference in transport, called Fabry-Pérot interference, also confirms that our devices show ballistic and phase coherent transport. We do not see such oscillations in the theoretical model which only predicts them at much higher energies (larger V_G). We will explain the origin of the experimental interferences in section 4.4

Fig. 4.12 shows a semi-quantitative agreement between the experimental data and theory. However, this agreement can be further improved if we include the effects of contact resistance and impurities. The origin of contact resistance, R_C, arises from the injection of the charge carriers from the gold into the graphene. Although current annealing removes most of the impurities from the sample, a small density of impurities (n_{imp}) always remains. These impurities effectively smooth the G vs V_G curve around $V_G \approx 0$. In Fig. 4.14 (c) we show that including R_C and n_{imp} into the theoretical model increases the agreement with the experimental data. R_C in our sample is much smaller than the total resistance of the samples. The R_C fit parameter extracted from several of our of samples is plotted with respect to the width of the samples in Fig. 4.14 (b). We see that R_C is inversely proportional to W, as it is expected for p-n junctions (equation 4.6). The contact area of our devices is estimated to extend within a radius of one μm. This corresponds to the maximum injection length measured in graphene (see Fig. 4.14 (a)) [71]. We use this area to calculate R_C per unit of area between graphene and gold in our samples:

$$\begin{aligned} R_C &= \frac{R_\square}{A} \\ R_C &= \frac{R_\square}{A_L} + \frac{R_\square}{A_R} \\ R_\square &= R_C(\frac{1}{A_L} + \frac{1}{A_R})^{-1} \end{aligned} \tag{4.9}$$

Let $R_\square$ be the contact resistance for one μm^2, and A_L and A_R be the left and right contact areas (area of graphene covered by gold for our devices). We find $R_\square \approx 230 - 400\ \Omega\ \mu m^2$ in our sample. This is very close to the reported values in the literature (see Fig. 4.14 (b)) [23]. Charge impurities result from fabrication residues and H_2O on graphene. The density of impurities, n_{imp}, can be etched from the HWHM (half width half maximum) of R vs n in the diffusive regime [23]. We use an impurity density of $n_{imp} \approx 5 \times 10^{10}\ cm^2$, which we extracted from our diffusive samples, which were prepared and annealed with the same procedure as our ballistic devices. Fig. 4.14 (c) shows the effect of adding impurities (orange dashed-dotted line) in the model. It modestly shifts the minimum conductivity, however far away from the Dirac point this change becomes negligible.

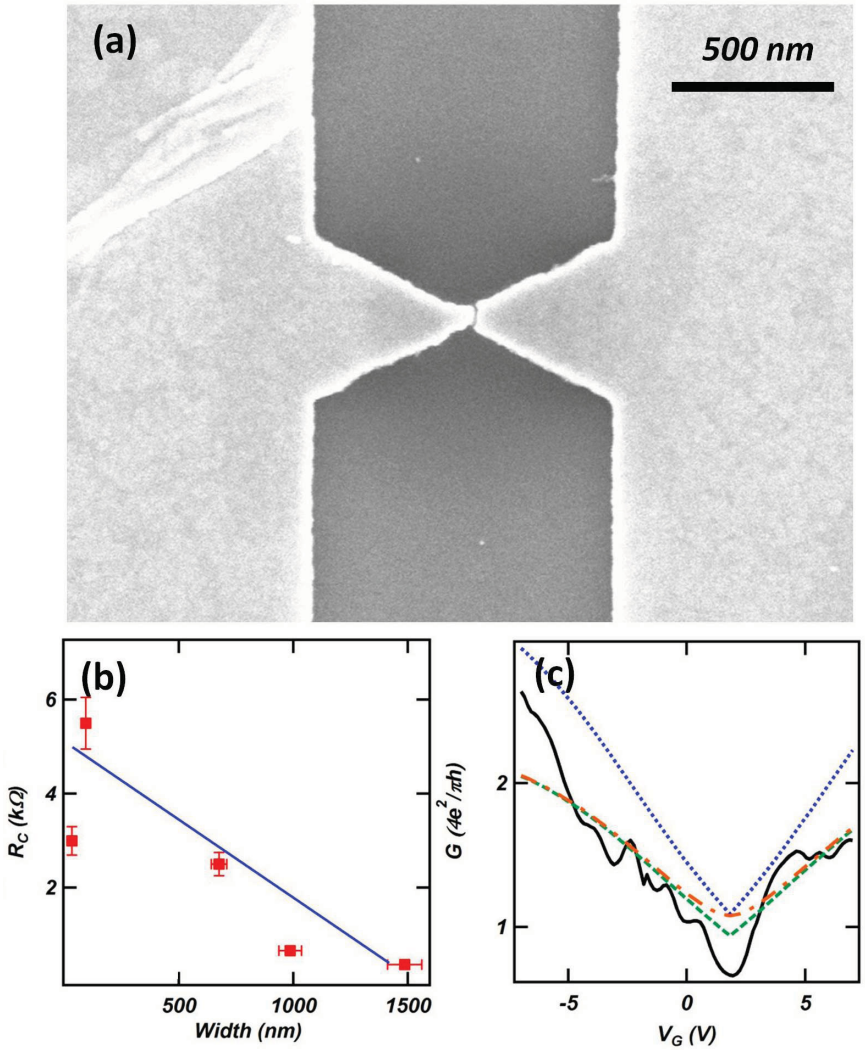

Figure 4.14: Conductance (G) of Device C as a function of gate voltage, including contact resistance and impurities. (a) SEM image of a device showing how the contact area is extracted using a 1μm radius. (b) Contact resistance, R_C, of our devices as a function of width of the samples. (c) Conductance, G of Device C vs V_G. The black solid line shows the experimental data. The blue line is the G predicted by theory for L and W from the SEM image of Device C ($L = 23$ nm and $W = 32$ nm). The green line is the model plotted for Device C with the same dimensions and with a contact resistance ($R_\square = 241\ \Omega\mu m^2$). The orange line is the theory plotted for Device C with the same dimensions and $R_\square$ and with an impurity density of $n_{imp} = 5 \times 10^{10}\ cm^2$.

4.3.1 Agreement of experimental data with the theoretical model

We now compare data from four samples covering a broad range of L, W and W/L ratio. We show data for two ultra short ($L \approx 20$ nm) devices whose $W \approx 32$ and 92 nm. We also show data for two samples whose $L \approx 100$ nm, and $W \approx 1.5$ and 1 μm (see table 4.1).

All of these devices are suspended and decoupled from the substrate disorder. We made use of current annealing to remove contamination and fabrication residues. In the widest devices (F and M) edge disorder has a much smaller effect on transport, and the data show an even better agreement with the theory. Thus, substrate disorder, contamination and edge disorder has been removed or minimized in these devices.

Table 4.1: Width, length and aspect ratio for four Devices A, C, F and M (shown in Fig. 4.15)

Device	W_{SEM} (nm)	L_{SEM} (nm)	aspect ratio (W/L)
A	92	26	3.5
C	32	23	1.4
F	985	98	10.1
M	1485	105	14.1

Fig. 4.15 shows low temperature ($1.5 - 4$ K) G vs V_G for Devices A, C, F and M. We limit our V_G to $\leq$ 15 V for Devices F and M (gap junctions) and $\leq$ 7 V for Devices A and C (break-junctions), because the samples are suspended and the electrostatic force from the gate electric field could collapse the devices. The black lines in Fig. 4.15 are the experimental data and the red curves show the ballistic model. We observe good agreement between the theory and experimental data over a wide range of length, width and aspect ratio. The minimum conductivity, σ_{min} is close to what the model predicts when including contact resistance and impurities. We used $n_{imp} = 5 \times 10^{10}$ cm^{-2} for all samples. We observe better agreement between theory and experimental data in the devices with a rectangular shape and smooth contact edges, compared to non-square ones with rough edges.

If we compare transport on the electron side (positive V_G) with the hole side (negative V_G) we notice an asymmetry for all samples. This is evidence of the creation of a strong n-p-n junction in the channel.

We observed highly reproducible coherent oscillations in conductance at low bias

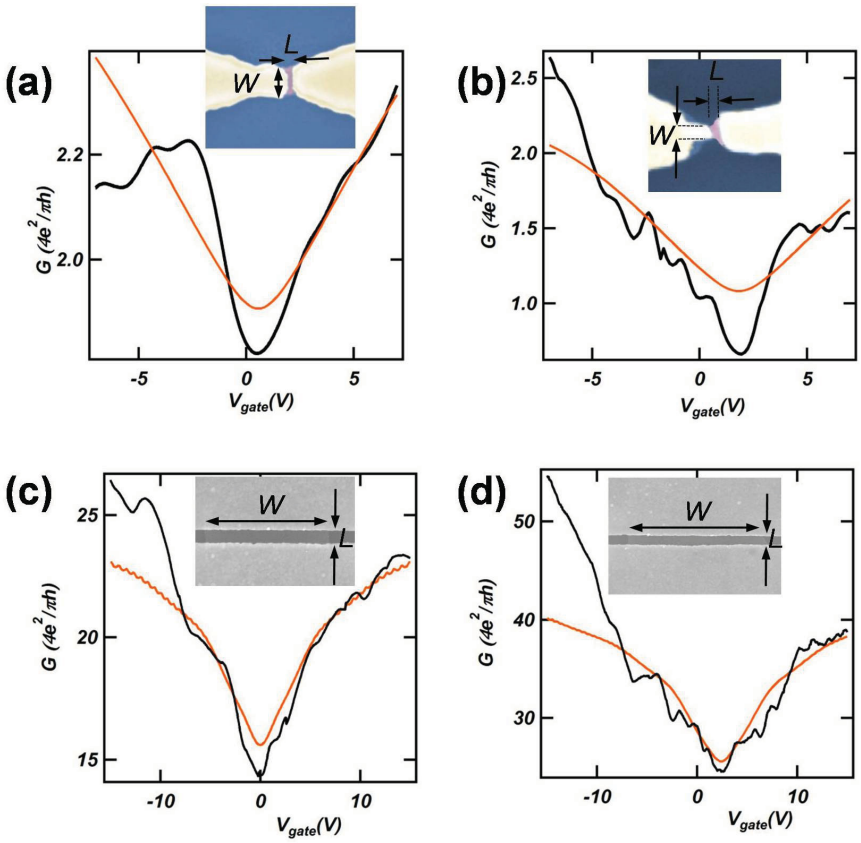

Figure 4.15: $G - V_G$ data for ballistic devices. The black curves are the experimental data and the red curve are the theoretical calculations. (a) Device A, $W = 92$ nm, $L = 26$ nm with $R_\square \approx 394\ \Omega\ \mu\text{m}^2$. Data taken at $T = 4.2$ K. (b) Device C, $W = 32$ nm, $L = 23$ nm and $R_\square \approx 241\ \Omega\ \mu\text{m}^2$. Data taken at $T = 4.2$ K. (c) Device F, $W = 985$ nm, $L = 98$ nm and $R_\square \approx 334\ \Omega\ \mu\text{m}^2$. Data taken at $T = 1.5$ K. (d) Device M, $W = 1485$ nm, $L = 105$ nm and $R_\square \approx 227\ \Omega\ \mu\text{m}^2$. Data taken at $T = 1.5$ K. Impurity density for all the samples is $n_{imp} = 5 \times 10^{10}\ \text{cm}^{-2}$.

and low temperature. These oscillations are another signature of coherent ballistic transport. We will discuss these oscillations in detail in the next section. In $L \approx 20 - 30$ nm devices we do not expect to see such coherent oscillations, because it requires reaching a much higher Fermi energy (higher V_G) than we can access. But surprisingly, we see low energy oscillations in all the samples. In section 4.4 we will discuss these low energy oscillations which apparently come from longer length scales than the ones seen in the SEM images.

4.4 Fabry-Pérot oscillations and quantum coherent transport

We first introduce the concept of Fabry-Pérot (FP) oscillations as a result of quantum coherent transport in graphene. We then use this framework to analyze the conductance oscillations visible in the data of Fig. 4.15. We will analyze the FP oscillations as a function of Fermi energy (see equation 4.4) at different V_B and T to extract the coherence length, L_{FP} of the charge carriers in our devices.

In ballistic transport, charged carriers do not scatter while traversing the device (except for elastic scattering at the source and drain contacts), and therefore they preserve their quantum phase information. This leads to interferences between the wavefunctions of reflected and transmitted carriers (see Fig. 4.16). This optics-like interference is called Fabry-Pérot interference. The coherence length (length over which the quantum phase is preserved) is very sensitive to disorder. The presence and amplitude of FP oscillations are good measures of the quality of the samples. The length of the FP cavity can be extracted from the energy spacing between subsequent FP fringes (ΔE) [13, 72]:

$$\begin{aligned} \Delta E = E_2 - E_1 &= \frac{\pi \hbar v_F}{L} \\ E_F &= \hbar v_F \sqrt{\pi n_{total}} \end{aligned} \tag{4.10}$$

Where n_{total} is the total carrier density in the channel given by Eq. 4.4 as a function of V_G, T and n_{imp}.

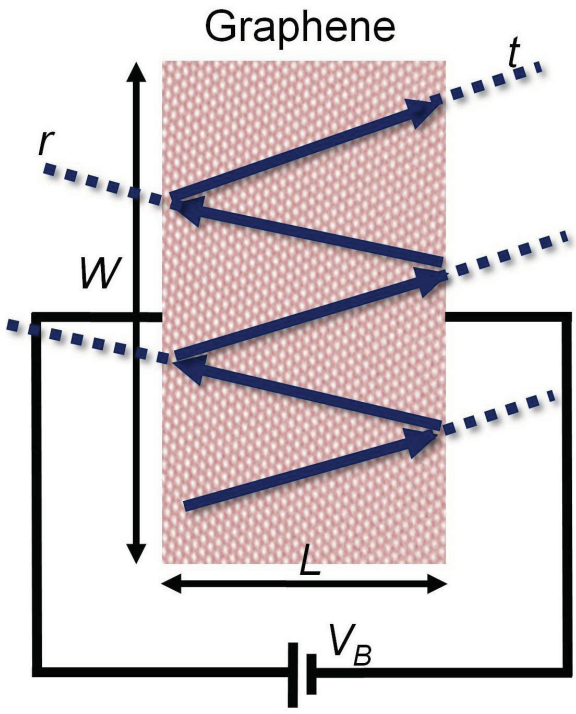

Figure 4.16: Cartoon of a graphene channel showing reflected and transmitted modes.

4.4.1 Length of the FP cavity and its dependance on T and V_B

Figure 4.17 shows transport data for Device F ($W = 985$ nm, $L = 98$ nm) for different temperatures, T, where we observe clear FP oscillations, allowing us to extract the FP cavity length in this device.

Figure 4.17(a) shows $G - V_G$ data for $T = 1$ up to 128 K. At 1 K we see

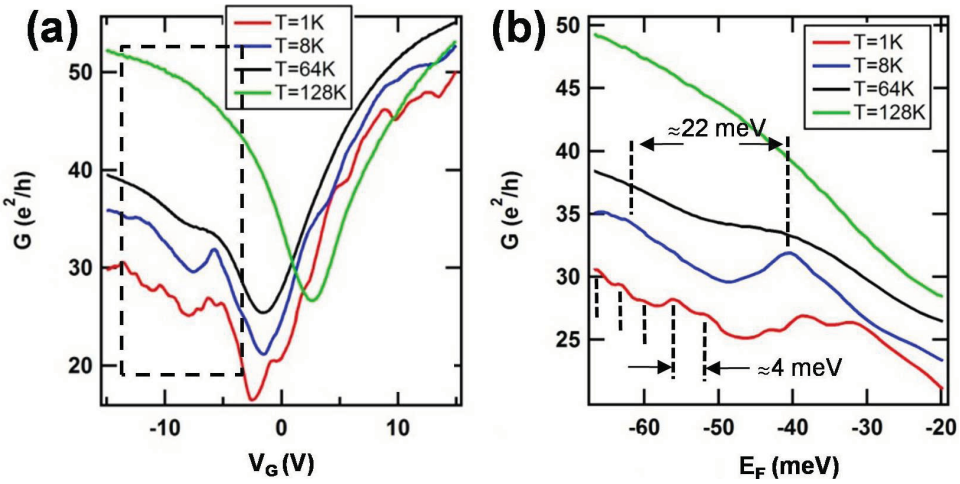

Figure 4.17: Temperature dependence of the conductance of Device F. (a) G vs V_G data for Device F at different temperatures, 1 K (red), 8 K (blue), 64 (black) and 128 K (green). (b) G vs E_F data for Device F for the section indicated in (a).

oscillations with two periods ($\Delta E_{small} \approx 4$ meV and slow oscillations $\Delta E_{big} \approx 22$ meV). As T increases these oscillations smear out. At 8 K, the small energy spacing oscillations (ΔE_{small}) which correspond to a long cavity according to the equation 4.10 are almost gone. By 64 K, these oscillations are gone, and the slow oscillations (ΔE_{big}) survive until $T = 128$ K. We use equation 4.4 to translate V_G into Fermi energy (E_F). Fig. 4.17 (b) shows G vs E_F for sample F at various T. The cavity length, L_{FP}, can be extracted from this plot using equation 4.10. We find $L_{FP} \approx 94 \pm 5$ nm and $\approx 700 \pm 50$ nm using $\Delta E_{big} \approx 22 \pm 1$ meV and $\Delta E_{small} \approx 4 \pm 1$ meV respectively. The $L_{FP} \approx 94 \pm 5$ nm cavity length is expected for the Device F, based on the length of the device from the SEM image $L_{SEM} \approx 98$ nm (see Fig. 4.15 (c)). However the second length scale, $L_{FP} \approx 700 \pm 50$ nm is much longer than the length of the channel seen.

The visibility (amplitude) of the oscillations changes as a function of the temperature

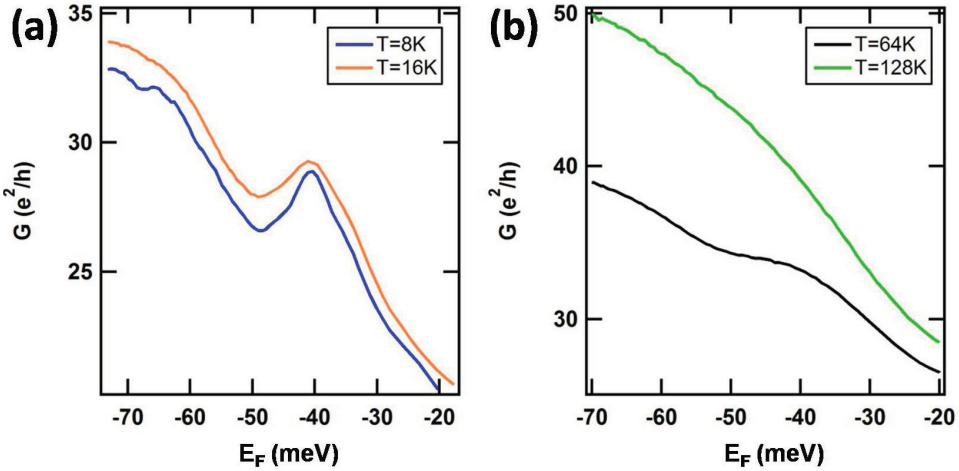

Figure 4.18: FP oscillations at different temperatures for device F. (a) G vs E_F for Device F at $T = 8$ K and $T = 16$ K. (b) G vs E_F for Device F at $T = 64$ K and $T = 128$ K.

[11]. The FP interference should be visible when the energy spacing between the oscillations, ΔE, is larger than the thermal fluctuation $k_B T$. Thus, we expect to lose visibility when the energy spacing, ΔE_{FP}, is comparable with $k_B T$. Thus,

$$\begin{aligned} if, \quad \Delta E_{FP} &\gg k_B T \\ then, \quad L_{FP} &\ll L_{Thermal} \end{aligned} \tag{4.11}$$

where $L_{FP} = \frac{\pi \hbar v_F}{\Delta E_{FP}}$ and $L_{Thermal} = \frac{\pi \hbar v_F}{k_B T}$.

Fig. 4.18 (a) shows the G vs E_F for Device F at $T = 8$ K and $T = 16$ K. We can still see the ΔE_{small} at $T = 8$ K ($k_B T \approx 0.7$ meV) but with low visibility. By $T = 16$ K ($k_B T \approx 1.38$ meV) these interferences are suppressed. Considering that at 16 K, $L_{Thermal}$ (equation 4.11) is about ≈ 1.5 μm, it puts the upper limits on the FP cavity length at <1.5 μm. This is consistent with the FP cavity length of $\approx 700 \pm 50$ nm extracted from ΔV_G for low energy oscillations of $\approx 3 - 4$ meV.

Fig. 4.18 (b) shows the G vs E_F for Device F at $T = 64$ K and $T = 128$ K. At 64 K, where $k_B T \approx 5.5$ meV, we still see some high energy $\Delta E_{big} \approx 22 \pm 1$ meV oscillations. However by 128 K, where $k_B T \approx 11$ meV, there are no visible oscillations. Considering that $L_{Thermal}$ is about ≈ 190 nm at $T = 128$ K, the FP cavity for these high energy

interferences should be < 190 nm. This is in agreement with the $L_{FP} = 94 \pm 5$ nm we extracted from ΔV_G. This confirms that we observe coherent interferences corresponding to the length of the suspended graphene channel visible in the SEM image ($L_{SEM} \approx 98$ nm) as well as coherence interference corresponding to a much longer cavity. In the next section we will explain the origin of this longer cavity. We observed similar FP interferences in four devices, and found a similar agreement between the temperature and V_G dependance of the interference pattern.

We continue our analysis by presenting a 2D map of FP oscillations as a function of both V_G and V_B for Device C. We show that the measured FP cavity length from V_B and V_G are also in agreement.

Fig. 4.19 (a) 2D map $dI/dV - V_B - V_G$ data for Device C at $T = 4.2$ K. The FP

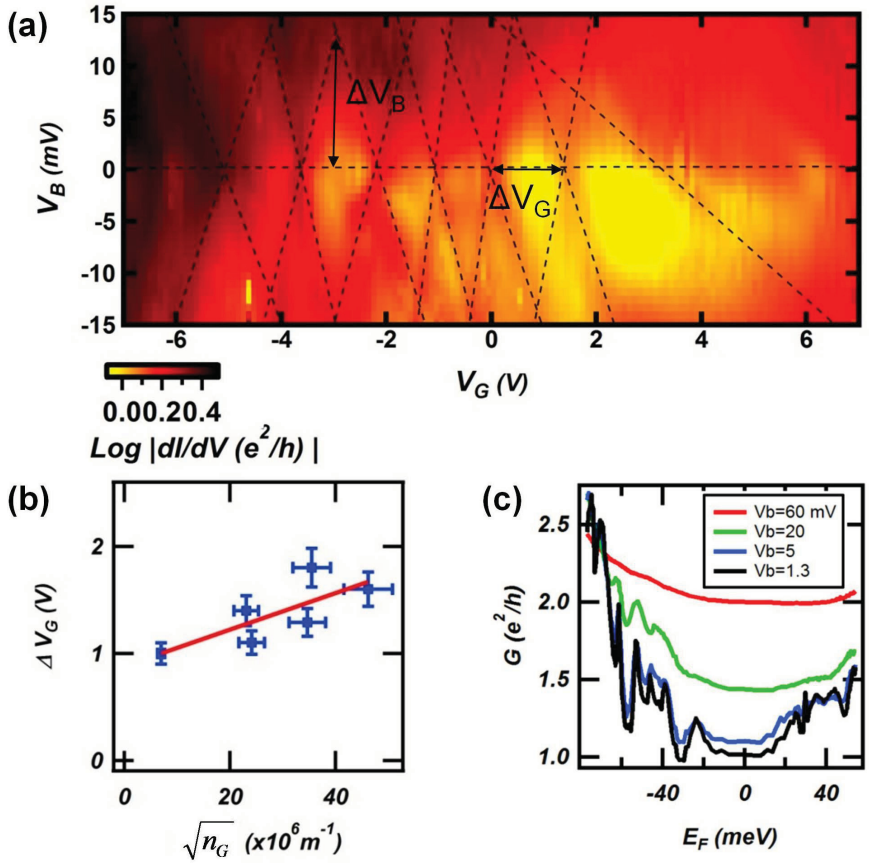

Figure 4.19: 2D map of FP interference for device C.(a) 2D map $dI/dV - V_B - V_G$ data for Device C at $T = 4.2$ K. (b)ΔV_G as a function of $\sqrt{n_G}$ (carrier density). The slope is $\approx 1.7 \times 10^{-8}$ V/m. (c) 1D cuts along V_G sweeps in (a) at different V_B.

interference pattern is visualized in this 2D map as straight intersecting lines. The cavity length can be extracted from the value of V_B at the intersection points of two lines. At these intersections, we have [73]:

$$\Delta V_B = \frac{\pi \hbar v_F}{e L_{FP}} \tag{4.12}$$

where ΔV_B is the height of the V_B crossing points, and $e\Delta V_B$ is the energy spacing between fringes. We extract $L_{FP} \approx 170 \pm 20$ nm in Device C from the average ΔV_B of $\approx 12 \pm 2$ mV.

The value of L_{FP} can also be extracted from the horizontal ΔV_G spacing of the fringes. The energy spacing between two peaks can be extracted as follows:

$$\Delta E_{FP} = \frac{\pi \hbar v_F}{L_{FP}} = \hbar v_F (\sqrt{\pi n_2} - \sqrt{\pi n_1}) \tag{4.13}$$

and the following approximation can be used to express Eq. 4.13 in terms of ΔV_{gate}

$$(\sqrt{n_2} - \sqrt{n_1}) \approx \frac{n_2 - n_1}{2\sqrt{n_G}} = \frac{C_G \Delta V_G}{2e\sqrt{n_G}} \quad for \quad \Delta n_G \ll n_G \tag{4.14}$$

where n_G and C_G are the carrier density induced with the gate, and gate capacitance per unit of area respectively. Using equations 4.13 and 4.14 one finds:

$$\Delta V_G = \frac{2e\sqrt{\pi n_G}}{C_G L_{FP}} \tag{4.15}$$

Equation 4.15 shows that ΔV_G should increase as n_G (or V_G). Fig. 4.19 (a) clearly shows that ΔV_G is increasing as V_G increases to positive or negative voltages. In Fig. 4.19 (b) we plot the ΔV_G as a function of $\sqrt{n_G}$. The slope of this plot gives the FP cavity length as slope$= \frac{2e\sqrt{\pi}}{C_G L_{FP}}$. We extracted $L_{FP} \approx 140 \pm 20$ nm from the slope $\approx 1.7 \times 10^{-8}$ V/m).

Finally, we also extracted the L_{FB} from 1D cuts along V_G, as we did previously for Device F. Fig. 4.19 (c) shows $G - E_F$ data extracted from Fig. 4.19 (a) for Device C (using equation 4.4). We find that $L_{FP} \approx 200 \pm 20$ nm. Fig. 4.19 (c) shows that as V_B increases to higher values, the oscillations disappear, which is likely due to inelastic electron-electron scattering [74].

In summary we extracted the $L_{FP} \approx 140 - 200$ nm long from 2D data. This

$L_FP \approx 140 - 200$ is much longer than $L_{SEM} \approx 23$ nm for Device C, similarly to Device F (L_{SEM}=95 nm, and $L_{FPlong} \approx 700$ nm), under the gold and from an extended FP cavity. This suggests that some conduction modes can "leak" (due to Klein tunneling) into the graphene under the gold contacts. This is possible, because long sections of the gold contacts are suspended and annealed, which could mean that graphene under these contacts is also ballistic.

4.5 Ballistic graphene contacts for graphene transistors

In the previous section we extracted the FP cavity length for different devices. The maximum extracted cavity length was much longer than the channel of the device measured by SEM. This suggests that some of the conduction modes coherently leak into the graphene under the gold. In this section we will discuss the implication of this observation for our devices, and the origin of this long FP cavity.

Fig. 4.20 (b) shows a tilted SEM image ($\approx 85°$ tilt) of one of our samples. We see that the horizontal distance etched under the gold bridge is much longer than the depth (vertical distance) of the etch. According to this SEM image, the contacts are suspended over a horizontal length of ≈ 800, nm although the sample was vertically etched at ≈ 100 nm. We measured the suspended length, L_{sus} of several samples from tilted SEM images and plot L_{sus} etched depth (see Fig. 4.20 (c)). The geometry of the entire device is shown in detail in Fig. 4.20. One notices three distinct sections. Section 1: the ballistic transistor channel which corresponds to the observed high energy FP interferences. This section is surrounded by vacuum (vacuum/graphene/vacuum). Section 2: suspended graphene covered by gold (gold/graphene/vacuum); we name this section "suspended contact". Section 3: graphene sandwiched between gold and SiO_2 (gold/graphene/SiO_2). These three sections have different carrier densities, gate electric fields, disorder and phase coherence lengths.

During the electromigration and annealing processes, sections 1 and 2 become very hot. It is reported that the temperature of graphene during annealing can reach ≥ 1000 K [3] [24]. This temperature is high enough to remove H_2O and EBL resist,

[3] Graphene breakdown temperature in vacuum is around 2230 K [24].

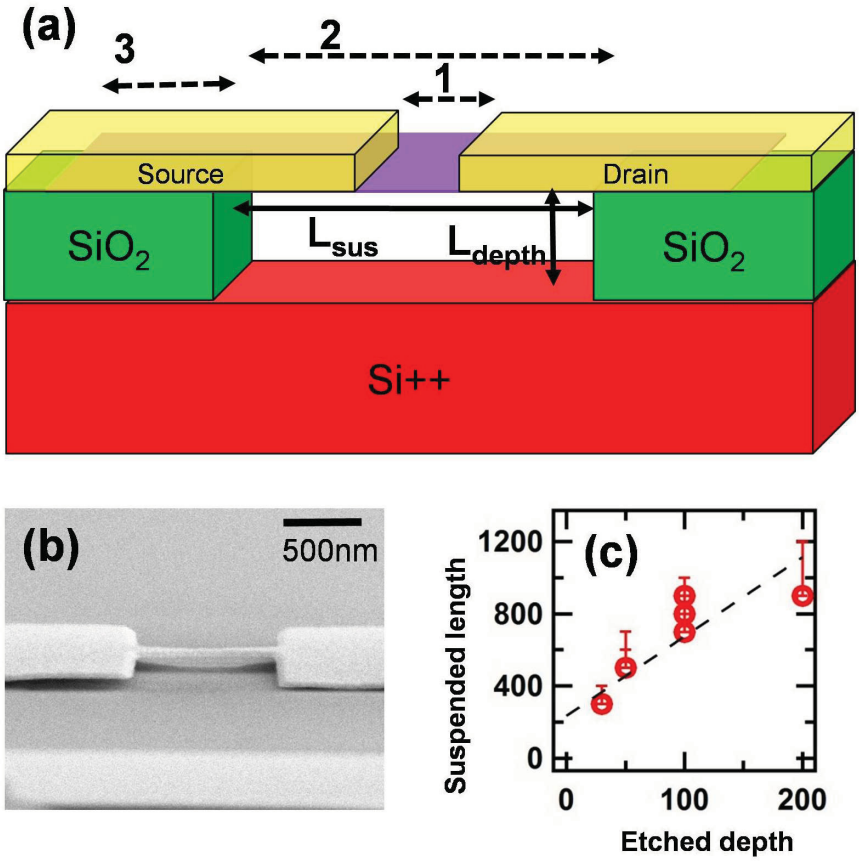

Figure 4.20: Suspended length of electromigrated graphene devices.(a) Cartoon of a suspended graphene transistor showing the three sections: graphene/vacuum, gold/graphene/vacuum and gold/graphene/SiO2. (b) Tilted SEM image ($\approx$ 85 degree) of a suspended break-junction. (c) Calibration curve showing the suspended length vs the etched depth, which indicates how much sample is suspended horizontally vs the etching depth. gold/graphene/SiO2.

such that the graphene in sections 1 and 2 is very clean. Fig. 4.21 shows SEM images of Devices A and C after electromigration and annealing. A close inspection reveals that the texture of the gold film is very different between sections 3, 1 and 2. The non-suspended section 3 did not heat up enough during annealing to ashen impurities since it is thermally anchored to the substrate. Indeed Fig. 4.21 shows that the gold film remains rough in section 3. Thus, it remains contaminated (H_2O and EBL resist) and disordered (SiO_2 charge traps and phonons). Moreover, the gate electric field is different in section 3 since the dielectric constant of SiO_2 is almost four times larger than that of vacuum. Looking at these three sections from the charge carrier's electronic point of view, one notices the formation of two cavities. Cavity 1: suspended graphene section 1 limited by the gold contacts, and Cavity 2: suspended graphene limited by the SiO_2 substrate.

The long FP cavity length extracted in section 4.4 and the suspended length

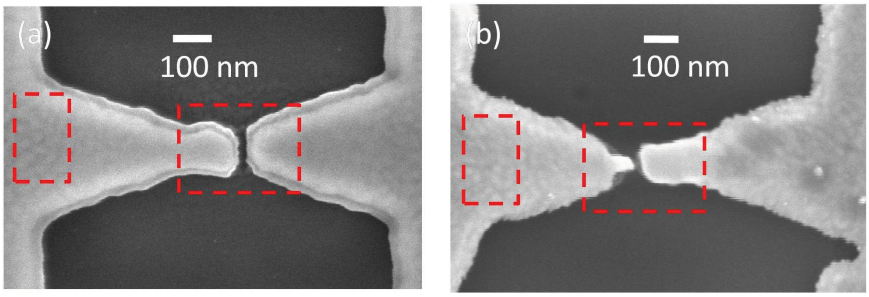

Figure 4.21: SEM images of devices A and C after electromigration and annealing. (a) SEM images of Device C after electromigration and annealing processes. (b) SEM images of Device A after electromigration and annealing processes.

(Fig. 4.20 (c)) are consistent. While section 1 is the transistor channel, since the transport data agree with the ballistic model using L and W of section 1, there are a few modes which coherently leak into section 2 (gold/graphene/vacuum), but are reflected at the edge of the disordered section 3. These "leaking" modes are the ones with $\theta \approx 0$ and, as expected for Klein tunneling (see sections 1.2.1 and 4.1.2), they cannot be stopped by *n-p-n* junctions. In order to observe FP interferences in section 2 we must have ballistic transport in both sections 1 and 2. But section 3, (gold/graphene/SiO_2), is a diffusive section where carriers quickly lose their coherence. Thus, we demonstrated that we have ballistic transistor channels (section 1)

connected by ballistic graphene contacts (section 2). These ballistic wires could be used to transport the coherent (quantum) information in graphene circuits [72, 75, 76].

4.6 Conclusion

In this chapter we reported electron transport in $23-105$ nm long suspended graphene ballistic n-p-n junctions. The shortest high-quality ballistic transistor we made was 23 nm long ($\approx$ 10 nm p-n junction). We make use of gold-gated graphene/bare graphene interference to create charge density gradients (p-n junctions) in graphene. Since the spacing between gold and graphene is $\leq$ 1 nm [57], we could reduce the size of the p-n junction down to the 10 nm scale. We observed ballistic transport in agreement with the theory of Dirac fermions in ultra-short graphene devices [56]. We observed FP interferences as evidence of coherent ballistic transport. We observed coherent transport up to a length scale of $\approx$ 700 nm in suspended Devices F and M. This suggests the formation of ballistic transport in graphene under the gold film. Thus, graphene under the gold acts as ballistic electron contacts for the graphene transistor channel. The combination of ballistic transistors (computing) and ballistic wires (communication) form the building blocks for future graphene nanoelectronic devices.

The devices we fabricated also provide a platform for future studies of the effects of mechanical strain (gauge field) on the quantum phase of the carriers in 10 nm scale p-n junctions.(*i.e.* strain-engineering of graphene electronics) [77].

Chapter 5

Conclusion, and other contributions

We have developed a feedback controlled electromigration technique capable of fabricating ≈ 10 nm scale clean suspended graphene quantum dots and ballistic transistors. Our devices are, to our knowledge, the smallest suspended graphene devices made to date. In such short devices, the quantum properties of the relativistic-like charge carriers (Dirac fermions) in graphene offer a platform for fundamental studies and the creation of nanoelectronic devices. We studied the effects of quantum lateral confinement on electron transport, for widths ranging from 30 to 1500 nm. The 30 nm wide devices show QD behaviour at $T = 4.2$ K. Measuring electron transport across these devices, we observed a variable charging energy as a function of the charge occupation of the dot, as expected for the chaotic billiard transport of Dirac fermions. We observed electron-vibron coupling and NEMS frequencies of ≈ 100 GHz. We demonstrated ≈ 10 nm graphene p-n junctions and ballistic transistors which could be used as the building blocks for graphene-based nanoelectronic circuits [78, 79]. Finally, we showed coherent ballistic transport over distances of up to ≈ 700 nm in graphene wires doped by a gold film, which could be used as buses for quantum information [72, 75, 76]. A brief summary of data showing these effects is presented in Fig. 5.1.

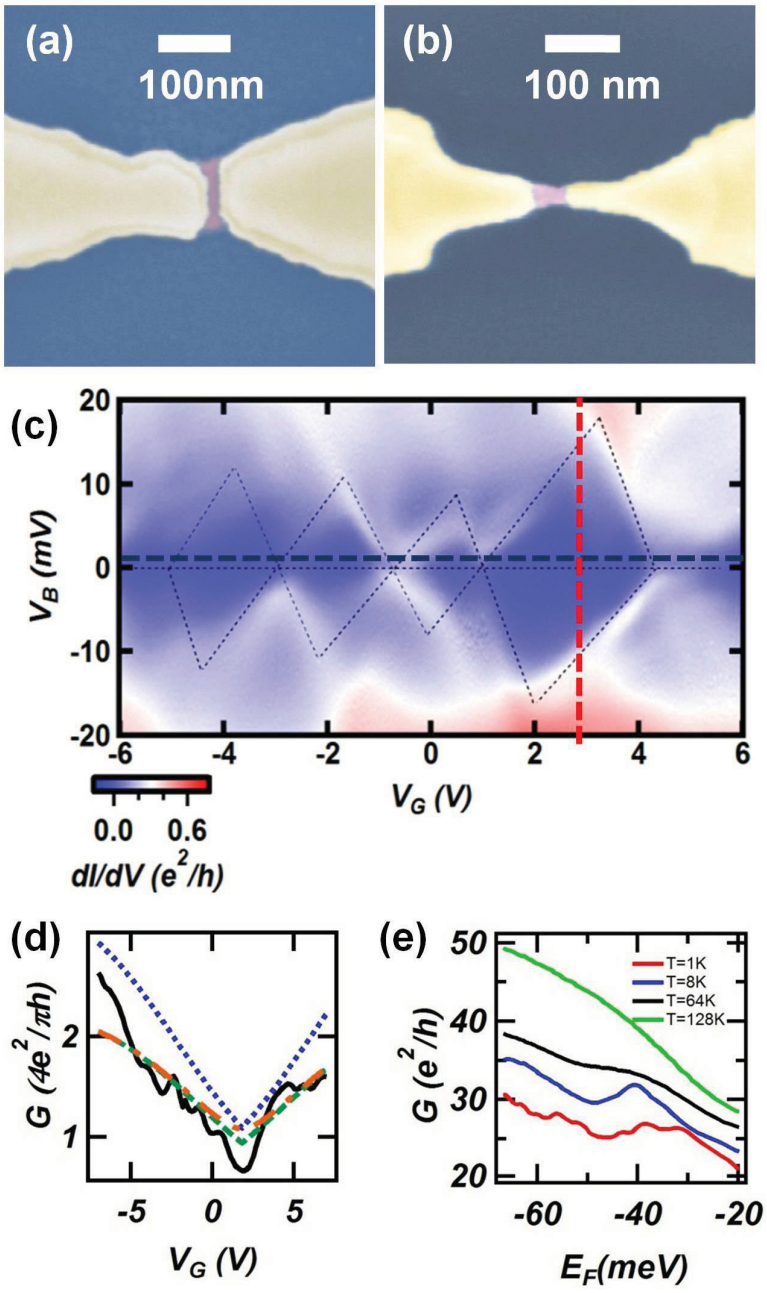

Figure 5.1: Summary of main results from suspended graphene QD and ballistic devices. (a) and (b) are SEM images of a $\approx$ 26 nm long ballistic transistor and a $\approx$ 32 nm suspended graphene quantum dot respectively. (c) Contour plot dI/dV as a function of V_B and V_G for the graphene quantum dot shown in (b). (d) G as a function of V_G for a ballistic transistor in agreement with the theory of Dirac fermions [56]. (d) G as a function of Fermi energy, E_F, at different temperatures for a 100 nm long ballistic transistor showing FP oscillations phase coherent interference.

5.1 Main results

In chapter 2 we explained the sample fabrication and experimental setup to create and measure suspended nanometer-size gold on graphene break-junctions. We described the wiring up of these nanometer scale devices to macroscopic electronics, and how we cool them down to low temperatures.

In Chapter 3, we presented an electromigration method to etch nanogaps in these suspended gold bridges, and expose an $\approx 10-100$ nm long graphene channels in the center of the gold bridges [28, 2]. Such ≈ 10 nm scale transistors cannot be fabricated using standard nanofabrication techniques. Using our electromigration technique we can tailor the shape and size of the graphene channel to fabricate devices with different channel length and widths. The narrower channels (≈ 30 nm) formed graphene quantum dots while the wider ones (≈ 100 nm) acted as ballistic transistors (described in chapter 4). Fig. 5.1(a)-(b) show examples of such devices. Fig. 5.1(b) is a $\approx 24 \times 44$ nm suspended graphene QD which is, to our knowledge, the smallest graphene QD made to date.

The electromigration tailored QDs that we fabricate, offer the prospect of distinguishing and isolating different sources of disorder in QDs: we can control substrate disorder by suspension, edge disorder by making the devices wider, and bulk disorder by intentionally introducing defects by electromigrating the graphene. This disorder control should lead to the ability to make higher quality QD devices, by minimising sources of disorder, and allow the study of effects of the different types of disorder on charge transport in graphene [80, 81, 82].

We studied the charge transport across ≈ 30 nm graphene QDs as a function of bias voltage (V_B) and the charge occupation number (V_G) [10]. As previously observed for graphene QDs ≤ 100 nm, the charging energy, E_C, of the QDs is variable as a function of the charge occupation due to the chaotic billiard transport of Dirac fermions bouncing off disordered graphene edges [35]. Fig. 5.1(c) is a contour plot $dI/dV - V_B - V_G$ for the 24×44 nm suspended graphene QD shown in Fig. 5.1(b) and non-periodic Coulomb diamonds. Graphene QDs have applications in nanoelectronics [76, 83, 84], spintronics [41, 85] and charge sensing [36].

We observed signatures of electron-vibron coupling in $dI/dV - V_B - V_G$ data in our suspended QDs. Due to a high Q-factor (after annealing/electromigration), coupling between electrons and out-of-plane vibrons (bending mode) can gives rise

to self-actuated vibrations [3]. We extracted vibrational frequencies of up to ≈ 100 GHz, in agreement with the frequencies expected from the geometry of the devices. These frequencies largely exceed any reported frequencies for graphene NEMS [7, 4]. Suspended graphene NEMS offer a platform for studying the effects of strain on Dirac electron transport and electron-vibron coupling. High-frequency suspended graphene resonators are useful for ultra sensitive force/mass sensors and NEMS [4, 5, 7].

In Chapter 2 we fabricated $23 - 100$ nm long suspended graphene ballistic n-p-n junctions ($\approx$10 nm p-n junctions), Fig. 5.1(d). We made use of an ultra-clean (annealed) gold film on top of graphene to n-doped the graphene. We build a p-n or n'-n junctions across the gold-on-graphene-/bare-graphene interfaces. Since the spacing between the gold film and graphene underneath it is ≤ 1 nm [57], we could reduce the size of the p-n junctions down to the ≈ 10 nm scale. Fig. 5.1(a) shows an example of such graphene n-p-n transistors. Graphene p-n junctions are the building blocks of graphene-based high speed transistors [79, 86].

We demonstrated coherent ballistic transport in agreement with the theory of Dirac fermions [56] in these $23 - 100$ nm long suspended graphene transistors, as shown in Fig. 5.1 (d). We see phase coherent interferences (Fabry-Pérot) in our devices as evidence of coherent ballistic transport [10]. Fig. 5.1(e) is an example of FP oscillations in a 100 nm long ballistic transistor. We measured phase coherent lengths of up to 700 nm in our graphene devices. These phase coherent lengths are much longer than the lengths extracted from SEM images of our devices (channel of the transistor) which shows that some of the conductance modes are coherently transmitted across the p-n junction and "leak" into the contacts. This supports the idea that we can achieve scattering-free (ballistic) transport in graphene buried under a gold film, thus creating ballistic contacts for our ballistic transistors [10]. The devices that we fabricate may provide a platform for future studies of the effects of strain (gauge field) on the phase of the carriers in 10 nm scale transistors, which offers the prospect of strain-engineering graphene electronics [77, 87]. Ballistic graphene transistors and ballistic leads can be used as quantum bits and quantum wires [60, 76, 88].

5.2 Contributions to other research projects

I have made substantial contributions to other research projects which led to three publications in peer-reviewed journals [2, 3, 23]. My contributions were focused on developing the sample fabrication procedures and measurement methods, as well as training fellow labmates. I also contributed to the construction of the instrumentation necessary for these experiments and assisted with the data analysis.

5.2.1 Few-hundred GHz carbon nanotube nanoelectromechanical systems (NEMS)

In addition to graphene, we used our feedback controlled electromigration technique to make clean suspended single-wall carbon nanotube (SWCNT) QDs ranging in length from ≈ 3 nm up to a few 10s of nm [2].

Fig. 5.2 (a) shows a ≈ 22 nm long section of a SWCNT suspended between gold

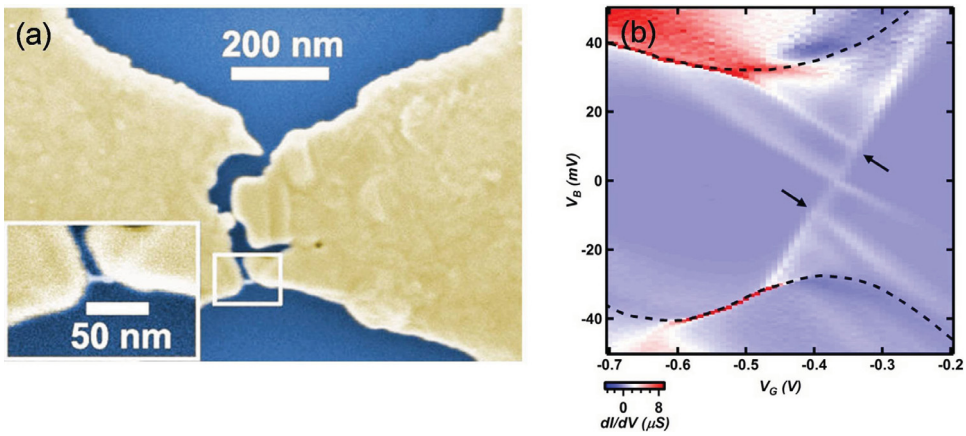

Figure 5.2: Few-hundred GHz carbon nanotube nanoelectromechanical systems (NEMS). (a) SEM image of ≈ 22 nm long SWCNT-QD. (b) Contour plot $dI/dV - V_B - V_G$ of a SWCNT-QD. The arrows point to the stretching vibron excitation modes and the dashed lines indicate bending mode resonances.

contacts. We find that this device forms a clean and tuneable QD, and observe signatures of both the stretching and bending vibrational modes. We used electron transport to measure the energy spectrum of these devices. The arrows in Fig. 5.2

(b) point to the stretching vibron exciations while the dashed lines indicate bending mode resonances. We were able to measure the self-actuated bending mode using DC transport, by making use of a positive feedback mechanism between tunneling electrons and bending oscillations. In these NEMS, we measured fundamental bending frequencies $f_{bend} \approx 75 - 280$ GHz and extract quality factors $Q \sim 10^6$. We find that our NEMS' bending frequencies can be tuned by a factor of two, with tension induced by the electrostatic force from the gate electrodes [3].

5.2.2 Electronic thermal conductivity measurements in intrinsic graphene

We fabricated few hundreds of nm up to micron-scale clean suspended graphene transistors. Fig. 5.3 (a) shows an SEM image of such a device. We extracted the electronic thermal conductivity in these devices using two-point DC electron transport measurements in the nearly intrinsic regime, over a temperature range of $20 - 300$ K. We used a Joule self-heating technique, in which the resistance of the samples is used as both a heater and thermometer. Since our devices are suspended, we could prevent heat leak to the substrate and achieve current annealing. We performed our experiments at low bias voltages, where the electron and lattice temperatures are decoupled. This allows us to detect the average temperature of electrons in graphene and to extract the electronic thermal conductivity independently from the phononic contribution, using the heat equation. We found K_e ranging from 0.5 to 11 W/m K over the studied temperature range. Fig. 5.3 (b) shows K_e as a function of average electron temperature for three different devices. The data (symbols) are consistent with a model (solid lines) in which heat is carried by quasiparticles with the same mean free path and velocity as graphene's charge carriers [23]. The electronic thermal conductivity of graphene and two-dimensional Dirac materials is of fundamental interest and can play an important role in the performance of nanoscale devices.

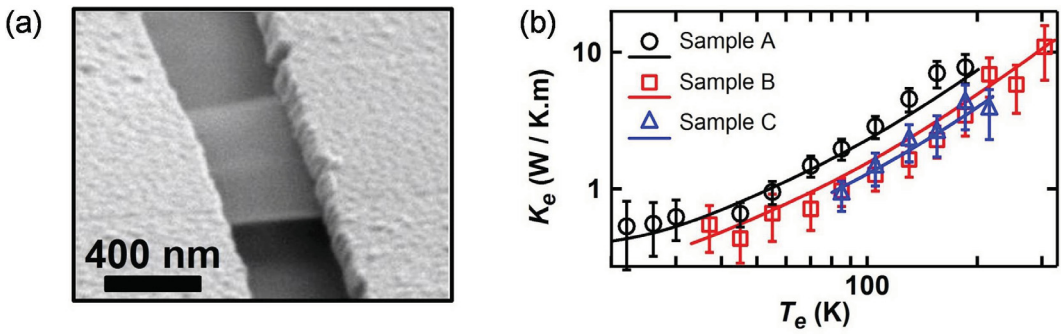

Figure 5.3: Electronic thermal conductivity measurements in intrinsic graphene. (a) A tilted SEM image of a 400 nm long suspended graphene transistor. (b) Electronic thermal conductivity K_e in the quasi-intrinsic regime. The solid lines are a theoretical calculation and the symbols are the experimental data.

Bibliography

[1] V. Tayari et al., *Tailoring of 10-nm-scale suspended graphene quantum dots by electromigration*, In preparation for Applied Physics Letters (2014).

[2] J. O. Island, V. Tayari, S. Yigen, A. C. McRae, and A. R. Champagne, *Ultra-short suspended single-wall carbon nanotube transistors*, Applied Physics Letters **99**, 243106 (2011).

[3] J. O. Island, V. Tayari, A. C. McRae, and A. R. Champagne, *Few-Hundred GHz Carbon Nanotube Nanoelectromechanical Systems (NEMS)*, Nano Letters **12**, 4564 (2012).

[4] J. S. Bunch et al., *Electromechanical Resonators from Graphene Sheets*, Science **315**, 490 (2007).

[5] C. Changyao and J. Hone, *Graphene nanoelectromechanical systems*, Proceedings of the IEEE **101**, 1766 (2013).

[6] D. Garcia-Sanchez et al., *Imaging Mechanical Vibrations in Suspended Graphene Sheets*, Nano Letters **8**, 1399 (2008).

[7] C. Chen et al., *Performance of monolayer graphene nanomechanical resonators with electrical readout*, Nature nanotech (2009).

[8] X. Song et al., *Stamp Transferred Suspended Graphene Mechanical Resonators for Radio Frequency Electrical Readout*, Nano Letters **12**, 198 (2011).

[9] S. Shivaraman et al., *Free-Standing Epitaxial Graphene*, Nano Letters **9**, 3100 (2009).

[10] V. Tayari, A. C. McRae, and A. R. Champagne, *Ballistic transport in nanometer-scale suspended graphene transistor*, In preparation for Nano Letters (2014).

[11] A. F. Young and P. Kim, *Quantum interference and Klein tunnelling in graphene heterojunctions*, Nat Phys **5**, 222 (2009).

[12] X. Du, I. Skachko, A. Barker, and E. Y. Andrei, *Approaching ballistic transport in suspended graphene*, Nat Nano **3**, 491 (2008).

[13] Y. Wu et al., *Quantum Behavior of Graphene Transistors near the Scaling Limit*, Nano Letters **12**, 1417 (2012).

[14] A. H. Castro Neto, F. Guinea, N. M. R. Peres, K. S. Novoselov, and A. K. Geim, *The electronic properties of graphene*, Reviews of Modern Physics **81**, 109 (2009).

[15] A. K. Geim and K. S. Novoselov, *The rise of graphene*, Nat Mater **6**, 183 (2007).

[16] J. Gttinger et al., *Transport through graphene quantum dots*, Reports on Progress in Physics **75**, 126502 (2012).

[17] M. I. Katsnelson, K. S. Novoselov, and A. K. Geim, *Chiral tunnelling and the Klein paradox in graphene*, Nature Physics **2**, 620 (2006).

[18] K. I. Bolotin et al., *Ultrahigh electron mobility in suspended graphene*, Solid State Communications **146**, 351 (2008).

[19] P. Rickhaus et al., *Ballistic interferences in suspended graphene*, Nat Commun **4** (2013).

[20] C. Lee, X. Wei, J. W. Kysar, and J. Hone, *Measurement of the Elastic Properties and Intrinsic Strength of Monolayer Graphene*, Science **321**, 385 (2008).

[21] H. J. Mamin and D. Rugar, *Sub-attonewton force detection at millikelvin temperatures*, Applied Physics Letters **79**, 3358 (2001).

[22] M. D. LaHaye, O. Buu, B. Camarota, and K. C. Schwab, *Approaching the Quantum Limit of a Nanomechanical Resonator*, Science **304**, 74 (2004).

[23] S. Yien, V. Tayari, J. O. Island, J. M. Porter, and A. R. Champagne, *Electronic thermal conductivity measurements in intrinsic graphene*, Physical Review B **87**, 241411 (2013).

[24] V. E. Dorgan, A. Behnam, H. J. Conley, K. I. Bolotin, and E. Pop, *High-Field Electrical and Thermal Transport in Suspended Graphene*, Nano Letters **13**, 4581 (2013).

[25] K. S. Novoselov et al., *Electric Field Effect in Atomically Thin Carbon Films*, Science **306**, 666 (2004).

[26] A. A. Balandin, *Thermal properties of graphene and nanostructured carbon materials*, Nat Mater **10**, 569 (2011).

[27] M. I. Katsnelson, K. S. Novoselov, and A. K. Geim, *Chiral tunnelling and the Klein paradox in graphene*, Nat Phys **2**, 620 (2006).

[28] H. Park, A. K. L. Lim, A. P. Alivisatos, J. Park, and P. L. McEuen, *Fabrication of metallic electrodes with nanometer separation by electromigration*, Applied Physics Letters **75**, 301 (1999).

[29] S. F. Shi, X. D. Xu, D. C. Ralph, and P. L. McEuen, *Plasmon Resonance in Individual Nanogap Electrodes Studied Using Graphene Nanoconstrictions as Photodetectors*, Nano Letters **11**, 1814 (2011).

[30] P. Geim, Andre. K. Kim, *Carbon wonderland*, Scientific American **298** (2008).

[31] A. C. Ferrari et al., *Raman Spectrum of Graphene and Graphene Layers*, Physical Review Letters **97**, 187401 (2006).

[32] P. E. Gaskell, H. S. Skulason, C. Rodenchuk, and T. Szkopek, *Counting graphene layers on glass via optical reflection microscopy*, Applied Physics Letters **94**, 143101 (2009).

[33] D. Graf et al., *Spatially Resolved Raman Spectroscopy of Single- and Few-Layer Graphene*, Nano Letters **7**, 238 (2007).

[34] A. Gupta, G. Chen, P. Joshi, S. Tadigadapa, and Eklund, *Raman Scattering from High-Frequency Phonons in Supported n-Graphene Layer Films*, Nano Letters **6**, 2667 (2006).

[35] L. A. Ponomarenko et al., *Chaotic Dirac Billiard in Graphene Quantum Dots*, Science **320**, 356 (2008).

[36] J. Guttinger et al., *Charge detection in graphene quantum dots*, Applied Physics Letters **93**, 212102 (2008).

[37] C. Stampfer et al., *Tunable Graphene Single Electron Transistor*, Nano Letters **8**, 2378 (2008).

[38] K. Todd, H.-T. Chou, S. Amasha, and D. Goldhaber-Gordon, *Quantum Dot Behavior in Graphene Nanoconstrictions*, Nano Letters **9**, 416 (2008).

[39] S. Schnez et al., *Observation of excited states in a graphene quantum dot*, Applied Physics Letters **94**, 012107 (2009).

[40] J. Gttinger et al., *Electron-Hole Crossover in Graphene Quantum Dots*, Physical Review Letters **103**, 046810 (2009).

[41] J. Gttinger, T. Frey, C. Stampfer, T. Ihn, and K. Ensslin, *Spin States in Graphene Quantum Dots*, Physical Review Letters **105**, 116801 (2010).

[42] J. Park, *Electron Transport in Single Molecule Transistors*, PhD thesis, 2003,.

[43] T. Ohta, A. Bostwick, T. Seyller, K. Horn, and E. Rotenberg, *Controlling the Electronic Structure of Bilayer Graphene*, Science **313**, 951 (2006).

[44] R. Balog et al., *Bandgap opening in graphene induced by patterned hydrogen adsorption*, Nat Mater **9**, 315 (2010).

[45] G. Giovannetti, P. A. Khomyakov, G. Brocks, P. J. Kelly, and J. van den Brink, *Substrate-induced band gap in graphene on hexagonal boron nitride: Ab initio density functional calculations*, Physical Review B **76**, 073103 (2007).

[46] H. Park et al., *Nanomechanical oscillations in a single-C-60 transistor*, Nature **407**, 57 (2000).

[47] J. W. Park et al., *Wiring up single molecules*, Thin Solid Films **438**, 457 (2003).

[48] K. I. Bolotin, F. Kuemmeth, A. N. Pasupathy, and D. C. Ralph, *Metal-nanoparticle single-electron transistors fabricated using electromigration*, Applied Physics Letters **84**, 3154 (2004).

[49] D. R. Strachan et al., *Controlled fabrication of nanogaps in ambient environment for molecular electronics*, Applied Physics Letters **86** (2005).

[50] G. Esen and M. S. Fuhrer, *Temperature control of electromigration to form gold nanogap junctions*, Applied Physics Letters **87** (2005).

[51] D. R. Strachan et al., *Clean electromigrated nanogaps imaged by transmission electron microscopy*, Nano Letters **6**, 441 (2006).

[52] M. L. Trouwborst, S. J. van der Molen, and B. J. van Wees, *The role of Joule heating in the formation of nanogaps by electromigration*, Journal of Applied Physics **99** (2006).

[53] M. J. B. Moura and M. Marder, *Tearing of Free-Standing Graphene*, Physical Review E **88**, 032405 (2013).

[54] K. Kim et al., *Atomically perfect torn graphene edges and their reversible reconstruction*, Nat Commun **4** (2013).

[55] G. A. Steele et al., *Strong Coupling Between Single-Electron Tunneling and Nanomechanical Motion*, Science **325**, 1103 (2009).

[56] J. Tworzydo, B. Trauzettel, M. Titov, A. Rycerz, and C. W. J. Beenakker, *Sub-Poissonian Shot Noise in Graphene*, Physical Review Letters **96**, 246802 (2006).

[57] G. Giovannetti et al., *Doping Graphene with Metal Contacts*, Physical Review Letters **101**, 026803 (2008).

[58] P. A. Khomyakov et al., *First-principles study of the interaction and charge transfer between graphene and metals*, Physical Review B **79**, 195425 (2009).

[59] L. Liao et al., *High-speed graphene transistors with a self-aligned nanowire gate*, Nature **467**, 305 (2010).

[60] J. Zheng et al., *Sub-10 nm Gate Length Graphene Transistors: Operating at Terahertz Frequencies with Current Saturation*, Sci. Rep. **3** (2013).

[61] J. Thomas, *Quantum computing: Graphene qubits*, Nat Nano (2006).

[62] S. Barraza-Lopez, M. Vanevi, M. Kindermann, and M. Y. Chou, *Effects of Metallic Contacts on Electron Transport through Graphene*, Physical Review Letters **104**, 076807 (2010).

[63] W. R. Hannes, M. Jonson, and M. Titov, *Electron-hole asymmetry in two-terminal graphene devices*, Physical Review B **84**, 045414 (2011).

[64] F. Xia, V. Perebeinos, Y.-m. Lin, Y. Wu, and P. Avouris, *The origins and limits of metal-graphene junction resistance*, Nat Nano **6**, 179 (2011).

[65] M. Titov, *Impurity-assisted tunneling in graphene*, EPL (Europhysics Letters) **79**, 17004 (2007).

[66] R. V. Gorbachev, A. S. Mayorov, A. K. Savchenko, D. W. Horsell, and F. Guinea, *Conductance of p-n-p Graphene Structures with Air-Bridge Top Gates*, Nano Letters **8**, 1995 (2008).

[67] L. M. Zhang and M. M. Fogler, *Nonlinear Screening and Ballistic Transport in a Graphene p-n Junction*, Physical Review Letters **100**, 116804 (2008).

[68] P. A. Khomyakov, A. A. Starikov, G. Brocks, and P. J. Kelly, *Nonlinear screening of charges induced in graphene by metal contacts*, Physical Review B **82** (2010).

[69] V. V. Cheianov and V. I. Falko, *Selective transmission of Dirac electrons and ballistic magnetoresistance of n-p junctions in graphene*, Physical Review B **74**, 041403 (2006).

[70] D. McClain et al., *Impact of oxygen adsorption on a population of mass produced carbon nanotube field effect transistors*, Carbon **47**, 1493 (2009).

[71] N. Nemec, D. Tomanek, and G. Cuniberti, *Contact dependence of carrier injection in carbon nanotubes: An ab initio study*, Physical Review Letters **96** (2006).

[72] A. L. Grushina, D.-K. Ki, and A. F. Morpurgo, *A ballistic pn junction in suspended graphene with split bottom gates*, Applied Physics Letters **102**, (2013).

[73] W. Liang et al., *Fabry - Perot interference in a nanotube electron waveguide*, Nature **411**, 665 (2001).

[74] Q. Li and S. Das Sarma, *Finite temperature inelastic mean free path and quasiparticle lifetime in graphene*, Physical Review B **87**, 085406 (2013).

[75] ThomasJessica, *Quantum computing: Graphene qubits*, Nat Nano (2006).

[76] G. Guo-Ping et al., *Quantum computation with graphene nanoribbon*, New Journal of Physics **11**, 123005 (2009).

[77] V. M. Pereira and A. H. Castro Neto, *Strain Engineering of Graphenes Electronic Structure*, Physical Review Letters **103**, 046801 (2009).

[78] S. Chun-Yung, Graphene nanoelectronics, in *Semiconductor Device Research Symposium, 2009. ISDRS '09. International*, pages 1–2.

[79] G. Iannaccone et al., Perspectives of graphene nanoelectronics: probing technological options with modeling, in *Electron Devices Meeting (IEDM), 2009 IEEE International*, pages 1–4.

[80] J.-H. Chen, W. G. Cullen, C. Jang, M. S. Fuhrer, and E. D. Williams, *Defect Scattering in Graphene*, Physical Review Letters **102**, 236805 (2009).

[81] P. Gallagher, K. Todd, and D. Goldhaber-Gordon, *Disorder-induced gap behavior in graphene nanoribbons*, Physical Review B **81**, 115409 (2010).

[82] A. Lherbier et al., *Transport properties of graphene containing structural defects*, Physical Review B **86**, 075402 (2012).

[83] R. M. Westervelt, *Graphene Nanoelectronics*, Science **320**, 324 (2008).

[84] R. Patrik and T. Bjrn, *Quantum dots and spin qubits in graphene*, Nanotechnology **21**, 302001 (2010).

[85] D. Pesin and A. H. MacDonald, *Spintronics and pseudospintronics in graphene and topological insulators*, Nat Mater **11**, 409 (2012).

[86] F. Schwierz, *Graphene transistors*, Nat Nano **5**, 487 (2010).

[87] A. H. V. Mara, J. Fernando de, and C. Alberto, *Gauge fields and curvature in graphene*, Journal of Physics: Conference Series **129**, 012001 (2008).

[88] F. R. Braakman, C. W. W. Barthelemy, P. Reichl, and L. M. K. Vandersypen, *Long-distance coherent coupling in a quantum dot array*, Nat Nano **8**, 432 (2013).